Formation dry-out and injectivity impairment during CO_2 storage in saline aquifers

Proefschrift

ter verkrijging van de graad van doctor
aan de Technische Universiteit Delft,
op gezag van de Rector Magnificus *Prof. Ir. K.Ch.A.M. Luyben;*
voorzitter van het College voor Promoties,
in het openbaar te verdedigen op
2 september 2015 om 10.00 uur

Door

Saskia Maria ROELS
Master of Science in Hydrogeology geboren te *Rotterdam, Nederland*

This dissertation has been approved by the

promotor: *Prof. dr. P.L.J. Zitha*

Composition of the doctoral committee:

Rector Magnificus
Prof. dr. P.L.J. Zitha promotor

Independent members:
Prof. dr. ir. J. D. Jansen, CiTG, TU Delft
Prof. dr. W.R. Rossen, CiTG, TU Delft
Prof. dr. H. Geerlings, CiTG, TU Delft /Shell Global Solutions Intern. B.V.
Prof. dr. C. Spiers, Universiteit Utrecht
Dr. K.-H. Wolf, CiTG, TU Delft
Dr. H. Ott, Shell Global Solutions International B.V.

Substitute member:
Prof. dr. J. Bruining, CiTG, TU Delft

This research has been conducted as part of the Dutch National Program of CCS: CATO-2. The program consists of several sub-programs which focus on the different steps towards underground storage of CO_2: (1) Capture, (2) CO_2 transport and chain integration, (3) Underground storage, monitoring and verification, (4) Regulation and safety and (5) Public perception. This research was conducted as part of the Underground storage work package to develop this temporary solution as part of the transition to sustainable energy resources. It was carried out in the Laboratory of Geoscience and Engineering at Delft University of Technology.

Contents

List of Figures

List of Tables

Nomenclature

D	Diffusion	L^2T^{-1}
g	Gravity	$L^{-1}T^{-2}$
i	Component	-
k	Mass transfer coefficient	T^{-1}
K	Permeability	L^2
K_0	Initial permeability	L^2
k_r	Relative permeability	-
m	Van Genuchten parameter	-
n_g	Brooks and Corey parameter CO_2	-
n_w	Brooks and Corey parameter brine	-
P	Pressure	$ML^{-1}T^{-2}$
P_c	Capillary pressure	$ML^{-1}T^{-2}$
P_d	Entry pressure	$ML^{-1}T^{-2}$
Q	Evaporation rate	$ML^{-3}T^{-1}$
r	Precipitation coefficient	T^{-1}
R	Precipitation rate	$ML^{-3}T^{-1}$
s	Subscript for salt phase	-
S	Saturation	-
u	Velocity	LT^{-1}
v	Velocity	LT^{-1}
w	Subscript for water phase	-
X	Mass fraction	-
α	Phase	-
Γ	Verma and Pruess parameter	-
θ	Verma and Pruess parameter	-
μ	Viscosity	$ML^{-1}T^{-1}$
ρ	Density	ML^{-3}
φ	Porosity	-
φ_r	Porosity (K=0)	-
ω	Verma and Pruess parameter	-

1

Introduction

1.1. Geological CO2 storage

An energy mix corresponding to intermediate demand for hydrocarbons and increasing demand for alternative resources is considered to be the most likely energy scenario for the 21st century (Schollnberger, 1998). Although a notable increase in the usage of renewable energy forms is expected, the use of conventional fuels will still not be balanced and production of greenhouse gases is unavoidable (Fanchi, 2000). Accumulation of greenhouse gases in the atmosphere is an important factor in the contribution to global warming (Metz et al., 2007). Among these gases, CO_2 is of great importance due to its high radiative forcing and its long life (Solomon, 2007).

1.1.1. CO_2 emissions and CCS

The concentration of atmospheric CO_2 has increased by 35% over the last two centuries and is expected to double over the next 50 years (Metz et al., 2007), in case no mitigation measures are taken. As a great part of the atmospheric CO_2 increase is attributed to anthropogenic activities, society as a whole must act to mitigate this development.

Carbon dioxide capture and storage (CCS) is one of the most widely discussed options for reducing CO_2 emissions. This method concerns the techniques for capturing and purification of CO_2 from fossil-fuel power plants, subsequent compression and transport, and ultimately the storage of CO_2 in deep geological formations. An overview of recent injection pilots and commercial operations demonstrates that underground storage of CO_2 is a feasible technique (Michael et al., 2010). Three main types of sites for subsurface CO_2 storage have been discussed widely: saline aquifers, depleted oil and gas reservoirs, and coal beds (Metz et al., 2005). It has become the favoured option to store CO_2 in saline aquifers, due to their potential of high storage capacities (Fang et al., 2010; Hosa et al., 2011).

Suitable aquifers are high permeable sandstone formations, saturated with brackish water or brine, with sufficient capacity to store large amounts of CO_2. These storage sites are mainly located at depths between 1000-2000 m, where water contains too large salt concentration to function as a drinking water source. Under the pressures and temperatures present at such depths the injected CO_2 will have a lower density than the formation water and will flow upward due to buoyancy forces (Holloway, 2005). To prevent leakage towards shallower regions holding drinking water or the atmospheric surface, the aquifer should be confined by a layer of low-permeable material, usually referred to as *aquitard* (Bachu et al., 2007; Ebigbo et al., 2007).

1.1.2. Worldwide CO_2 storage projects

The four largest commercial CO_2 storage projects in saline aquifers, i.e. Sleipner, In Salah, Snøhvit and Gorgon are listed in Table 1.1 (Hosa et al., 2011; Michael et al., 2010). Sleipner and In Salah have been in operation for more than 10 years, Snøhvit for more than 6 years and Gorgon is due to start in 2015. Below follows a brief description of each project.

Sleipner is the first large scale CO_2 storage project and started in 1996. The Sleipner field produces 47,000 m^3 of oil per day, 36 million Sm^3 of gas per day and 14,000 Sm^3 condensate (light oil) per day. CO_2 is separated and then injected into an aquifer of the Utsira formation. The aquifer lies approximately 700 m beneath seabed and has a thickness of 250 m (Korbøl and Kaddour, 1995). Nearly 1 million metric tons of CO_2 per year have been successfully stored in the Sleipner project to this day (Arts et al., 2008).

The natural gas production field In Salah is located in Algeria at a depth of 1700 m below surface. The field is currently producing at plateau level of around 20,000 m^3 of oil per day and has an estimated storage capacity of 17 Mt. CO_2 injection started in 2004 and has reached an average injection rate of 1.2 million tons of CO_2 per year (Sengul, 2006).

The Snøhvit injection project was started in 2008 and is combined with the production of natural gas. Natural gas is first pumped to a carbon capture plant at Melkøya. Here, 5-8% of carbon dioxide is removed from the gas and piped back and injected into a 2400 m deep sandstone formation below seabed. By September 2010, 0.8 million tons of CO_2 had been injected (Eiken et al., 2011). The total storage capacity was estimated to be 23 Mt and the injection rate is 2000 tons/day (Hosa et al., 2011; Michael et al., 2010).

The Gorgon project includes the conversion of natural gas into liquefied natural gas (LNG) in combination with offshore CO_2 storage. With an estimated storage capacity of 129 Mt of CO_2, it is the largest storage site in the world (Hosa et al., 2011; Michael et al., 2010). The injection rate is estimated to be 12,300 tons/day.

Table 1.1. Worldwide largest CO_2 storage projects in saline aquifers (Hosa et al., 2011; Michael et al., 2010).

Project	*Location*	*Estimated storage capacity*	*(Expected) Start date*	*Injection rate (tons/day)*
Sleipner	North Sea, Norway	25 Mt	1996	2700
In Salah	In Salah, Algeria	17 Mt	2004	3500
Snøhvit	Barents Sea, Norway	23 Mt	2008	2000

Gorgon	Gorgon Area, Australia	129 Mt	2015	12,300

1.1.3. Challenges and gaps in knowledge

The existing CO_2 storage projects enabled the accumulation of site-specific knowledge and operational experience in the areas of static reservoir modeling and dynamic fluids behavior in the aquifer. However, up to now significant gaps exists in the understanding of phenomena inherent to the CO_2 storage process. A reason for this is that the design, planning and implementation of CO_2 storage projects often relied on the adaptation of methods used for oil and gas, without a detailed scrutiny of the effects arising from the interactions of CO_2 with fluids and the rock in the aquifer. For instance, the projects where dry CO_2 was injected, e.g. Snøhvit and In Salah, met with challenges due to severe injectivity decline (Eiken et al., 2011; Hansen et al., 2013). Experimental work on core plugs obtained from Snøhvit, indicated that CO_2 injection induces salt precipitation in the pores (Grude et al., 2013). The solid salt was mainly located at the pore throats which explains the significant impact on permeability and injectivity. Recent experimental and modeling studies have confirmed that salt precipitation induced by CO_2 injection leads to a reduction in formation permeability (Bacci et al., 2011; Pruess and Müller, 2009a). However, whether a reduction in formation permeability may lead to increased injection pressures still remains to be investigated. It was found by Muller et al. (2009) and Peysson et al. (2014) that capillary-driven backflow could lead to salt accumulation near the injection point, causing a dramatic decrease in injectivity. The exact conditions for capillary-driven backflow have not been understood and experimental proof is very limited. For example, the forces induced by different injection velocities that can suppress capillary-driven backflow should be examined. Therefore, current risk assessments on injectivity performance during underground CO_2 storage lack a solid knowledge basis.

1.1.4. Motivation for this research

This research concerns the geological storage of CO_2 and in particular injectivity impairment problems related to salt precipitation. Drying and salt precipitation in geological formations can have serious consequences for upstream operations in terms of injectivity and productivity. This can negatively affect the performance of injection and production wells and can even lead to well clogging, which is a serious risk for such operations. It is therefore of great importance to explore the effect of dry-out and salt precipitation on storage capacity and injectivity.

The understanding of dry-out and salt precipitation induced by CO_2 injection into aquifers is far from complete. There has been very limited dedicated experimental and modeling studies done to verify the potential of salt accumulation and its effect

on injectivity. The influence that factors such as injection velocity, capillary-driven flow and connecting brine-saturated layers have on injectivity remains largely unknown.
Recently, the use of X-ray computed tomography (CT) for observing saturation distributions inside porous media during experiments have led to an increase in understanding of single and multi-phase flow. In particular the usage of micro-computed tomography (μ-CT) can provide new insights into fluid and particle behavior inside a porous medium. When μ-CT X-ray transmission information is obtained from a multitude of radiographic images, scanned at different angles, a complete 3D image can be obtained, which can provide important information on solid salt distributions. The spatial and temporal resolutions of μ-CT allow us to study processes on a pore scale and, to the aim of this research provides us with 3D visualization of salt crystals inside the pore space. New experimental techniques such as (μ-)CT scanning and improved measurement devices on pressure drop in small cores can provide experimental results on salt precipitation during CO_2 injection, which are currently lacking in literature.

1.2. Research objectives and methodology

This research aims at gaining a better understanding of the conditions that lead to impairment in injectivity due to salt precipitation. To meet this objective, controlled experiments consisting of CO_2 injection into brine-saturated natural sandstone cores were performed. Salt precipitation and dry-out were investigated with the aid of CT and μ-CT scanning. Numerical modeling was used to give insight into the factors that influence solid salt distribution. We have tried to contribute to a better knowledge by answering the following research questions:

- Is it possible to visualize and quantify solid salt crystals inside a porous medium with the aid of μ-CT scanning? (Chapter 3)
- Does precipitation of salt affect injectivity? (Chapter 3)
- Can we simulate the dry-out process and salt precipitation pattern? (Chapter 3)
- What is the role of injection velocity on salt accumulation? (Chapter 4)
- What are the length scales that contribute to accumulation of salt near the inlet? (Chapter 4)
- How does the velocity field inside a radial injection domain influences salt precipitation patterns compared to a one-dimensional domain? (Chapter 5)
- Can we capture and quantify the dry-out process inside a radial injection domain with a medical CT scanner? (Chapter 5)

- Does a brine source that is connected to the CO_2 injection layer contribute to salt precipitation by capillary-driven flow of brine toward the dry zone? (Chapter 6)
- Does capillary-driven flow occur from a fine textured layer to a coarse textured layer when the latter is sufficiently dry? (Chapter 6)

1.3. Outline of the thesis

The chapters of this thesis are based on articles which are either published or currently under review. The text is partly identical to the published work and partly improved with increased understanding along the way. Consequently, the reader may find to some degree repetition in part of the chapters. The chapters in this thesis are structured as follows:

Chapter 2 provides the mathematical frame used in this study for describing CO_2-brine flows, taking into account the key processes involved with CO_2 injection into a brine-saturated porous medium: displacement of brine by CO_2, capillary forces, evaporation of water into CO_2 and salt precipitation.

Chapter 3 presents the results from the experimental and numerical work done on CO_2 injection into a one-dimensional domain. It describes core flooding experiments and shows visualization of solid salt inside a porous medium by µ-CT scanning. Numerical modeling of the process includes a kinetic versus a local equilibrium approach on evaporation.

Chapter 4 shows experimental and numerical work on the effect of injection velocity on salt accumulation. Visualization and quantification of solid salt inside a porous medium by µ-CT scanning was used to understand the effect of flow rate. An estimate of length scales over which capillary-driven flow can contribute to salt accumulation was done by numerical analysis.

Chapter 5 is devoted to the work of CO_2 injection into a radial domain. Experimental work shows the risk of formation clogging during radial injection of CO_2 into a brine-saturated porous medium. Numerical work shows the potential of formation clogging for two different injection velocities and compares the results with a one-dimensional flow domain.

Chapter 6 describes the effect of capillary-driven flow from a brine source on salt precipitation. Experimental work with and without a brine source was performed

and compared for the potential for formation clogging. The risk of contribution to salt precipitation from a confining fine-textured layer was studied.

Bibliography

Arts, R., Chadwick, A., Eiken, O., Thibeau, S., Nooner, S., 2008. Ten years' experience of monitoring CO2 injection in the Utsira Sand at Sleipner, offshore Norway. First break 26.

Bacci, G., Korre, A., Durucan, S., 2011. Experimental investigation into salt precipitation during CO2 injection in saline aquifers. Energy Procedia 4, 4450-4456.

Bachu, S., Bonijoly, D., Bradshaw, J., Burruss, R., Holloway, S., Christensen, N.P., Mathiassen, O.M., 2007. CO2 storage capacity estimation: Methodology and gaps. International Journal of Greenhouse Gas Control 1, 430-443.

Ebigbo, A., Class, H., Helmig, R., 2007. CO2 leakage through an abandoned well: problem-oriented benchmarks. Computational Geosciences 11, 103-115.

Eiken, O., Ringrose, P., Hermanrud, C., Nazarian, B., Torp, T.A., Høier, L., 2011. Lessons learned from 14 years of CCS operations: Sleipner, In Salah and Snøhvit. Energy Procedia 4, 5541-5548.

Fanchi, J.R., 2000. Oil and Gas in the Energy Mix of the 21st Century.

Fang, Y., Baojun, B., Dazhen, T., Dunn-Norman, S., Wronkiewicz, D., 2010. Characteristics of CO2 sequestration in saline aquifers. Petroleum Science 7, 83-92.

Grude, S., Dvorkin, J., Clark, A., Vanorio, T., Landrø, M., 2013. Pressure effects caused by CO2 injection in the Snøhvit Field. first break 31.

Hansen, O., Gilding, D., Nazarian, B., Osdal, B., Ringrose, P., Kristoffersen, J.-B., Eiken, O., Hansen, H., 2013. Snøhvit: The History of Injecting and Storing 1 Mt CO2 in the Fluvial Tubåen Fm. Energy Procedia 37, 3565-3573.

Holloway, S., 2005. Underground sequestration of carbon dioxide—a viable greenhouse gas mitigation option. Energy 30, 2318-2333.

Hosa, A., Esentia, M., Stewart, J., Haszeldine, S., 2011. Injection of CO2 into saline formations: Benchmarking worldwide projects. Chemical Engineering Research and Design 89, 1855-1864.

Korbøl, R., Kaddour, A., 1995. Sleipner vest CO2 disposal-injection of removed CO2 into the utsira formation. Energy Conversion and Management 36, 509-512.

Metz, B., Davidson, O., Bosch, P., Dave, R., Meyer, L., 2007. IPCC, 2007: Climate Change 2007: Mitigation. Contribution of Working Group III to the Fourth

Assessment Report of the Intergovernmental Panel on Climate Change. Cambridge University Press, Cambridge, United Kingdom and New York, NY, USA.

Metz, B., Davidson, O., De Coninck, H., Loos, M., Meyer, L., 2005. IPCC, 2005: IPCC special report on carbon dioxide capture and storage. Prepared by Working Group III of the Intergovernmental Panel on Climate Change. Cambridge, United Kingdom and New York, NY, USA, 442 pp.

Michael, K., Golab, A., Shulakova, V., Ennis-King, J., Allinson, G., Sharma, S., Aiken, T., 2010. Geological storage of CO2 in saline aquifers—A review of the experience from existing storage operations. International Journal of Greenhouse Gas Control 4, 659-667.

Muller, N., Qi, R., Mackie, E., Pruess, K., Blunt, M.J., 2009. CO2 injection impairment due to halite precipitation. Energy procedia 1, 3507-3514.

Peysson, Y., Andre, L., Azaroual, M., 2014. Well injectivity during CO2 storage operations in deep saline aquifers—Part 1: Experimental investigation of drying effects, salt precipitation and capillary forces. international journal of Greenhouse Gas Control 22, 291-300.

Pruess, K., Müller, N., 2009. Formation dry-out from CO2 injection into saline aquifers: 1. Effects of solids precipitation and their mitigation. Water Resources Research 45, W03402.

Schollnberger, W., 1998. Projections of the World's Hydrocarbon Resources and Reserve Depletion in the 21 st Century. Houston Geological Society Bulletin 41, 31-45.

Sengul, M., 2006. CO2 Sequestration-A safe transition technology, SPE International Health Safety & Environment Conference. Society of Petroleum Engineers.

Solomon, S., 2007. Climate change 2007-the physical science basis: Working group I contribution to the fourth assessment report of the IPCC. Cambridge University Press.

2

Key processes and governing equations

2.1. Multi-phase flow in a porous medium

2.1.1. General flow equations

We describe CO_2 injection into a brine-saturated porous medium by the mass balances for three phases, i.e. gaseous phase (g), aqueous phase or brine (w) and solid salt phase (s) and three components, namely carbon dioxide (CO_2), water (H_2O) and potassium iodide (KI). The porous medium is assumed to be incompressible and homogeneous. The components carbon dioxide (CO_2) and water (H_2O) can be present in the gaseous and brine phase and dissolved salt (KI) is only present in the brine phase. Solid salt is considered part of the pore space and does not experience advection nor diffusion. The solid salt phase consists of one component which is precipitated salt. To describe the flow process we use the balance of mass for phase α and component i:

$$\partial_t(\varphi\rho_\alpha S_\alpha X_\alpha^i) + \nabla\cdot(\rho_\alpha \boldsymbol{u}_\alpha X_\alpha^i) - \nabla\cdot(\varphi\rho_\alpha S_\alpha \boldsymbol{D}_\alpha^i \nabla X_\alpha^i) = \varphi\rho_\alpha S_\alpha Q_{\alpha\beta}^i + \varphi\rho_\alpha S_\alpha R_{\alpha\beta}^i \quad (1)$$

$$\alpha \in \{g, w, s\}, i \in \{CO_2, H_2O, KI\}$$

where φ (-) is the porosity, ρ (ML^{-3}) is the density, S (-) is the saturation, u (LT^{-1}) is the Darcy velocity, X (-) is the mass fraction, D (L^2T^{-1}) is diffusion within a phase, Q ($ML^{-3}T^{-1}$) is the evaporation rate and R ($ML^{-3}T^{-1}$) is the precipitation rate. Q is only valid for component H_2O from phase w to phase g, and R is only valid for component KI from phase w to phase s.

Flow is described by the Darcy's equations for multi-phase flow:

$$\boldsymbol{u}_\alpha = -\frac{\boldsymbol{K}k_{r\alpha}}{\mu_\alpha}(\nabla P_\alpha - \rho_\alpha \boldsymbol{g}) \quad (2)$$

$$\alpha \in \{g, w\}$$

where K (L^2) is the permeability of the porous medium, k_r (-) is the relative permeability, μ ($ML^{-1}T^{-1}$) is the dynamic viscosity, P ($ML^{-1}T^{-2}$) is the pressure and g (LT^2) is the gravitational acceleration. Note that since solid salt is immobile the Darcy's equation is only applicable to the gaseous and the brine phase. To complete the problem formulation we provide below the constitutive relations, i.e. the functional relations describing the dependence of the relative permeabilities on water saturation and the dependence of capillary pressure on water saturation.

2.1.2. Effective water saturation

For injection of CO_2 into a fully brine-saturated porous medium ($S_w = 1$), we consider a primary drainage process and the residual gas saturation equalizes zero. For primary drainage, the water saturation is normalized between the upper limit of complete saturation ($S_{wmax} = 1$) and the lower limit of connate water saturation ($S_w = S_{wc}$), resulting in the *effective water saturation*:

$$S_{we} = \frac{S_w - S_{wc}}{S_{wmax} - S_{wc}} \tag{3}$$

In this research, we assume that hysteresis does not affect the effective water saturation. Therefore, for imbibition Eq. 3 applies with $S_{wmax}=1$.

2.1.3. Relative permeability relations

The constitutive relations for the relative permeabilities are described by analytical or semi-empirical relations (Brooks and Corey, 1964; Van Genuchten, 1980; Parker) and pore-network modeling (Valvatne and Blunt, 2004). The relevant parameters are determined by fitting these relations to relative permeability data obtained by special core analysis (SCAL) methods. In this work, Brooks and Corey (Brooks and Corey, 1964) functional relations for relative permeability were used in order to describe the flow of CO_2 and brine in porous media:

$$\begin{aligned} k_{rw} &= k_{rw}^0 S_{we}^{(2+3n_w)/n_w} \\ k_{rg} &= k_{rg}^0 (1 - S_{we})^2 \left[1 - S_{we}^{(2+n_g)/n_g}\right] \end{aligned} \tag{4}$$

with k_{rg}^0 (-) and k_{rw}^0 (-) being the end-point relative permeabilities for CO_2 and brine, S_{we} (-) represents the effective water saturation and n_g (-) and n_w (-) are the fitting parameters for CO_2 and brine, respectively. The parameters for Bentheimer sandstone were obtained from relative permeability measurements for an oil-water drainage process and are listed in Table 2.1. In Chapter 4, Berea sandstone is used instead of Bentheimer, for which the parameters are listed in the relevant chapter. Below the residual saturation of brine the relation for relative permeability of gas is not well defined. In this study, we extend the formulation with a linear behavior for non-wetting phase relative permeability between the endpoint saturation and complete dry-out. We assume that hysteresis in the relative permeability functions can be neglected (Figure 2.1). The presence of solid salt is not taken into account in the relative permeability description.

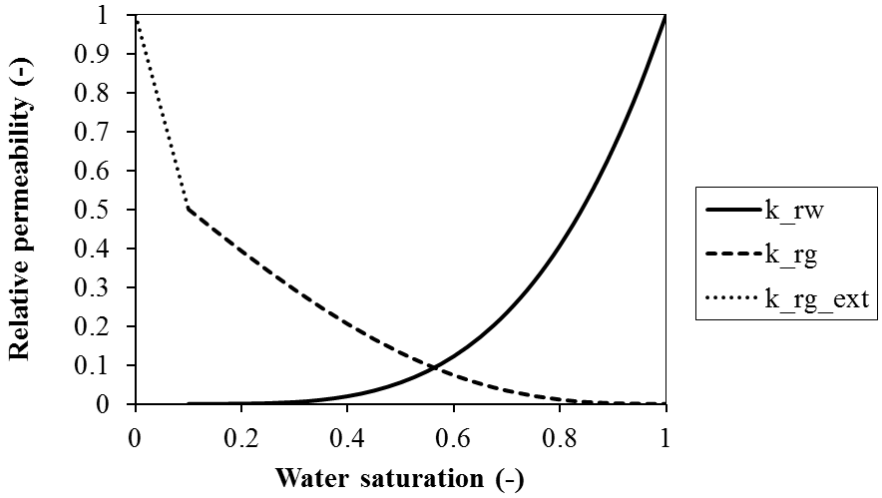

Figure 2.1. Relative permeability curves as a function of water saturation. The curve for CO_2 is extended linearly below connate water saturation.

Table 2.1. Simulation parameters Bentheimer.

Parameter	*Value*	*Unit*
k_{rw}^{0} *- Brooks and Corey*	1	-
k_{rg}^{0} *- Brooks and Corey*	0.5	-
n_w *- Brooks and Corey*	3.5	-
n_g *- Brooks and Corey*	1.5	-
P_d *– Van Genuchten*	3.3×10^4	Pa
m – Van Genuchten	0.85	-
Γ *– Verma and Pruess*	0.95	-
φ_r *– Verma and Pruess*	0.5	-
S_{wc}	0.1	-

2.1.4. Capillary pressure

For two-phase flow in porous media, capillary pressure refers to the pressure difference across the fluid-fluid interface between the non-wetting and wetting phase. In a water-wet porous medium, the attractive forces between the solid surface and the wetting phase (brine) dominate over the attractive forces between the non-wetting phase (CO_2) and the solid surface. As a result, during CO_2 injection in a

100% brine-saturated medium (primary drainage) a pressure difference builds up between CO_2 and brine resulting in a non-zero curvature of the interface. When a certain pressure difference (entry pressure) is reached, the interface starts to move and the pore fills with CO_2. Large pores drain at lower entry pressures than small pores so that capillary pressure is inversely proportional to the radius of the pore. On the core scale, the saturation distribution during two-phase flow displacement is highly affected by the strength of capillary forces. In this study, we describe the dependence of the capillary pressure on water saturation by the Van Genuchten equation (Van Genuchten, 1980):

$$P_c = P_d\left({S_{we}}^{-1/m} - 1\right)^{1-m} \tag{5}$$

where P_d (Pa) and m (-) are parameters that are fit to measured data. The parameters of the capillary pressure function for Bentheimer are listed in Table 2.1. They were obtained by fitting Eq.(5) to the capillary pressure data measured by mercury injection as shown in Figure 2.2. Typical functional relations work appropriately when saturations below the connate saturation of the wetting fluid are not considered. However, during CO_2 injection into a brine-filled porous medium the brine saturation will drop below its connate saturation due to evaporation of water molecules into the gaseous phase. For modeling purposes, we assume that capillary pressure is constant below connate water saturation.

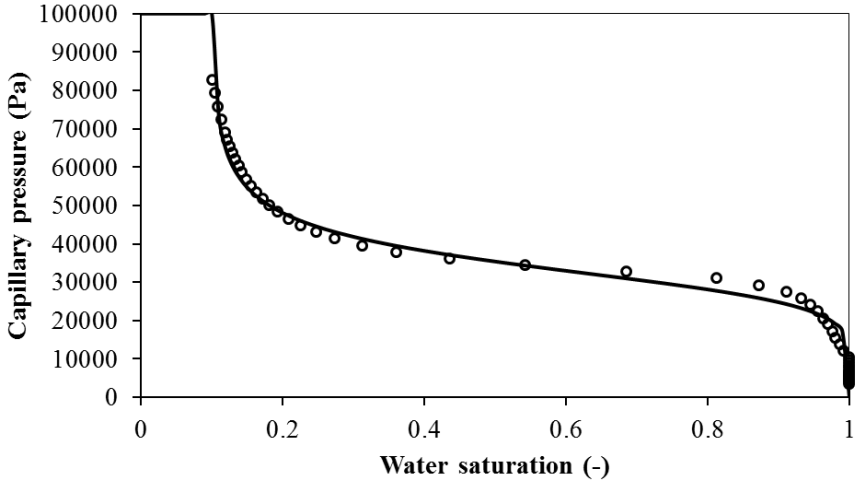

Figure 2.2. Capillary pressure-Water saturation curve. The symbols represent the mercury injection measurements in Bentheimer sandstone and the line represents the Van Genuchten equation. Pc is constant below connate water saturation.

2.1.5. Fluid densities

In the TOUGH2/ECO2N reservoir simulator, brine density for the binary system water-salt is calculated as in Battistelli et al. (1997) from the correlations of Haas (1976) and Andersen et al. (1992). The calculation starts from aqueous phase density without salinity at vapor-saturated conditions, which is obtained from the correlations given by the International Formulation Committee (1967). Corrections are then applied to account for effects of salinity and pressure. The density of the CO_2-rich (gas) phase is obtained by neglecting effects of water, and approximating the density by that of pure CO_2 at the same temperature and pressure conditions. Density is obtained through bivariate interpolation from a tabulation of CO_2 densities as function of temperature and pressure, that is based on the correlations developed by Altunin (1975).

In the numerical code developed in this study we assumed densities of CO_2 and brine to be constant at the value for ambient pressure and temperature. This assumption was considered valid, because in the core-flooding experiments the temperature was kept constant and pressure changes were minor due to the small sample sizes. The brine density was obtained from measurements with a density-meter (Anton Paar DMA Generation M) and the CO_2 density was found from the National Institute of Standard and Technology (NIST).

2.2. Evaporation of water into the gaseous phase

2.2.1. Solubility limits

CO_2 injection into a brine-saturated porous medium leads to physical and chemical disequilibria. The spatial and temporal distribution of the CO_2-rich gaseous phase and the dissolution kinetics give rise to gradients in the Gibbs free energy as it induces spatial variations of pressures (viscous pressure drop and capillary pressure) and concentration (Sandler, 2006). The system tends to minimize Gibbs free energy by redistributing fluid phases and molecules within the phases in the direction of decreasing chemical potential. This results in mass-transfer within phases and between phases on all involved length scales. Since the Gibbs free energy increases linearly with concentration, the molecules tend to move from areas with high concentration to areas of low concentration until the free energy reaches its minimum, i.e. until equilibrium is reached (Sandler, 2006).

Solubility limits of water vapor in CO_2 and of CO_2 in brine were measured by Spycher and Pruess (2005) for a range of temperatures and pressures. Below the critical temperature, a sharp discontinuity was observed in the solubility of H_2O in CO_2, which coincides with a phase change from a gaseous to a liquid CO_2-rich phase (Spycher et al., 2003). Water evaporation into the gaseous CO_2-rich phase decreases

with increasing pressure but, on the contrary, water solubility in liquid CO_2 increases with pressure (Spycher et al., 2003). Mutual solubilities diminish with increasing salinity, although this effect is more pronounced for CO_2 solubility in brine. Under experimental conditions used in Chapter 3, 5 and 6, ambient temperature and atmospheric pressure, the solubility limit of CO_2 in brine is negligible, while water solubility limit in gaseous CO_2 phase is relatively high, with a mass fraction of at least 1.2% (Spycher and Pruess, 2005; Spycher et al., 2003). In Chapter 4, we discuss these effects for CO_2 injection at reservoir conditions of 100 bar/45°C.

2.2.2. Mass transfer formulation

In order to model water evaporation, i.e. the mass transfer of water from the aqueous phase to the gaseous phase, we use (Pinder and Celia, 2006):

$$Q_\alpha^i = k_\alpha^i \left(X_\alpha^{i,max} - X_\alpha^i\right) \tag{6}$$

where k_α^i (T^{-1}) is the mass transfer rate coefficient, $X_\beta^{i,max}$ (-) is the solubility limit of component *i* in phase α and X_β^i (-) is the actual mass fraction of component *i* in phase α. In this research, it was assumed that the mass transfer rate coefficient, k_α^i, is a constant and does not depend on interfacial area, injection velocity or other factors that might affect evaporation. Correlations between interfacial area and mass transfer rate are available in the literature (Niessner and Hassanizadeh, 2009), but require extensive information on parameter values which are not available for our system. For this reason, we chose to assume a constant evaporation rate.

2.3. Modeling of salt precipitation

2.3.1. Nucleation and crystal growth

Water evaporation into the CO_2-rich phase increases salt concentration in the brine phase. Continuous injection of CO_2 may therefore eventually lead to super-saturation of the brine and subsequently precipitation of salt in the porous medium. Salt crystals can grow inside the porous medium, a phenomenon called *subflorescence*, or at the external water film in the injection well which is referred to as *efflorescence*. Whether salt crystals will precipitate in smaller or larger pores is difficult to predict. Since larger pores drain at lower entry pressures than smaller pores, and evaporation increases the concentration inside the pores, salt is more likely to precipitate in the smaller pores (Scherer, 2004). On the other hand, as nucleation can start in any pore (all pores have heterogeneities that can function as

nucleation points), two adjacent pores with different sizes can growth crystals until super-saturation has been consumed. It was found that smaller salt crystals are in equilibrium with a higher dissolved salt concentration than larger crystals (Cahn, 1980). Therefore, solute content is higher in the small pore and will dissolve toward the larger pores, and enhance salt crystal growth in the larger pores (Scherer, 2004).

2.3.2. Salt precipitation formulation

Similar to the mass transfer equation (Eq. (6)), precipitation can be described as a function of a precipitation rate coefficient the difference between solubility limit and actual mass fraction:

$$R_\alpha^i = -r_\alpha^i \left(X_\alpha^i - X_\alpha^{i,max}\right) \tag{7}$$

where r_α^i (-) is the precipitation rate coefficient. In this case, however, the driving force is the solubility limit in the 'providing' phase and not in the 'receiving' phase. In the simulations reported in this work, instantaneous salt precipitation was assumed above the solubility limit of dissolved salt in water. Different implementations were used to achieve instantaneous precipitation, depending on the software used in this research. In general, stating that precipitation occurs instantaneously implies that r_α^i tends to infinity. For modeling purposes, the mass balance equations are summed over the components and the mass transfer terms cancel out (Pinder and Celia, 2006). Otherwise, we used a very high precipitation rate in order to achieve quasi-instantaneous precipitation.

2.3.3. Effect of salt precipitation on porosity and permeability

Since precipitated salt occupies a fraction of the pore space it results in the decrease in permeability. The following correlation of Verma and Pruess (1988a) was used to describe the effect of salt precipitation on permeability:

$$\frac{K}{K_0} = \theta^2 \frac{1 - \Gamma + \frac{\Gamma}{\omega^2}}{1 - \Gamma + \Gamma\left[\frac{\theta}{\theta + \omega - 1}\right]^2} \tag{8}$$

$$\theta = \frac{1 - S_s - \varphi_r}{\varphi_r} \tag{9}$$

$$\omega = 1 + \frac{1/\Gamma}{1/\varphi_r - 1} \tag{10}$$

where K (L^2) is the permeability of the porous medium, K_0 (L^2) is the initial rock permeability, S_S (-) is the solid salt saturation, Γ (-) is the fractional length of the pore bodies and φ_r (-) is the fraction of the original porosity for which the permeability reduces to zero. This relation represents a model that can capture the converging-diverging nature of natural pore channels consists of alternating segments of capillary tubes with larger and smaller radii, respectively. While in straight capillary tube models permeability remains finite as long as porosity is non-zero, in models of tubes with different radii in series, permeability is reduced to zero at a finite porosity (φ_r). Parameters Γ and φ_r were chosen based on the measured permeability at the end of the experiment in Chapter 3 and are listed in Table 2.1.

Bibliography

Altunin, V., 1975. Thermophysical properties of carbon dioxide. Publishing House of Standards Moscow Russia.

Anderson, G., Probst, A., Murray, L., Butler, S., 1992. An Accurate PVT Model for Geothermal Fluids as represented by H2OCO2-NaCl Mixtures, Proc. 17th Workshop on Geothermal Reservoir Engineering.

Battistelli, A., Calore, C., Pruess, K., 1997. The simulator TOUGH2/EWASG for modelling geothermal reservoirs with brines and non-condensible gas. Geothermics 26, 437-464.

Brooks, R., Corey, T., 1964. Hydraulic Properties of Porous Media.

Cahn, J.W., 1980. Surface stress and the chemical equilibrium of small crystals—I. The case of the isotropic surface. Acta Metallurgica 28, 1333-1338.

Haas Jr, J., 1976. Thermodynamics properties of the coexisting phases and thermochemical properties of the NaCl component in boiling NaCl solutions. US, Geol. Surv., Bull.;(United States) 1421.

International Formulation Committee, I., 1968. The 1968 IFC Formulation for Scientific and General Use a Formulation of the Thermodynamic Properties of Odinary Water Substance, April 1968 and Thermodynamic Property Values of Ordinary Water Substance Calculated from the 1968 IFC Formulation for Scientific and General Use, April 1968. ASE.

Niessner, J., Hassanizadeh, S.M., 2009. Modeling kinetic interphase mass transfer for two-phase flow in porous media including fluid–fluid interfacial area. Transport in porous media 80, 329-344.

Parker, J., Lenhard, R., Kuppusamy, T., 1987. A parametric model for constitutive properties governing multiphase flow in porous media. Water Resources Research 23, 618-624.

Pinder, G.F., Celia, M.A., 2006. Subsurface hydrology. John Wiley & Sons.

Sandler, S.I., 2006. Chemical, biochemical, and engineering thermodynamics. John Wiley & Sons Hoboken, NJ.

Scherer, G.W., 2004. Stress from crystallization of salt. Cement and Concrete Research 34, 1613-1624.

Spycher, N., Pruess, K., 2005. CO2-H2O mixtures in the geological sequestration of CO2. II. Partitioning in chloride brines at 12–100° C and up to 600 bar. Geochimica et Cosmochimica Acta 69, 3309-3320.

Spycher, N., Pruess, K., Ennis-King, J., 2003. CO2-H2O mixtures in the geological sequestration of CO2. I. Assessment and calculation of mutual solubilities from 12 to 100° C and up to 600 bar. Geochimica et Cosmochimica Acta 67, 3015-3031.

Valvatne, P.H., Blunt, M.J., 2004. Predictive pore-scale modeling of two-phase flow in mixed wet media. Water Resources Research 40.

Van Genuchten, M.T., 1980. A closed-form equation for predicting the hydraulic conductivity of unsaturated soils. Soil science society of America journal 44, 892-898.

Verma, A., Pruess, K., 1988. Thermohydrological Conditions and Silica Redistribution Near High-Level Nuclear Wastes Emplaced in Saturated Geological Formations. J. Geophys. Res. 93, 1159-1173.

3

μ-CT analysis and numerical simulation of CO_2 injection into brine-saturated sandstone

Abstract

CO_2 injection in brine-saturated Bentheimer sandstone was studied experimentally to visualize and quantify salt precipitation in porous rock caused by evaporation of water into injected gaseous phase CO_2. Gas and solid-salt saturation profiles were captured by µ-CT (micro computed tomography) and the pressure drop over the core was monitored continuously. The experimental results were compared with numerical simulations using the TOUGH2 reservoir simulator with the equation of state module ECO2N, and a numerical code that we have developed with an alternative approach on evaporation. Using the equilibrium phase partitioning model in TOUGH2, simulation results predict injectivity decline due to an accumulation of precipitated salt near the core inlet. This is in contradiction to our experimental observations, in which neither salt accumulation nor injectivity impairment was noticed. It appears that at near well injection velocities, local equilibrium phase partitioning used in the simulator overestimates evaporation of water into the CO_2 gaseous phase. On the other hand, satisfying results were obtained from our model which uses a kinetic formulation for the evaporation. No injectivity impairment was found which is compatible with the experimental results.

[Based on: Roels, S.M., Ott, H., Zitha, P.L.J., 2014. µ-CT analysis and numerical simulation of CO_2 injection into brine-saturated sandstone. Int. Journal of Greenhouse Gas Control 27, 146-154.]

3.1. Introduction

Atmospheric CO_2 concentration increased by 35% over the last two centuries, and is expected to double over the next 50 years (Metz et al., 2007). Accumulation of CO_2 in the atmosphere is an important contribution to global warming. Since a large fraction of the atmospheric CO_2 increase arose from anthropogenic activities, society as a whole must act to mitigate this development. One of the most promising options for reducing CO_2 emissions is referred to as carbon capture and storage (CCS). This technique concerns the capture and purification of CO_2 emissions from anthropogenic sources, subsequent compression and transport, and ultimately the storage of CO_2 in deep geological formations. One critical outstanding scientific issue is the identification of geological formations suited for long-term storage safety. It has become the favored option to store CO_2 in saline aquifers, rather than depleted oil or gas fields, due to their potential for high storage capacities (Fang et al., 2010).

However, several numerical studies on CO_2 storage in saline aquifers have predicted injectivity loss due to formation dry-out (e.g. Fuller et al., 2006; Giorgis et al., 2007; Muller et al., 2009; Pruess and Garcia, 2002; Pruess and Müller, 2009a). Water and CO_2 either in gaseous or supercritical state, are mutually soluble. As CO_2 is injected into a saline aquifer it will therefore eventually vaporize water of the resident brine phase. This will lead to super-saturation of the brine and consequently precipitation of salt in the porous medium, also known as subflorescence, which reduces formation porosity and possibly permeability. It is well accepted that permeability is sensitive to porosity variation (e.g. Pape et al., 1999) and there is theoretical (e.g.Verma and Pruess, 1988a) and experimental (Bacci et al., 2011; Ott et al., 2012) evidence that porosity reduction due to precipitation leads to substantial reduction of permeability. When brine saturation decreases due to evaporation, capillary forces increase and can act as a driving force for brine to flow from higher saturations toward dryer zones. As long as the liquid is connected to the bulk phase, advective transport of dissolved salt is possible and may lead to salt accumulation in the near wellbore zone. Severe reduction in injectivity caused by salt accumulation was found by numerical studies using TOUGH2 with different modules such as ECO2N (André et al., 2013; Muller et al., 2009; Pruess and Müller, 2009a), EWASG (Lorenz and Müller, 2003) and TMGAS (Giorgis et al., 2007). In case of immobile brine present during CO_2 injection, evaporation leads to low values of precipitated salt reaching relatively far into the reservoir (Tambach et al., 2014). Other research suggested preventing leakage along the wellbore by intentional salt clogging through brine-alternating CO_2 injection (Wasch et al., 2013).

Permeability reduction varying from 30 to 60% caused by salt precipitation was also found in several experimental studies (Bacci et al., 2011; Muller et al., 2009;

Peysson, 2012; Wang et al., 2009; Zuluaga et al., 2002). However, reduced permeability does not necessarily lead to impairment in injectivity (Ott et al., 2012). Two counteracting processes affect the pressure drop: (1) an increase in CO_2 relative permeability due to an increase in CO_2 saturation decreases the pressure drop and (2) precipitation of salt in the pore space decreases the rock permeability and therefore increases the pressure drop. The authors found that increase in CO_2 relative permeability, due to decrease in brine saturation, is able to compensate for the decrease in rock permeability. Furthermore, it was hypothesized that salt precipitated at the edges of the CO_2-pathways leaving a cross-sectional area open for flow. This was also found in evaporation studies with brine-air systems where salt predominantly precipitated in the low permeable zones which drew solution from the high permeable zones by capillary forces (PiPujol and Buurman, 1997; Scherer, 2004), creating a pathway open for gas flow (Nachshon et al., 2011). It was found by (Ott et al., 2011) that an injection velocity above a certain critical value may result in a uniform salt distribution whereas during a lower injection velocity the balance of forces may allow brine to redistribute, resulting in a local accumulation of salt.

Recently, another explanation for the absence of salt accumulation was given by Peysson et al. (2014). Experimental results showed that in case of low Péclet numbers, evaporation is slow compared to diffusion of salt in brine and the dissolved salt concentration will stay in equilibrium during the entire experiment. This may lead to a flat salt deposition profile. The opposite effect was observed for high Péclet numbers, with salt accumulation near the inlet.

In this study, we aim to explain the discrepancy between experimental and modeling results regarding salt precipitation. It is of great importance to understand the salt precipitation mechanisms during CO_2 storage processes, because based on contemporary numerical simulations potential storage sites will be rejected due to clogging predictions. Laboratory flooding experiments were performed in which CO_2 was injected into brine-saturated sandstones. Quantification of solid salt was done by a pore-scale visualization of precipitated salt using a Phoenix Nanotom µ-CT X-ray scanner. The results were compared to numerical simulations using the reservoir simulator TOUGH/ECO2N, which is widely used for modeling CO_2 sequestration, and a code that we have developed which approaches the evaporation process with a kinetic formulation. First, the physical concept of displacement and capillary-driven flow will be discussed. Next, the experimental set-up and procedure will be explained, followed by a presentation and discussion of the numerical and experimental results. At last the main conclusions of this study are presented.

3.2. Propagation of CO2 phase and dry-out

3.2.1. Displacement regime

Displacement of one phase by another in a homogeneous porous medium can be dominated by either capillary, viscous or gravity forces, depending on the system dimensions, rock and fluid properties. The balance between these forces determines whether a stable displacement or viscous fingering will occur (Lenormand et al., 1988). In case of a stable displacement with favorable mobility ratio, the resident fluid will be efficiently displaced by the injected fluid on a macroscopic scale (sweep efficiency) without bypassing of rock matrix. As a consequence, the remaining resident fluid saturation will only be determined by the microscopic displacement efficiency (Lake, 1989) and a low remaining saturation is expected. In case of unstable displacement, a fraction of the porous medium will be bypassed and the experimental results would depend on the exact fluid distribution in the rock. Hence it is important to investigate the stability of the displacement process, since a generally valid result can only be derived from a stable flood.

In order to analyze the stability of the displacement process in the experiments, we evaluated the macroscopic capillary number (Hilfer and Øren, 1996), shock-front mobility ratio (Berg and Ott, 2012; Riaz and Tchelepi, 2006) and gravity number (Anton and Hilfer, 1999; Riaz and Tchelepi, 2004) which can be expressed by the following formulations respectively:

$$N_{cap} = \frac{u_t \mu_{CO_2} L}{\bar{P}_c K} \tag{11}$$

$$M = \frac{k_{r,CO_2}(S_{shock})/\mu_{CO_2}}{k_{r,brine}(S_{brine} = 1)/\mu_{brine}} \tag{12}$$

$$N_{grav} = \frac{\Delta\rho g K}{\mu_{CO_2} u_t} \tag{13}$$

where u_t is the linear flow velocity, μ_{CO_2} is the viscosity of CO_2, L is the length of the domain, K is the rock permeability, $k_{r,CO_2}(S_{shock})$ is the relative permeability of CO_2 at shock front saturation and $k_{r,brine}(S_{brine} = 1)$ is the brine relative permeability at initial brine saturation (unity for primary drainage), and $\Delta\rho$ is the density difference between CO_2 and brine. $\bar{P}_c$ is the capillary pressure at breakthrough saturation $\bar{P}_c = P_c(S_{shock})$ (Hilfer and Øren, 1996) or as a characteristic value described by $\bar{P}_c = P_c\left[\left(S_{wc} - S_{gr} + 1\right)/2\right]$, i.e. the plateau value (Anton and Hilfer, 1999).

With the parameters listed in Table 2.1 and 3.1, we find that $N_{cap} = 1.3 \times 10^{-2}$ and $1.0 \times 10^{-2} \ll 1$ for both formulations of $\bar{P}_c$ respectively, which indicates that capillary forces dominate over viscous forces. The shock front saturation, end point values, formulation and parameters used in the relative permeability functions can result in significantly different values for mobility ratio, *M*, as was found by others (Riaz and Tchelepi, 2006). In this study we found $M = 8.7$, which indicates unstable displacement with viscous fingering. The gravity number represents the influence of gravitational forces relative to viscous forces. It was found to be $N_{grav} = 1.2 \sim 1$, which indicates a balance between gravitational and viscous forces.

Summarizing, the mobility ratio predicts an unstable displacement by viscous fingering in absence of capillary and gravity forces. However, the capillary number, $N_{cap} \ll 1$, indicates a stable displacement front on the length scale considered in this study (Berg and Ott, 2012). In addition, gravity stabilized the flood due to the vertical top-down flow geometry, resulting in a stable displacement. However, the efficiency of CO_2-brine displacement is low due to the low CO_2-brine viscosity ratio. Consequently, we expect a high remaining brine saturation after CO_2 breakthrough.

The $P_c = 0$ boundary condition at the outlet leads normally to a non-uniform water saturation in the core. This so-called capillary end-effect should be taken into account for an accurate description of the displacement of wetting phase by non-wetting phase in porous media (Huang and Honarpour, 1998). The capillary end effect hinders further production of brine and causing large remaining brine saturation near the core outlet.

Table 3.1. System and fluid properties.

Property	*Value*	*Unit*
μ_{brine}	0.000891	Pa·s
μ_{co2}	0.000015	Pa·s
u_t	0.0011	m/s (Q = 5 mL/min)
L	0.03	m
$\Delta\rho$	1750	kg/m^3
g	9.81	m/s^2
S_{shock}	0.25	-
K	1.13×10^{-12}	m^2

3.2.2. Salt precipitation and accumulation

Solid salt may block a fraction of the pore space which was initially open for fluid flow and may therefore cause permeability to decrease. Simulations have shown that a reduction in injectivity can be caused by the precipitation of salt in the porous medium, especially in the vicinity of the wellbore where large amounts of dry CO_2 are injected into the aquifer (Muller et al., 2009).

An important consequence of desaturation due to evaporation is increase in capillary suction which might result in counter-current imbibition of brine in upstream direction. The principle of capillary-driven backflow can be readily understood by considering the fractional flow formulation for water including capillary pressure (Dong and Dullien, 1997):

$$u_w = u_t f_w = u_t \frac{\lambda_w}{\lambda_w + \lambda_g}\left(1 + \frac{\lambda_g}{u_t}\frac{dP_c}{dS_w}\frac{\partial S_w}{\partial x}\right) \qquad (14)$$

where u_w is the Darcy velocity for water, f_w is the fractional flow for water, u_t is the total velocity, $\lambda_g = Kk_{rg}/\mu_g$ is the gas mobility and $\lambda_w = Kk_{rw}/\mu_w$ is the water mobility, P_c is the capillary pressure and S_w is the water/brine saturation. The equation consists of a viscous flow term and a capillary flow term, where the derivative dP_c/dS_w is negative and the direction of brine flow is determined by the dominancy of either viscous or capillary-driven flow.

Capillary-driven backward flow of brine towards the injection well sustains salt transport towards the drying front. As evaporation continues, an accumulation of salt in the near wellbore region will further decrease aquifer permeability. On the other hand, a local super-saturation of brine creates a gradient in salt concentration which causes the dissolved salt to diffuse away from the drying front (Peysson, 2012; Peysson et al., 2013). Whether diffusion of salt can reduce salt accumulation near the inlet can be evaluated by the Péclet number:

$$Pe = \frac{L\rho_g X_g^{w,max} u_g}{\rho_w \varphi D} \qquad (15)$$

where ρ_g (ML^{-3}) is CO_2 density, ρ_w (ML^{-3}) is brine density, φ (-) is porosity, D (LT^{-2}) is the diffusion coefficient, u_g (LT^{-1}) is the gas velocity and $X_g^{w,max}$ (-) is the solubility limit of water vapor in CO_2. If we assume the diffusion coefficient to be in the order of 10^{-9} m^2/s, we find that Pe<<1, which means that diffusion dominates over advection and negatively affects accumulation of salt near the inlet.

3.3. Numerical simulations

3.3.1. Model description

The model consists of a one-dimensional domain with gravity pointing in the direction of flow. The domain is initially fully saturated with brine, which is close to the saturation limit with respect to solutes. At $t=0$, CO_2 injection starts from one side of the domain with a constant flow rate. The outlet is represented by a Dirichlet boundary condition of zero capillary pressure. This means that the last grid-block of the modeling domain is adjacent to the last grid-block containing the porous medium and has constant properties for all time-steps. Gas outflow at the outlet can occur due to the difference in pressure over the outlet (i.e. over the second to last and last grid blocks). The parameters used for the simulation can be found in Tables 2.1, 3.1 and 3.2. Some parameters were measured during the experiment and others are typical values for Bentheimer sandstone found in literature. The porous medium was assumed to be incompressible. To describe the effect of salt precipitation, i.e. decrease in porosity, on permeability Eq.(8-10) were used (Verma and Pruess, 1988a).

3.3.2. TOUGH2/ECO2N

TOUGH2 is a non-isothermal multiphase, multicomponent reservoir simulator. Combined with the ECO2N module (Pruess, 2005) it covers the thermodynamic properties of pure fluids as well as brine-CO_2 mixtures and is widely used for modeling of geological CO_2 storage in aquifers. The simulator uses a local equilibrium phase partitioning and mass fraction of water in the CO_2 phase is calculated according to its solubility limit at a certain pressure, temperature and salinity (Spycher and Pruess, 2005).

3.3.3. Non-equilibrium phase partitioning

The model developed in this study uses a mass transfer formulation between brine and CO_2 as described in Eq.(6). The mass transfer rate coefficient, k_α^i, was obtained by matching the model to the experimental data. The mass-transfer coefficient k_α^i is an effective parameter for the specific rock-fluid system. For convenience, a few assumptions are made in this model. Due to the small length of the core, and hence the small pressure drop, densities of both CO_2 and brine were assumed to be constant. Viscosities of brine and CO_2 were also assumed to be constant, which was considered valid because of isothermal conditions. Densities and salt solubility limit were adjusted when the results were compared to TOUGH2 simulations (NaCl-solution) and experimental results (KI-solution).

For this problem an IMPEM method was used in order to avoid material balance errors (Doster et al., 2014; Farkas, 1998). In this approach, the system is directly

solved for the masses of both phases, which are conserved quantities. However, we will find volume balance errors which have to be corrected for in every time-step.
The pressure equation and transport equations are decoupled and are solved implicitly and explicitly, respectively (Doster et al., 2014). Since densities of both CO_2 and brine were assumed to be constant, the total flow rate is assumed to be constant and the gas and brine velocities can be obtained from the Darcy's equation. The transport equations solve for the masses of brine, gas and water vapor in gas in an upstream weighting scheme, taking capillary-driven backflow into account. From the masses, the saturations and mass fractions are extracted, obeying the solubility limits for both water vapor fraction and dissolved salt fraction.

Table 3.2. Simulation parameters

Parameter	*Value*	*Unit*
Porosity	0.24	-
Initial pressure	1.01325e5	Pa
Temperature	28	°C
Klinkenberg parameter	1.17e-5	1/Pa
Injection rate	0.0019	$(kg/s)/m^2$
Initial salt mass fraction (NaCl)	0.26	-
Initial salt mass fraction (KI)	0.59	-
Verma and Pruess - Phi	0.5	-
Verma and Pruess - Gamma	0.2	-
Mass transfer rate coefficient	0.04	s^{-1}

3.4. Experiments

3.4.1. Fluids and porous media

Brine consisting of a nearly saturated potassium iodide (KI) solution (58.3 wt%) was used to conduct the experiments. KI has a high X-ray attenuation coefficient due to its high density and mass number and enhances the contrast between the CO_2 and brine. In this way optimal CT-scanning results were obtained.

The flooding experiment was performed in a homogeneous Bentheimer sandstone core with a diameter of 1.0±0.1 cm and a length of 3.0±0.1 cm. The composition of the Bentheimer sandstone is shown in Table 3.3 (Van Hemert et al., 2013). Gas and brine permeability were measured in the core-flood set-up by injecting at different flow rates and were found to be 2.0±0.1 D and 1.1±0.1 D, respectively.

Table 3.3. Mineral composition of Bentheimer sandstone as determined from XRD and XRF measurements (Van Hemert et al., 2013).

Mineral	*Weight %*
Quartz	91.70
Kaolinite	2.50
Montmorillonite	0.18
Orthoclase	4.86
Dolomite	0.26
Calcite	0.15
Hematite	0.16
Rutile	0.03
Pyrite	0.01
Ca-phosphate	0.07
Halite	0.03

3.4.2. Experimental set-up

The experimental set-up especially designed for this study is shown schematically in Figure 3.1. A vessel with CO_2 of 99.7% purity was connected to a Quizix-pump to inject CO_2 into the sample from top to bottom. An ISCO-pump was used for injecting brine from the bottom of the core. The pumps were placed outside of the µ-CT scanner and were connected with the core holder placed inside the scanner using nylon tubing. In this way, the entire core flooding experiment could be carried out with the core-holder inside the µ-CT scanner. The PEEK core holder and the sandstone core were especially designed such that they could be positioned vertically in the Nanotom µ-CT scanner. Every few hours a 3D scan was taken without interrupting the flooding process. Absolute pressure and pressure drop were measured using pressure-transducers. Temperature was measured using a 2-wire thermocouple with an accuracy of 0.1°C. Pressure transducers and thermocouple were connected to a data acquisition system and monitored continuously. The experiments were performed under ambient temperature and with atmospheric back-pressure.

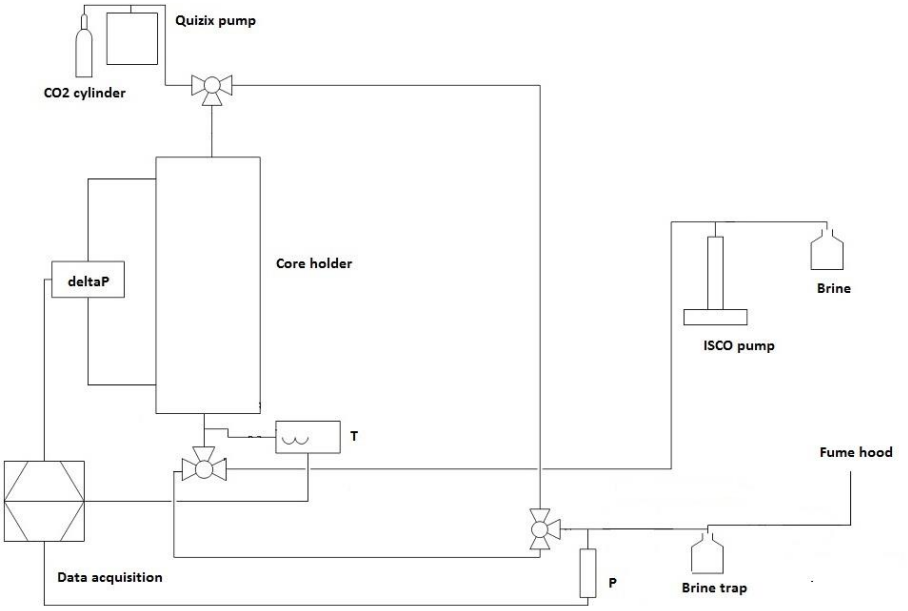

Figure 3.1. Schematic of experimental set-up.

3.4.3. Procedure and data processing

After pre-flushing the core with CO_2 to remove air, the core was filled with brine with 2 mL/min until approximately 10^4 pore volumes were injected. This large water volume is in excess of the calculated volume required to dissolve and remove any CO_2 present in the sample at atmospheric pressure. After the core was completely saturated with brine, CO_2 injection was started from the top of the core at a rate of 5 mL/min. Gas permeability was measured before and after the experiment and brine permeability was measured before the experiment. The experiment was tested on repeatability by being executed multiple times under similar conditions.

µ-CT scanning data are inherently noisy and precautions must be taken to minimize sources of error. Therefore settings of the µ-CT were optimized to obtain the best visualization and the most accurate quantification possible. The spatial resolution was 15 µm, which is a compromise between the best spatial resolution, total scan time (35 minutes) and a maximum field of view. The µ-CT scans were reconstructed with the phoenix reconstruction software which is based on the Feldkamp algorithm (Feldkamp et al., 1984). It converts the attenuation coefficients obtained from the scans directly to a gray value scale. The porosity was obtained from the dry scan taken prior to the experiment. The reconstructed CT-images were processed using in-house code written in MATLAB®. Threshold values were determined to

distinguish between materials in order to construct saturation profiles. The solid salt and gas saturations were quantified in terms of fraction of pore space per slice.

3.5. Results and discussion

In this section, we present results of the numerical modeling and the core-flood experiments on dry-out and salt precipitation. First, gas and solid-salt saturations and the pressure drop over time predicted by the local equilibrium (TOUGH2/ECON) and kinetic evaporation models are presented and compared. Then, the experimental data obtained from the µ-CT scanning will be presented and compared to the kinetic model modified for KI.

3.5.1. Numerical results

3.5.1.1. Gas and solid salt saturations

Figure 3.2 shows CO_2 saturations along the domain at different time steps obtained from the TOUGH2 simulator and the kinetic evaporation rate model. The breakthrough of CO_2 occurs after approximately 1.5 s. In line with our stability analysis (see section 3.2.1.) a typical behavior for viscous displacement of a high viscosity fluid by a low viscosity fluid can be observed, i.e. the front saturation is low. The capillary end effect imposed by the boundary condition ($P_c=0$) is shown by the lower gas saturation near the outlet. At later times, viscous displacement does not have a significant effect anymore and dry-out is completely dominated by evaporation. After 4.86 hours of injection the TOUGH2 simulation was aborted because the permeability at the inlet was reduced to zero. Capillary forces induce transport of brine towards the evaporation front at the inlet where solid salt accumulates (see Figure 3.3). The decrease in CO_2 saturation at the inlet is caused by an increase in solid salt saturation as numerical formulation accounts for solid salt as a fraction of pore space.

The kinetic rate model shows a complete dry-out process of the domain. The low evaporation rate prevents the injected CO_2 from becoming saturated with water vapor and therefore dry-out takes place along the entire core length. Again, a gas saturation of approximately 0.8 represents a dry domain as the remaining part of the pore space is occupied by solid salt. With the applied evaporation rate, the domain is completely dry after 17.5 hours of injection.

The solid salt profiles after dry-out predicted by the two models are shown in Figure 3.3. The TOUGH2 model predicts a precipitation profile in which all salt accumulates at the inlet of the domain. The instantaneous phase partitioning between brine and gas decreases the brine saturation dramatically near the inlet of the domain and capillary-driven backflow of brine towards the injection side is stimulated. This

leads to continuous advective transport of dissolved salt towards the inlet. Through the Verma and Pruess formulation (Verma and Pruess, 1988a) it was assumed that permeability reduces to zero as soon as the pore space reduces to 50%. This means that the maximum amount of salt has precipitated near the inlet and the simulation is aborted. The results show that even for low Péclet numbers, numerical simulation including a local equilibrium phase partitioning predicts salt accumulation near the inlet.

The kinetic rate model shows a generally flat solid salt profile when dry-out has been reached. Due to the uniform evaporation along the length, only a weak gradient in brine saturation was established, resulting in a slightly higher salt precipitation near the inlet.

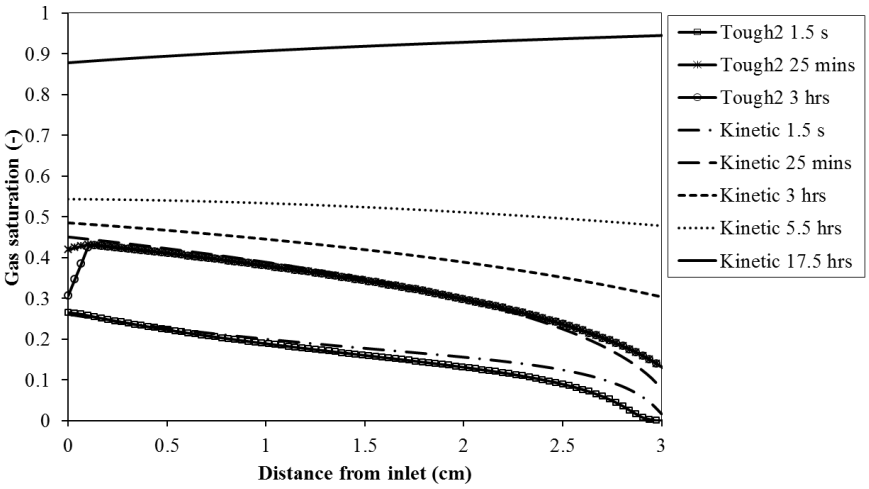

Figure 3.2. CO_2 saturation along the core at different time steps during displacement of brine by CO_2 as predicted by TOUGH2 and the kinetic model. The TOUGH2 simulation is aborted after 3 h of injection due to clogging of the inlet. Dry-out times for the kinetic model reach 17.5 h.

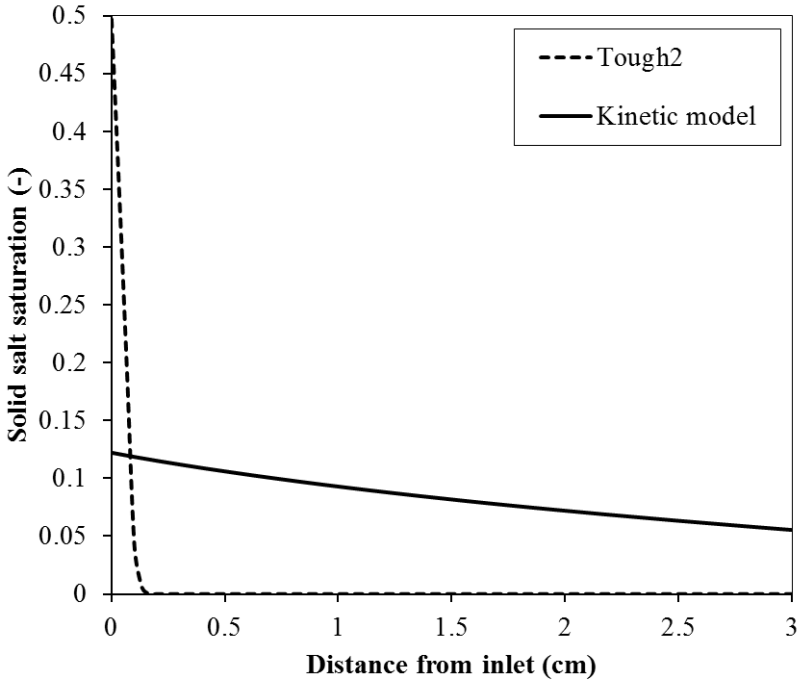

Figure 3.3. Solid salt at the end of the simulations. TOUGH2 predicts salt accumulation near the inlet compatible with full clogging. The kinetic model predicts a nearly uniform salt profile consistent with much smaller impairment of permeability.

3.5.1.2. Pressure drop and permeability reduction

The pressure drop over the domain versus time is shown in Figure 3.4. After CO_2 breakthrough which occurs a few seconds after injection starts, pressure drop falls dramatically for both models in line with a dominantly viscous displacement of the brine phase. In the TOUGH2 model, the pressure drop remains constant for approximately 4 hours. During this period, the reduction in rock permeability due to the formation of solid salt seems to be balanced by the increase in CO_2 relative permeability. After 4 hours a rapid increase in pressure drop takes place. This is caused by the accumulation of salt near the inlet of the domain as described in section 3.2.2.

In contrast, in the kinetic model the decrease in pressure drop continues until the domain is dry. During this stage CO_2 saturation and hence CO_2 relative permeability increase predominantly due to evaporation of water, i.e. the evaporation rate is higher than the viscous displacement rate. Because the salt is not transported throughout the core due to capillary forces, it simply precipitates in the pore space previously filled by remaining brine. At 12 hours, brine drops below its residual

saturation and the relative permeability curve changes slope, which affects the pressure drop directly. After 17.5 hours of CO_2 injection the domain is completely dry. Simulation results showed that the permeability of the domain has reduced with 38%. However, the pressure drop did not increase, which indicates that the increase in relative permeability of CO_2 due to the increase in saturation did counteract the decrease in absolute permeability.

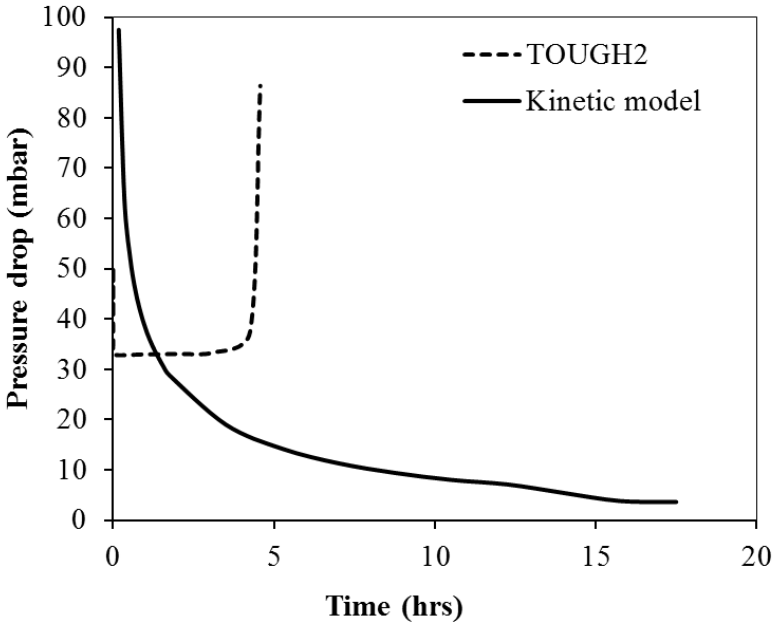

Figure 3.4. Pressure drop over the core during simulations. Complete impairment in injectivity was found in the TOUGH2 model after approximately 4 h of injection. In the kinetic model the pressure drop decreases over time, because the reduction in rock permeability is counteracted by the increase in CO_2 relative permeability.

3.5.2. Experimental results

The histograms of the images were used as a separation tool to distinguish between different phases. Materials have different ranges of X-ray absorption coefficients and show therefore separate peeks in the histograms. Unfortunately, attenuation coefficients for brine and solid salt were too similar to distinguish the different phases. Therefore, solid salt saturation could only be determined at the end of the experiment.

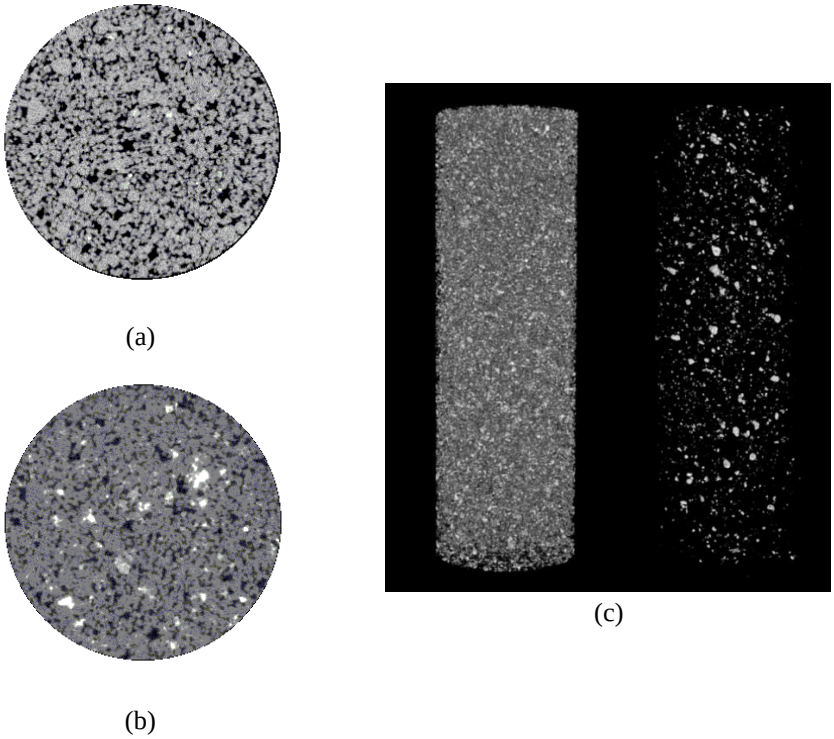

Figure 3.5. Slices of CT images (a) prior to and (b) post experiment and (c) 3D representation of dry core and precipitated salt. Precipitated salt is represented by the white color, gray represents the sandstone grains and gas is shown by the black color.

3.5.2.1. Visualization and quantification of salt precipitation

Figure 3.5 shows two slices obtained by µ-CT scanning (a) before and (b) after the dry-out experiment. The image quality allows for a clear distinction between gas, solid matrix and precipitated salt. Precipitated salt is clearly visible as bright spots in the pore space compared to the initially dry rock. Approximately 2000 slices were reconstructed along the core length resulting in a 3D image (Figure 3.5c). On the right-hand side only solid salt within the pore space is presented, while the initial rock is shown on the left. The location of formation of salt crystals is crucial to the connectivity of the flow path. We can observe salt formation in small and well as large pores and a uniform distribution throughout the core.

Figure 3.6 shows the final profile of precipitated salt along the core at the end of the experiment and is compared to the simulation with the kinetic model in the same panel. The experimental results for the solid salt fraction were obtained by taking the average over each slice. The simulation and experimental results are compatible for

most of the domain. Towards the inlet a discrepancy can be observed where the model predicts a higher solid salt fraction while experimental results show a slightly lower solid salt fraction. We believe this can be explained by an overestimation of the capillary end effect by the model as will be elaborated in the next section.

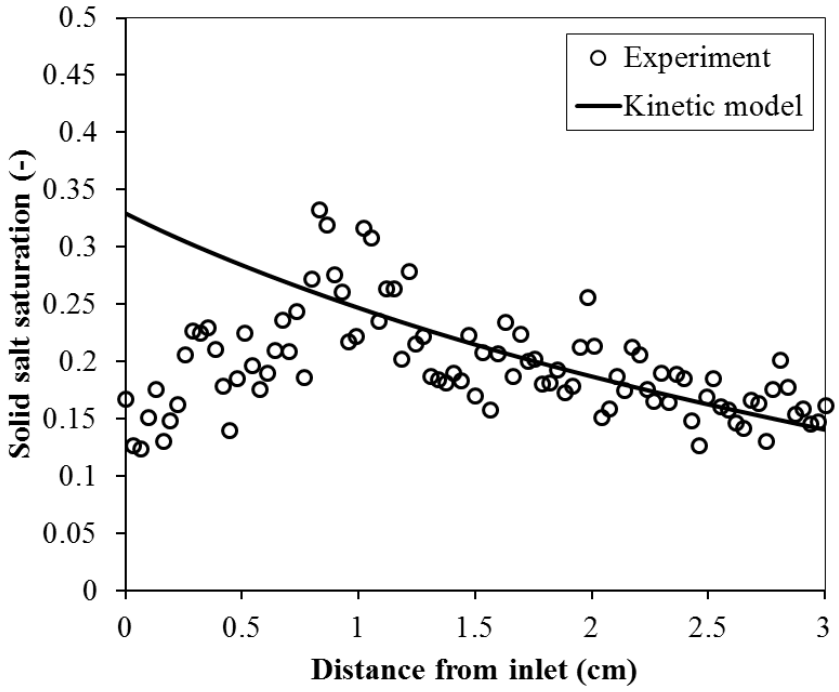

Figure 3.6. Salt precipitation profile along the core after dry-out. The kinetic model provides satisfying results for the salt profile along the core. A slight overestimation can be observed at the inlet.

3.5.2.2. Gas saturation profiles

Gas saturation profiles along the core were taken as slice-averaged values obtained from μ-CT scans. Figure 3.7 shows the gas saturation profiles at different time steps, starting at 25 minutes after CO_2 injection began. The low gas saturation at brine breakthrough shows that displacement was not very efficient which is in accordance with the high mobility contrast between CO_2 and brine. The core was considered to be dry after 17.5 hours because the gas saturation and salt saturation profiles summed up to unity. It appears that dry-out occurs at the whole length of the core as CO_2 saturation increases throughout the whole core simultaneously. The salt profiles indicate that capillary-driven backflow of brine was not significant, which makes evaporation the only drying mechanism present. A drying front moving from the

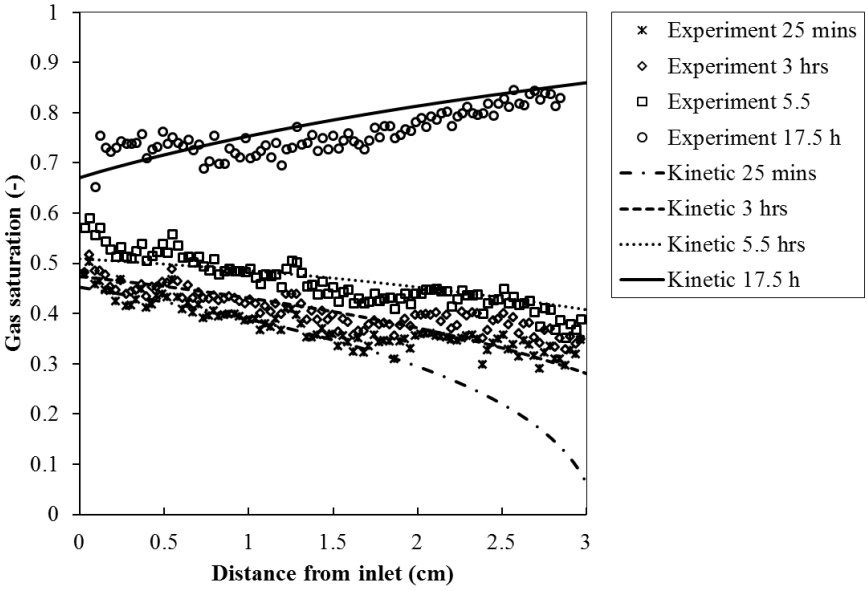

Figure 3.7. Gas saturation at multiple time steps obtained from CT scans and kinetic model. A good match was found between experimental and numerical data.

inlet towards the outlet cannot be observed, which indicates that the evaporation rate is significantly lower than the injection rate. This suggests that CO_2 does not become saturated with water and evaporation occurs along the whole core length.

The simulations can predict the progression of CO_2 saturation in the core over time very well. However, they overestimate the capillary end effect (t = 25 min). The experimental results show a rather uniform CO_2 distribution throughout the core whereas the model predicts a lower gas saturation towards the outlet. The discrepancy in solid salt fraction as pointed out in the previous section can be explained by the higher remaining brine saturation in the simulation combined with a mild capillary-driven backflow.

3.5.2.3. Pressure drop and permeability alteration

The experimental pressure drop over the core during dry-out is shown in Figure 3.8 by the solid line. At the given flow rate, breakthrough of CO_2 takes place within a few seconds, which is represented by the steep fall of the pressure drop in the short times. Then, a gradual decrease in pressure drop over time can be observed, which indicates a continuous increase of the effective permeability ($K \times k_{rg}$). Injectivity impairment was not found in the experiments. After approximately 30 minutes and after 8 hours of injection, we observe a steep fall in pressure drop in the experimental results.

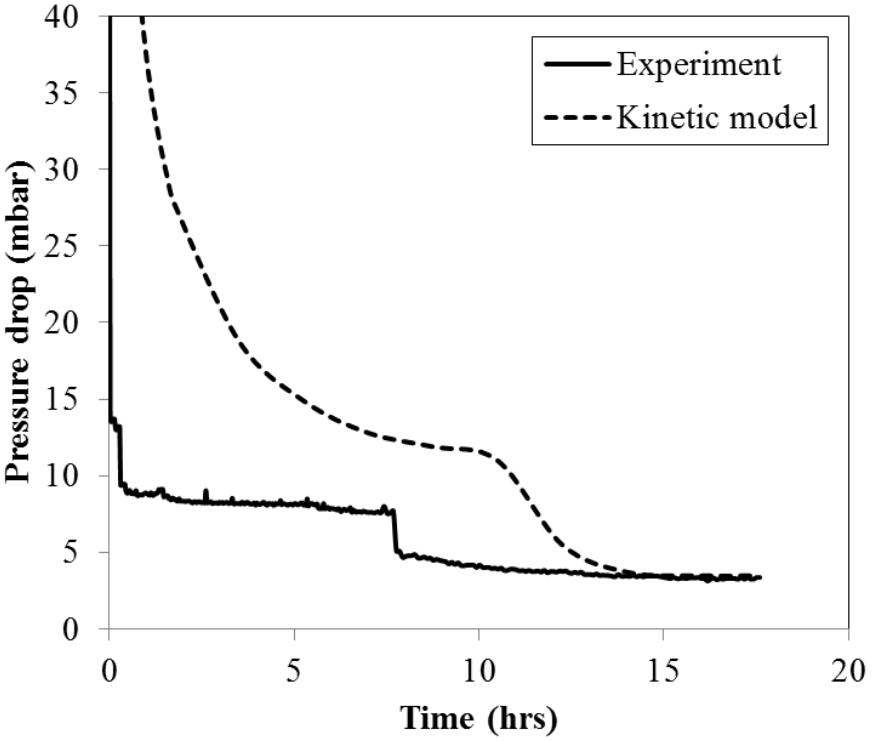

Figure 3.8. Pressure drop over the core for the kinetic model (dashed line), and the experimental results (solid line). The model can successfully predict the dry-out time and the trend of decreasing pressure drop. An exact match between the numerical and experimental results could not be obtained with the current relative permeability parameters.

The model can successfully predict the dry-out time and the trend of decreasing pressure drop, however, an exact match between the numerical and experimental results could not be obtained with the current relative permeability parameters. Also, adjustment of the parameters of the permeability-porosity relationship could not provide more satisfactory results. We believe that the use of oil as a non-wetting phase (instead of gas) in the relative permeability measurements, and the lack of experimental data below connate water saturation caused the difference between experimental and modeling results.

3.6. Conclusions

Dry-out and salt precipitation induced by CO_2 injection into sandstone cores saturated with brine have been visualized and quantified by µ-CT scanning technique. Attempt to match the salt precipitation profiles using TOUGH2/ECO2N (showing injectivity impairment) to the measured profiles (indicating absence of injectivity impairment) proved fruitless. Seemingly the assumption of a local equilibrium in the description of phase partitioning between CO_2 and brine leads to an erroneous prediction of clogging at the injection rates applied. TOUGH2/ECO2N numerical simulations showed an accumulation of salt near the core inlet consistently a capillary-driven backflow of brine. The permeability at the inlet of the modeling domain reduced to zero and injection was impaired.

By using a kinetic model for the CO_2 and brine phase partitioning the predicted profiles were more compatible with the measured ones. This strongly suggests that CO_2 did not become saturated with water and mass transfer occurred along the whole length of the core. Therefore the brine saturation gradient remained low and capillary-driven backflow did not have a significant impact on salt precipitation.

Regarding field conditions, we believe that one should be careful with applying local equilibrium assumption (LEA) to CO_2 injection modeling. Evaporation rates are orders of magnitude smaller than well injection velocities and LEA may not be valid. Numerical simulations may predict near well clogging by salt accumulation which may in reality take place much further away in the aquifer, where flow velocities are much lower.

Acknowledgments

This research was done as part of CATO-2, the Dutch National Program for CCS. The authors are grateful for the Dutch Ministry of Economic Affairs and the sponsoring companies for funding. We would like to thank Marc Friebel and Wim Verwaal, technical staff of our laboratory, for their help with conducting the experiments, and Dr. Cas Berentsen for useful discussions and comments. The authors would also like to thank Florian Doster, Eirik Keilegavlen and Jan Nordbotten for providing their book chapter with a detailed description of the ImPEM method.

Bibliography

André, L., Peysson, Y., Azaroual, M., 2013. Well injectivity during CO2 storage operations in deep saline aquifers – Part 2: Numerical simulations of drying, salt deposit mechanisms and role of capillary forces. International Journal of Greenhouse Gas Control.

Anton, L., Hilfer, R., 1999. Trapping and mobilization of residual fluid during capillary desaturation in porous media. Physical Review E 59, 6819-6823.

Bacci, G., Korre, A., Durucan, S., 2011. Experimental investigation into salt precipitation during CO2 injection in saline aquifers. Energy Procedia 4, 4450-4456.

Berg, S., Ott, H., 2012. Stability of CO2–brine immiscible displacement. International Journal of Greenhouse Gas Control 11, 188-203.

Dong, M., Dullien, F.A.L., 1997. A New Model for Immiscible Displacement in Porous Media. Transport in Porous Media 27, 185-204.

Doster, F., Keilegavlen, E., Nordbotten, J.M., 2014. Multi-Phase Multi-Component Flow Including Capillary Pressure And Buoyancy: A Robust Implicit Pressure Explicit Mass Finite Volume Method.

Fang, Y., Baojun, B., Dazhen, T., Dunn-Norman, S., Wronkiewicz, D., 2010. Characteristics of CO2 sequestration in saline aquifers. Pet. Sci. 7, 83-92.

Farkas, E., 1998. Linearization Techniques of Reservoir-Simulation Equations: Fully Implicit Cases. SPE Journal 3, 316-323.

Feldkamp, L., Davis, L., Kress, J., 1984. Practical cone-beam algorithm. JOSA A 1, 612-619.

Fuller, R.C., Prevost, J.H., Piri, M., 2006. Three-phase equilibrium and partitioning calculations for CO2 sequestration in saline aquifers. Journal of Geophysical Research: Solid Earth 111, B06207.

Giorgis, T., Carpita, M., Battistelli, A., 2007. 2D modeling of salt precipitation during the injection of dry CO2 in a depleted gas reservoir. Energy Conversion and Management 48, 1816-1826.

Hilfer, R., Øren, P., 1996. Dimensional analysis of pore scale and field scale immiscible displacement. Transport in Porous Media 22, 53-72.

Huang, D.D., Honarpour, M.M., 1998. Capillary end effects in coreflood calculations. Journal of Petroleum Science and Engineering 19, 103-117.

Lake, L.W., 1989. Enhanced oil recovery.

Lenormand, R., Touboul, E., Zarcone, C., 1988. Numerical models and experiments on immiscible displacements in porous media. Journal of Fluid Mechanics 189, 165-187.

Lorenz, S., Müller, W., 2003. Modelling of halite formation in natural gas storage aquifers, Proceedings, TOUGH Symposium 2003.

Metz, B., Davidson, O., Bosch, P., Dave, R., Meyer, L., 2007. IPCC, 2007: Climate Change 2007: Mitigation. Contribution of Working Group III to the Fourth Assessment Report of the Intergovernmental Panel on Climate Change. Cambridge University Press, Cambridge, United Kingdom and New York, NY, USA.

Muller, N., Qi, R., Mackie, E., Pruess, K., Blunt, M.J., 2009. CO2 injection impairment due to halite precipitation. Energy procedia 1, 3507-3514.

Nachshon, U., Weisbrod, N., Dragila, M.I., Grader, A., 2011. Combined evaporation and salt precipitation in homogeneous and heterogeneous porous media. Water Resources Research 47.

Ott, H., de Kloe, K., Marcelis, F., Makurat, A., 2011. Injection of supercritical CO2 in brine saturated sandstone: Pattern formation during salt precipitation. Energy Procedia 4, 4425-4432.

Ott, H., de Kloe, K., van Bakel, M., Vos, F., van Pelt, A., Legerstee, P., Bauer, A., Eide, K., van der Linden, A., Berg, S., 2012. Core-flood experiment for transport of reactive fluids in rocks. Review of Scientific Instruments 83, 084501.

Pape, H., Clauser, C., Iffland, J., 1999. Permeability prediction based on fractal pore-space geometry. Geophysics 64, 1447-1460.

Peysson, Y., 2012. Permeability alteration induced by drying of brines in porous media. The European Physical Journal Applied Physics 60, 24206.

Peysson, Y., Andre, L., Azaroual, M., 2014. Well injectivity during CO2 storage operations in deep saline aquifers—Part 1: Experimental investigation of drying effects, salt precipitation and capillary forces. international journal of Greenhouse Gas Control 22, 291-300.

Peysson, Y., André, L., Azaroual, M., 2013. Well injectivity during CO2 storage operations in deep saline aquifers—Part 1: Experimental investigation of drying effects, salt precipitation and capillary forces. International Journal of Greenhouse Gas Control.

PiPujol, M., Buurman, P., 1997. Dynamics of iron and calcium carbonate redistribution and palaeohydrology in middle Eocene alluvial paleosols of the southeast Ebro Basin margin (Catalonia, northeast Spain). Palaeogeography, Palaeoclimatology, Palaeoecology 134, 87-107.

Pruess, K., 2005. ECO2N: A TOUGH2 fluid property module for mixtures of water, NaCl, and CO2. Lawrence Berkeley National Laboratory Berkeley.

Pruess, K., Garcia, J., 2002. Multiphase flow dynamics during CO2 disposal into saline aquifers. Environmental Geology 42, 282-295.

Pruess, K., Müller, N., 2009. Formation dry-out from CO2 injection into saline aquifers: 1. Effects of solids precipitation and their mitigation. Water Resources Research 45, W03402.

Riaz, A., Tchelepi, H.A., 2004. Linear stability analysis of immiscible two-phase flow in porous media with capillary dispersion and density variation. Physics of Fluids 16, 4727.

Riaz, A., Tchelepi, H.A., 2006. Influence of relative permeability on the stability characteristics of immiscible flow in porous media. Transport in Porous Media 64, 315-338.

Scherer, G.W., 2004. Stress from crystallization of salt. Cement and Concrete Research 34, 1613-1624.

Spycher, N., Pruess, K., 2005. CO2-H2O mixtures in the geological sequestration of CO2. II. Partitioning in chloride brines at 12–100° C and up to 600 bar. Geochimica et Cosmochimica Acta 69, 3309-3320.

Tambach, T., Loeve, D., Hofstee, C., Plug, W.-J., Mass, J., 2014. Effect of CO2 Injection on Brine Flow and Salt Precipitation After Gas Field Production. Transport in Porous Media DOI 10.1007/s11242-014-0283-x.

Van Hemert, P., Rudolph, E.S.J., Zitha, P.L., 2013. Micro Computer Tomography Study of Potassium Iodide Precipitation in Bentheimer Sandstone Caused by Flow-through CO2 Drying. Energy Procedia 37, 3331-3346.

Verma, A., Pruess, K., 1988. Thermohydrological Conditions and Silica Redistribution Near High-Level Nuclear Wastes Emplaced in Saturated Geological Formations. J. Geophys. Res. 93, 1159-1173.

Wang, Y., Mackie, E., Rohan, J., Luce, T., Knabe, R., Appel, M., 2009. Experimental study on halite precipitation during CO 2 sequestration, International Symposium of the Society of Core Analysts held in Noordwijk, The Netherlands, pp. 27-30.

Wasch, L.J., Wollenweber, J., Tambach, T.J., 2013. Intentional salt clogging: a novel concept for long-term CO2 sealing. Greenhouse Gases: Science and Technology.

Zuluaga, E., Castrillon, J., Monsalve, J., Rendon, A., 2002. Experiments on Water Vaporisation in Porous Media, Canadian International Petroleum Conference. Petroleum Society of Canada.

4

Salt precipitation due to supercritical gas injection: capillary-driven flow in a porous medium

Abstract

Drying and salt precipitation in geological formations can have serious consequences for upstream operations in terms of injectivity and productivity. Here we investigate the consequences of supercritical CO_2 injection in sandstones. The reported findings are directly relevant for CO_2 sequestration and acid-gas injection operations, but might also be of interest to a broader community dealing with drying and capillary phenomena. By injecting dry supercritical CO_2 into brine-saturated sandstone, we investigate the drying process and the associated precipitation of salts in a capillary-pressure-dominated flow regime. Precipitation patterns were recorded during the drying process by means of μ-CT scanning. The experimental results and numerical simulations show that under a critical flow rate salt precipitates with an inhomogeneous spatial distribution because of brine and solutes being transported upstream in counter-current flow where salt eventually precipitates. A substantial impairment of the absolute permeability has been found, but despite high local salt accumulation, the effective CO_2 permeability increased during all experiments and impairment injectivity was not observed.

[Based on: H. Ott, S. M. Roels, K. de Kloe 2015. Salt precipitation due to supercritical gas injection: capillary-driven flow in unimodal sandstone. International Journal of Greenhouse Gas Control]

4.1. Introduction

Drying of porous media is an important topic in many industrial processes, in soil science and for upstream operations such as gas injection and production into and from geological formations. Drying of saline formations will cause precipitation of salt initially dissolved in the brine. This can negatively affect the performance of injection and production wells and can even lead to well clogging, which is a serious risk for such operations. In this paper we consider large-scale geological storage of CO_2, originating from anthropogenic sources like fossil fuelled power plants or contaminated gas production in order to reduce CO_2 emissions. Deep saline aquifers and depleted oil and gas fields are potential subsurface deposits for that purpose (Bachu and Gunter, 2004; Metz et al., 2005).

If dry or under-saturated, supercritical (SC) CO_2 is injected into water-bearing geological formations like saline aquifers, water is removed by either viscous displacement of the aqueous phase or by evaporation of water in CO_2 and subsequent advection in the injected CO_2-rich phase. These mechanisms act in parallel, but while advection of the aqueous phase decreases with increasing CO_2 saturation (diminished mobility), evaporation becomes increasingly important as the aqueous phase becomes immobile. Below residual water saturation, only evaporation takes place and the formation dries out if no additional source of water is available. In case of a brine source, capillary-driven backflow can induce flow from wetter to dryer regions, leading to an accumulation of salt in the dry zone. In highly saline formations, the amount of salt that potentially precipitates per unit volume can be quite substantial. The volumes depend on brine salinity, and the transport of solutes and water in the reservoir. Since fluid saturations and flow rates close to the well bore cover a large range as functions of space and time, there are no easy answers to the questions whether, where and how salt precipitates and how precipitation affects injectivity. The questions that need to be addressed are about the mechanisms of solute transport on a macroscopic scale that determine the macroscopic distribution of salt, and the salt distribution on a pore scale that determine how the permeability is affected as function of porosity reduction.

Even though salt precipitation in the vicinity of gas production wells are generally considered an issue, there are not many studies published referring to well data. The frequently cited paper is that of Kleinitz et al. (2001). The lack of well studies renders a proper problem statement difficult and we rely on numerical simulations and analytical models that are available in literature. Here, we only aim to highlight a few key studies on precipitation due to CO_2 injection relating to the problem discussed in this paper. In a series of publications, Pruess *et al.* presented numerical simulations of CO_2 injection in saline aquifers investigating the fundamental aspects of formation dry-out and salt precipitation (Muller et al., 2009; Pruess and Garcia,

2002). The simulations were performed with a single injection well in idealized 1D and 2D radial geometries. The authors observed that precipitation occurs only in a narrow dry-out zone confined to a few meters around the injection well. The solid salt saturation in this zone has been found to be independent of the injection rate. 2D radial simulations were carried out to explore gravity effects. In contrast to the 1D radial scenario, gravity in combination with capillary-driven flow lead to more heterogeneous precipitation with a maximum observed solid-salt saturation of more than 20%.

Giorgis et al. (2007) performed field-scale simulations in radial geometry. The authors found that the amount of precipitate around the wellbore depends on brine mobility and can be high if there is a capillary-driven backflow of brine. The authors have further shown that the injection rate is an important factor in controlling precipitation process and in avoiding or allowing complete clogging of the formation. In their simulations, solid salt saturations of locally more than 60% have been reached.

However, field scale simulations require input on flow physics and thermodynamics such as the $K(\phi)$ relationship and the mass transfer rates between phases. The quality of the input is critical for reliable simulations as several studies suggest that a modest change in porosity might lead to a serious reduction in permeability. The discussed mechanisms range from the porosity variation due to lithology/rock type (Ehrenberg and Nadeau, 2005; Pape et al., 1999) via mechanical compaction (Schutjens et al., 2004; Wyble, 1958) to silica dissolution and precipitation in geothermal systems in single phase flow (Xu et al., 2004b) to drying processes, i.e. in two-phase flow (Bacci et al., 2011), and this study. Even if usually described by power laws it cannot be expected that the $K(\phi)$ relationships resulting from different mechanisms are comparable – i.e. process independent – and generally applicable.

There are only a few studies on flow-through drying available, which are relevant for CO_2 storage. Zuluaga *et al*. investigated vaporization and salt precipitation in sand packs and sandstone for gas production wells (Zuluaga and Monsalve, 2003; Zuluaga et al., 2001). Recently, two experimental studies on dry CO_2 injection have been reported (Ott et al., 2011; Ott et al., 2010). The experiments have been performed in sandstone in realistic storage conditions addressing capillary-driven solute transport, the condition of counter current flow (Ott et al., 2011), and a permeability porosity relationship (Bacci et al., 2011). Recently, Peysson et al. (2014) and André et al. (2014) investigated the drying process by nitrogen injection in sandstone. The data have been used to benchmark a numerical simulation tool for field-scale modeling of CO_2 injection. Ott et al. (2011) pointed out that modeling of vaporization by an equilibrium approach is not sufficient to describe core flood experiments. Roels et al. (2014) performed core flood experiments and succeeded in the description of the saturation profiles by a kinetic approach.

This paper revisits results of CO_2 injection core-flood experiments reported earlier (Ott et al., 2011; Ott et al., 2010) to perform a more detailed analysis. The experiments were performed to investigate the drying process and the impact of salt precipitation on flow, i.e. the salt distribution inside the porous medium. The experiments were carried out at flow rates realistic for near-well-bore flow and at realistic thermodynamic conditions. During injection, spatial and time evolution of saturation changes were monitored by means of micro computed tomography (μ-CT). The results in this paper are based on a number of experiments showing precipitation profiles with different degrees of heterogeneity on a macroscopic scale. For quantification we discuss two of these experiments showing the largest and the smallest spatial variation of salt saturation after dry-out. In addition to the saturation profiles, changes in absolute permeability and effective CO_2 permeability were monitored. We explain the observed mild permeability reduction by the microscopic distribution of the salt with respect to the observed CO_2 flow channels.

4.2. Materials and methods

4.2.1. Experimental set-up and procedure

The experiments were carried out in a core-flood setup designed for flooding with volatile and reactive fluids (Figure 4.1). A detailed description of the unit can be found elsewhere (Ott et al., 2012). In the following, only a brief description of the elements will be given that are of relevance for the experiments here presented.

The flow experiments were performed in vertical geometry, with fluids being injected from top to bottom. The samples were embedded in polycarbonate and placed in a carbon-fiber based core holder – both materials have low X-ray attenuation coefficients. The core holder is placed in a μ-CT scanner for in-situ 3D imaging of the rock-fluid system. CT imaging allows to determine fluid saturations and changes of the rock matrix due to salt precipitation. The unit is equipped with two feed section for liquids and liquefied gas injection. The CO_2 feed pump was held at 3°C during the experiments – liquid CO_2 was injected and heated to experimental temperature and to the respective SC state in the injection lines. The density difference has been taken into account for the indicated flow rates. From flow rates and the differential pressure measurement, ΔP, the absolute, K, and effective permeability, $K \times k_r$, were derived on line.

The experiments were performed on Berea sandstone with an average permeability of 500 mD and 22% porosity. The samples were drilled from the same block and were small in cross section and volume (1.0 ± 0.1 cm diameter and 5.0 ± 0.1 cm length) to obtain representative flow rates and to reduce the experimental time to complete dry-out. The mineralogy of Berea is dominated by quartz with some K-

feldspar, kaolinite, and minor amounts of other clay minerals as determined by eSEM/EDX. The rock samples were pre-saturated with NaCl based high-salinity brine: 20 wt% NaCl and 2 wt% CsCl. The CsCl was added as a contrast agent as the X-ray absorption coefficient is high, leading to a high X-ray absorption contrast in μ-CT between the aqueous and the CO_2 rich phase.

For each experiment a dry and clean rock sample was placed in the core holder and subsequently pressurized and heated under N_2 flow to 45(±1)°C/100 bar (downstream side), corresponding to the thermodynamic conditions of a saline aquifer at a depth of about 1000 m. To quantitatively determine saturations, reference scans at 100% CO_2 saturation and 100% brine saturation were recorded. For that purpose, nitrogen was displaced by SC CO_2 (miscible displacement) until 100% CO_2 saturation was reached as checked by the density of the produced fluid. Subsequently, the core was slowly depressurized and evacuated to allow brine saturation without trapping CO_2. The core was then saturated with brine and subsequently pressurized. All the reference scans were taken at experimental temperature and pressure. During the experiments, dry SC CO_2 was injected at a constant rate into the brine-saturated core. The injection rates at experimental conditions were 2.2 mL/min and 4.4 mL/min, corresponding to realistic near-wellbore flow rates.

Under the experimental conditions in this work (45°C and 100 bar) CO_2 solubility in brine is substantial (Spycher and Pruess, 2005). The pH of the brine solution decreases significantly with increasing CO_2 concentration, which may lead to dissolution of clays (Lagneau et al., 2005; Shao et al., 2010). However, since the amount of clays detected by eSEM/EDX is very minor, we neglect the effects of dissolution of CO_2 on porosity and permeability alterations.

4.2.2. CT scanning

We observe the spatial distribution of precipitated salt by means of μ-CT imaging. Computer tomography is based on X-ray absorption determined by material-specific linear attenuation coefficients (μ), which are directly represented as gray values of the voxels in the reconstructed image (Vinegar and Wellington, 1987; Wellington and Vinegar, 1987). For saturation calculations we made use of tabulated mass-absorption coefficients μ/ρ (Hubbell, 1969), fluid densities ρ (Pruess and Spycher, 2007; Span and Wagner, 1996), and the density of solid salt (Lide, 2003). μ/ρ for the injected and produced fluids and their constituents are shown in Figure 4.2 and phase densities are listed in Table 4.1. Because of the sensitivity of saturation calculations to the X-ray contrast agent, we measured relative absorption coefficients of CsCl solutions as a function of CsCl concentration. The curve is shown in the lower panel of Figure 4.2; at 2 wt% CsCl, the mass-absorption coefficient is about 1.6 times larger than that of pure water. The CsCl calibration curve was also used to determine the effective photon energy of the μCT photon

source (hv=63 keV) in order to derive the mass absorption coefficients used for the saturation calculations. The derived effective mass absorption coefficients are listed in Table 4.1.

Due to the higher solubility limit of CsCl, we expect that salt precipitates in a ratio different from the initial ratio mNaCl/mCsCl =10, because CsCl might stay longer in solution and might be preferentially removed by the displacement process. To estimate CsCl depletion, we performed simulations (not shown) with the experimental brine composition. The simulations were performed using ToughReact (Xu et al., 2004a) as simulation tool. NaCl and CsCl precipitation was handled in equilibrium using the ToughReact data base for NaCl and the CsCl solubility data reported in Lide (2003). The simulations result in mNaCl/mCsCl =12.3 and a respectively corrected scaling factor for saturation conversion according to Eq.(18).

Table 4.1. Densities at 100 bar and 45°C and mass-attenuation coefficients for converting saturation profiles according to Equation 2; * = dry, ** = water saturated, † = with, and †† = without CsCl, ‡ = in the presence of CO_2 ‡‡ = before CO_2-breakthrough. §: the deviation from the literature value can be explained by a ≈2K lower temperature in the external density meter.

	ρ_{CO2}	ρ_{brine}	ρ_{salt}
Measured	$585^{**} \rightarrow 565^{*,\S}$	$1140^{\dagger,\ddagger\ddagger}$ (±2)	-
Literature	499^{*}, $517^{*,**}$ (Spycher and Pruess, 2005)	$1140^{\dagger\dagger}$, $1172^{\dagger\dagger,\ddagger}$ (Spycher and Pruess, 2005)	2170 (NaCl), 3988 (CsCl), (Lide, 2003)
Used for saturation conversion	500	1140	2264 (m_{NaCl}/m_{CsCl}=10) 2247(m_{NaCl}/m_{CsCl}=12.3)

	$(\mu/\rho)_{CO2}$ [cm^2/g]	$(\mu/\rho)_{brine}$ [cm^2/g]	$(\mu/\rho)_{salt}$ [cm^2/g]
Used for saturation conversion	0.185	0.33	0.85 (m_{NaCl}/m_{CsCl}=10) 0.75 (m_{NaCl}/m_{CsCl}=12.3)

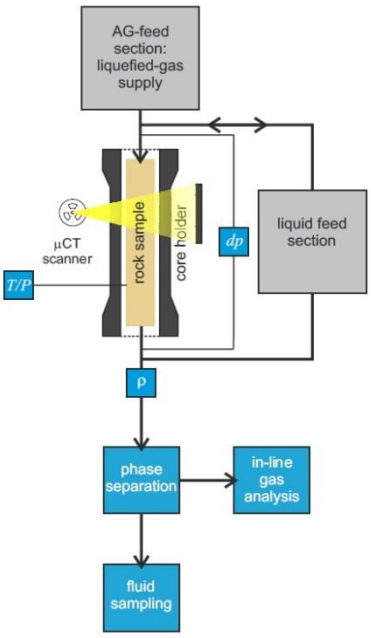

Figure 4.1. Schematic of the experimental set-up. More details are provided in Ott et al. (2012).

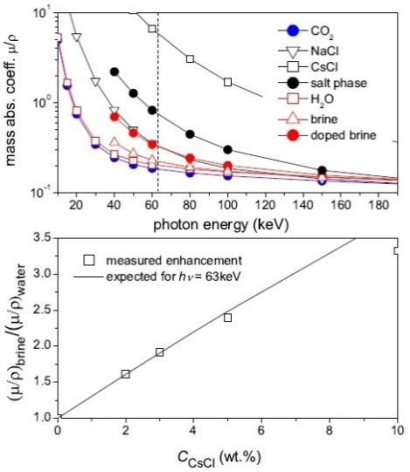

Figure 4.2. Top: X-ray mass absorption coefficients of the relevant fluids and salts as a function of photon energy. The vertical line indicates the calibrated effective photon energy that has been used to calculate the salt saturation by Eq. (18). Bottom: Relative absorption coefficients of the brine phase as a function of CsCl concentration. The data has been used to determine the effective photon energy *hν*=63 keV.

4.2.3. Numerical simulations

Numerical simulations were performed with the model presented in section 3.3.1., with the kinetic rate formulation as described in section 3.3.3. Simulation parameters were adjusted to account for a pressure of 100 bar and temperature of 45°C, and the use of a Berea sandstone. Capillary pressure and relative permeability parameters were obtained from Berg et al. (2013). In this simulations, relative permeability curves were described with a simplified version of the Corey model (Brooks and Corey, 1964):

$$k_{rw} = k_{rw}^{0} S_{we}^{\lambda_w}$$
$$k_{rg} = k_{rg}^{0}(1 - S_{we})^{\lambda_g} \quad (16)$$

where λ_w and λ_g are the fitting parameters for brine and CO_2 relative permeability, respectively. The simulation parameters used for Berea can be found in Table 4.2.

Table 4.2. Simulation parameters according to Berea sandstone and fluid properties at 100 bar and 45°C

Parameter	*Value*	*Unit*
k_{rw}^{0}	1	-
k_{rg}^{0}	0.5	-
λ_w	2.5	-
λ_g	3.7	-
P_d – *Van Genuchten*	6.0×10^4	Pa
m – Van Genuchten	0.9	-
Γ – *Verma and Pruess*	0.95	-
φ_r – *Verma and Pruess*	0.5	-
S_{wc}	0.15	-
K	0.5×10^{-12}	m^2
φ	0.22	-
L	0.05	m
Mass transfer rate coefficient	0.05	s^{-1}

4.3. Experimental results

4.3.1. Solid salt profile

Figure 4.3 shows the integrated µ-CT response profiles along the flow direction at different experimental time steps for the injection rate of 2.2 mL/min. The profiles are already converted to saturations by eliminating the rock matrix by subtracting the image from the fully brine-saturated scan. During the first 40 min brine and CO_2 were produced and, in the following period, only a CO_2-rich phase with no further liquid brine production. At that point, substantial drying by evaporation started. The

CO_2 saturation is represented with a scale ranging from 100% brine saturation (S_{CO2} = 0) to 100% CO_2 saturation (S_{CO2} = 1). The saturations have been calculated from integrated CT profiles $I(t)$ by:

$$S_{CO_2} = \frac{I_{brine} - I(t)}{I_{brine} - I_{CO_2}} \tag{17}$$

where I_{brine} and I_{CO2} represent the density profiles of the reference scans at 100% brine and 100% CO_2 saturation, respectively. The first CT scan was made after 0.4 h of CO_2 flooding. The saturation profile is flat, with an average CO_2 saturation of about 0.5 (blue line). The displacement was still advection dominated, with a high remaining brine saturation due to the unfavorable mobility ratio between CO_2 and brine. Salt precipitation due to evaporation can be ignored and so the system was in a two-phase regime (CO_2-brine). Subsequently the X-ray absorption decreases with time, in line with an increase in CO_2 saturation. If salt did not precipitate, flat density profiles would be expected, determined by the advection and water evaporation. However, while the lightest component in this experiment (CO_2) was injected, a dip occurred at about 2.5 mm from the core inlet, corresponding to a density increase - salt precipitates! The dip grew for about 9.5 h. After 10 h. (red line) the shape of the profile, including all features, did not change further for another 6 h of CO_2 flooding. This is a clear indication that the sample is dry – no water evaporates and no salt is precipitating anymore. We assume that at that point in time, the rock sample contained solid salt and CO_2 which, again, is a two-phase system. This allows the CT response for the red profile (dry state) to be rescaled to solid salt saturation by:

$$S_{salt} = \left(1 - S_{CO_2}\right) \frac{\mu_{brine} - \mu_{CO_2}}{\mu_{salt} - \mu_{CO_2}} \tag{18}$$

where μ denotes the respective attenuation coefficients, derived from the mass-attenuation coefficients (μ/ρ) and the respective phase densities ρ, listed in Table 4.1, by $\mu = (\mu/\rho)\rho$.

The mean value of potential solid-salt saturation was determined as 4.1±0.2%, in case salt precipitates inside an immobile brine phase. However, locally the solid salt saturation is as high as 18%, resulting from a redistribution of brine during dry-out near the inlet. The mean value of 4.1% corresponds to evaporation of 41±2% of the total water. From this, the average degree of water saturation in the produced CO_2 has been estimated to be about 35±2% using the saturation limit of water in CO_2 (≈ 0.00145 wt.%, (Pruess and Spycher, 2007; Span and Wagner, 1996), the injection rate and the experimental time to dry-out. From this we estimate the characteristic

length scale for the evaporation to be in the order of 0.3 to 1.0 m, which evidently is controlled by evaporation kinetics and the flow rate of the CO_2-rich phase.
The observed salt accumulation, which is locally much higher than the salt originally present in the brine in the same respective volume, is explained by a capillary driven counter-current flow as discussed further in the next section. However, using a flow rate of 4.4 mL/min resulted in a uniform salt precipitation profile. The precipitation profiles are shown in Figure 4.4 for both injection rates. The Péclet number, calculated with Eq.(15) is much larger than unity, i.e. Pe>>1. This indicates that the flat salt profile was not caused by diffusion of salt away from the drying front. The results suggest that at low injection rates, evaporation is fast compared to the flow velocity and a steep brine gradient is established inside the porous medium, leading to capillary-driven backflow. At high injection rates, salt precipitates homogeneously, as water evaporation takes place along the whole domain and capillary-driven backflow does not occur. Note that we did not observe a well-defined critical flow rate, which is a result of the variations of capillary properties from one sample to another. What we can state at this point is that the critical velocity, above which a flat salt profile can be expected, for the given rock type and thermodynamic conditions is in the range of the flow rates reported here.

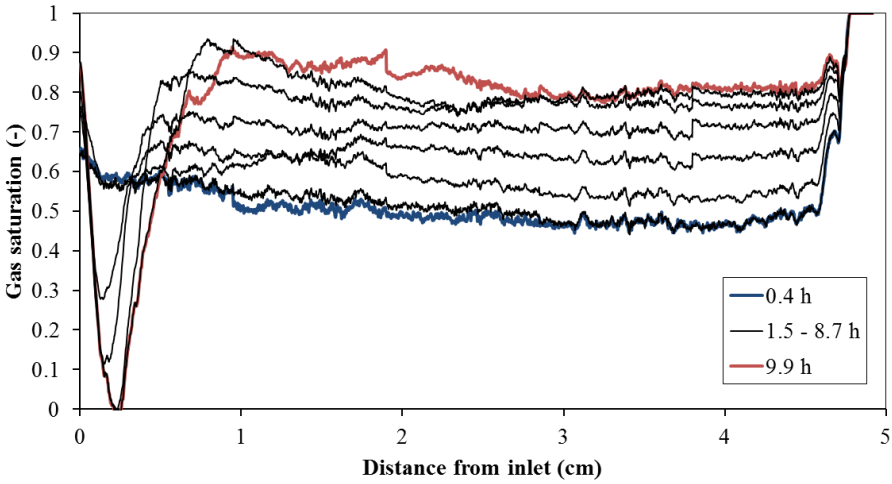

Figure 4.3. μ-CT data recorded during the experiment. Time series of normalized difference images projected onto the vertical sample axis in flow direction. The profiles represent changes of a three-phase system during injection of CO_2 with 2.2 mL/min: brine/CO_2/salt.

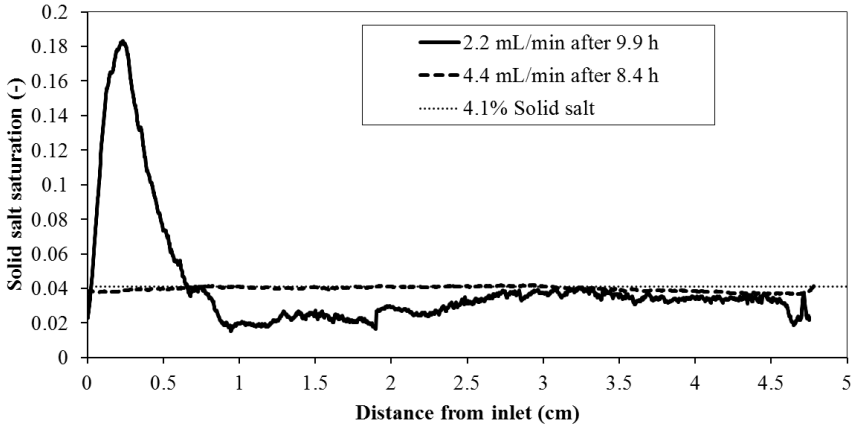

Figure 4.4 Solid salt profiles at the end of the experiments with salt accumulation near the inlet for 2.2 mL/min and a flat salt profile for 4.4 mL/min. The dotted line of 4.1% solid salt indicates the calculated salt saturation expected from the remaining brine saturation.

4.3.2. Effects on permeability

Of great interest is the effect of salt precipitation, i.e. porosity reduction, on permeability and eventually on injectivity. We measured porosity reduction by μ-CT and changes of permeability are reflected in the pressure drop. Figure 4.5 shows the pressure drop over the core length during flooding. The black line represents the data for injection with 2.2 mL/min showing a decrease in pressure drop with an initial differential pressure of about 600 mbar to a lower final value of 460 mbar. The onset of capillary back flow is visible as a small dip with a subsequent pressure drop increase due to substantial local precipitation. The pressure drop curve of the comparable experiment that showed a homogeneous precipitation pattern is shown in the same plot (red line). The pressure drop decreases significantly from about 600 mbar to 200 mbar at the end of the experiment.

The pressure drop does not decrease as dramatically in the low velocity injection experiment as in the high velocity injection experiment, but salt accumulation was not severe enough to cause impairment in injectivity. Despite the porosity reduction, the effective permeability of the CO_2-rich phase increased during the experiment, which means that relative permeability effects compensate for the absolute permeability reduction. A schematic illustration on the dry-out and precipitation process is shown in Figure 4.6. When salt precipitates in the location that was formerly occupied by the brine phase, reduction in permeability will not be observed. Instead, retraction of the brine phase (menisci) due to evaporation leads to an increase of CO_2 relative permeability.

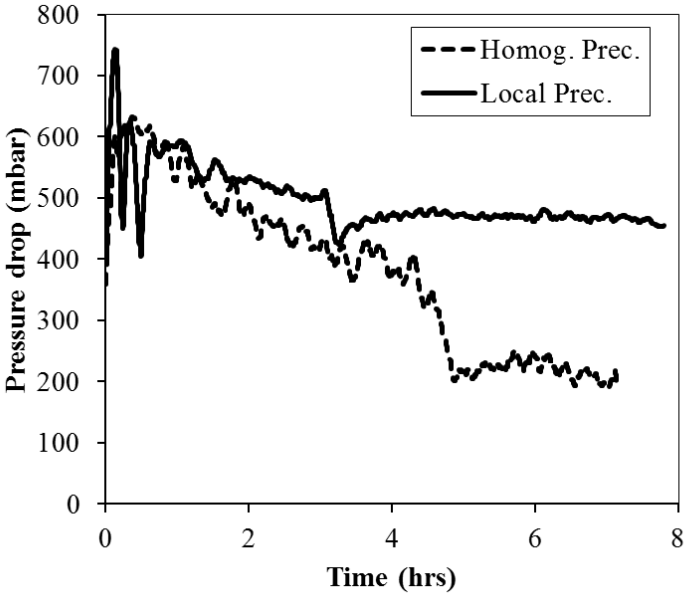

Figure 4.5. Pressure drop ΔP over the core during CO_2 injection. Two cases are shown: (1) the local precipitation case as discussed in the text (black line), and (2) ΔP recorded during homogeneous precipitation for comparison (red line).

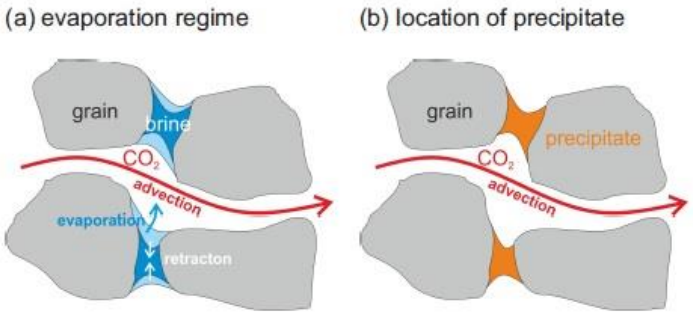

Figure 4.6. Schematic view on the dry-out and precipitation process. (a) Retraction of the brine phase (menisci) due to evaporation leading to an increase of CO_2 relative permeability. (b) The precipitate is essentially located in the volume formerly occupied by the brine phase.

4.4. Numerical simulations results

Numerical simulations were performed with the code accounting for kinetic phase partitioning between water and CO_2 (Roels et al., 2014). The following sections present the effect of injection velocity on the salt precipitation pattern, followed by an estimation of the zone of attraction for different injection velocities.

4.4.1. Effect of injection velocity on solid salt profile

The CO_2 injection process was simulated for the two different injection velocities, using the parameters listed in Table 4.2. The left graph in Figure 4.7 shows the precipitated salt profiles for 2.2 mL/min (solid line) and 4.4. mL/min (dashed line) at the end of the dry-out simulation. Accumulation of salt near the inlet was found for the lower injection velocity whereas for the higher injection velocity a flat salt profile was predicted. The simulations are therefore in good qualitative agreement with the experiments. However, to obtain this result an evaporation rate had to be applied such that a sufficient saturation gradient for capillary-driven backflow was established. Therefore, the numerical dry-out times are an order of magnitude larger than the experimental dry-out times. Similar observations can be made for the pressure drop simulations (Figure 4.7, right). The pressure drop decreases over time, supporting the idea that the increase in relative permeability for CO_2 is larger than the decrease in the matrix permeability. This is again in good qualitative with the experiments. The results indicate that the complexity of the evaporation process cannot be captured by the constant evaporation rate as applied in our model. A more accurate formulation of the dependence of evaporation on, e.g. interfacial area and injection velocity, should be developed in future studies.

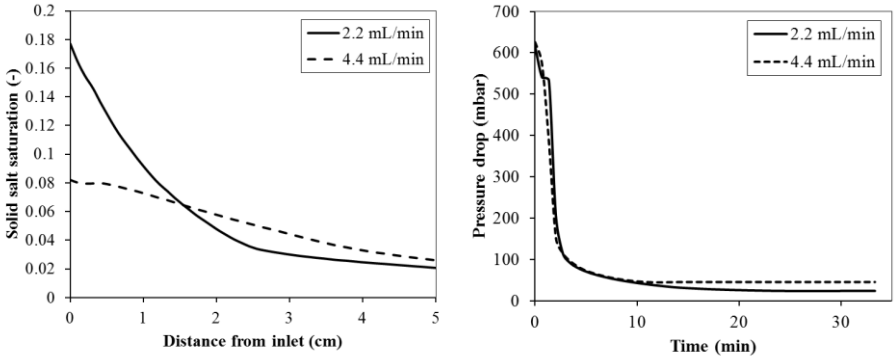

Figure 4.7. Left: solid salt saturation inside the domain after dry-out for two different injection velocities. Salt accumulation near the inlet is found for the low injection velocity. Right: pressure drop over the domain during the simulation. Impairment in injectivity does not occur.

4.4.2. The zone of attraction

Because of the finite contact area between the injected CO_2 stream and the brine in the rock and the finite evaporation rate, the solubility limit of water vapor in CO_2 is not reached instantly. As a result, water evaporates over a certain length until the solubility limit of water vapor in CO_2 is reached.

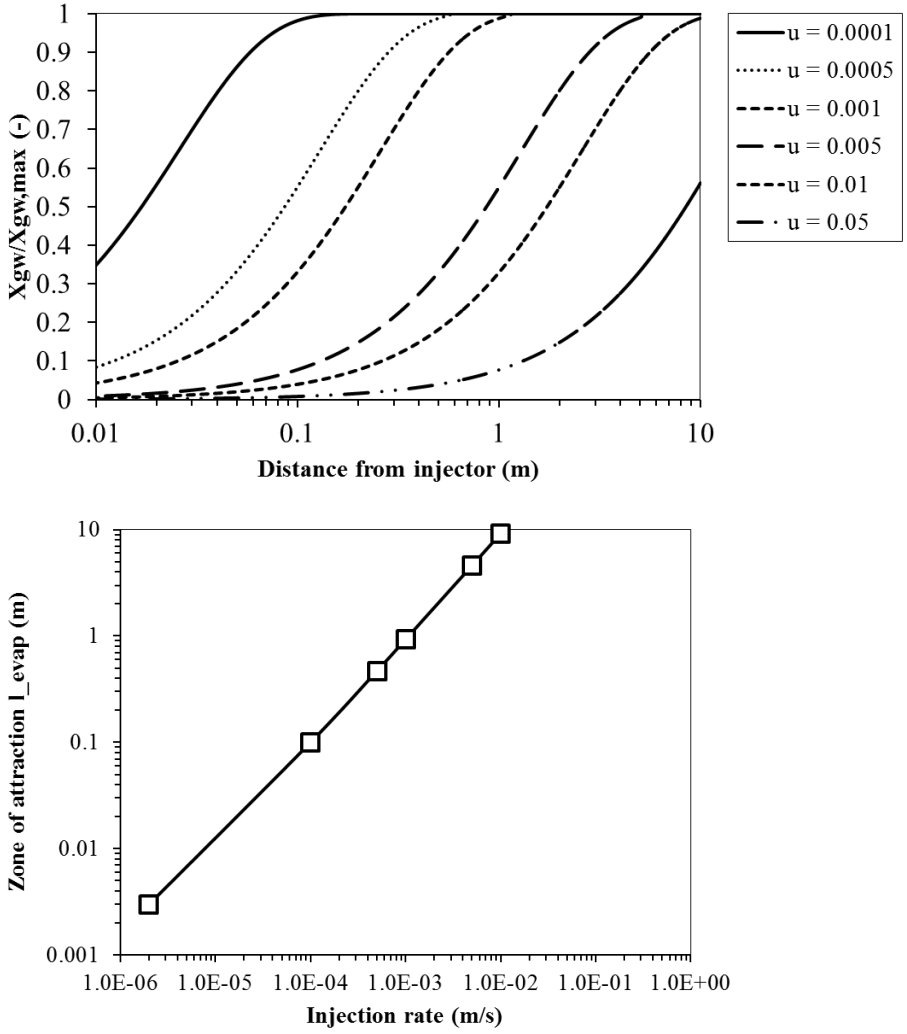

Figure 4.8: Zone of potential attraction. Upper panel: Water saturation in the CO_2-rich phase as function of distance from the injection point. The profiles for different injection rates are shown simulated in a linear flow geometry. Lower panel: The zone of attraction as a function of injection rate.

Over such a length, the water saturation gradient $\partial S_w/\partial x$ changes from the value corresponding to purely convective flow to values corresponding to capillary-dominated flow. In the latter case backflow of brine can occur. The zone of attraction is defined as the zone over which counter current solute transport can potentially occur. In this section we present an estimation of the zone dimension in linear geometry by numerical simulations. We model the zone of attraction for different injection rates between 0.01 and 100 ml/min/cm^2 (2×10^{-6} and 0.1 m/s). Simulations were performed with experimental input data on a semi-infinite simulation domain. Figure 4.8 shows the water content (molar fraction X_{gw} scaled to the solubility limit $X_{gw,max}$) profiles in the CO_2 stream for various injection rates. For all velocities, the ratio $X_{gw}/X_{gw,max}$ increases from 0.0 to 1.0 over a certain distance l_{evap} from the injector. The zone between the injector and l_{evap} is called zone of attraction. As shown in the lower panel of Figure 4.8, the length l_{evap} of the zone of attraction increases linearly from 3×10^{-3} to above 10 m as the velocity increases from 2×10^{-6} to 0.01 m/s. The presented kinetic simulations give valuable information about the size of the zone affected by salt precipitation and the distances over which solutes can be transported counter current in direction of the injector. This served the reservoir engineer as input for e.g. gridding of reservoir models around gas injectors and producers. The salt volume that potentially can be transported to the point of dry out can be estimated from the immobile brine fraction in the respectively affected volume.

4.5. Conclusions

We have investigated consequences of dry-out and salt precipitation in sandstone cores at flow regimes encountered in the vicinity of gas injection wells. In core flood experiments we injected dry SC CO_2 into brine-saturated sandstone samples and reached complete dry-out. During the floods we measured effective permeability and fluid and salt saturations.

We found that time scales of viscous displacement and drying are well separated. Two mechanisms turned out to be of importance: (1) macroscopic solute transport due to capillary pressure gradients, which determines the macroscopic salt distribution, and (2) the pore-scale arrangement of fluid phases during viscous displacement and the drying process. Such local effects determine effective permeability, the porosity-permeability relationship and probably the maximum possible saturation of salt in the pore space.

The principal mechanism of solute transport and the condition under which local precipitation occurs have been investigated by experiments and numerical

simulations. We identified the existence of a critical flow rate above which salt precipitates homogeneously on a macroscopic scale. Below the critical flow rate, capillary-induced back flow of the remaining brine phase transports solutes in the direction of the injection point, where salt eventually precipitates. We further showed the length scales over which solutes can potentially be transported as a function of injection rate. The zone of attraction can reach several meters depending on the flow rate and can exceed laboratory sample lengths. Due to counter current flow, the amount of precipitate per unit volume can exceed the volume of salt originally dissolved in the brine in the respective volume.

From pressure drop measurements during the presented experiments we evaluated the effect of porosity reduction on injectivity. Despite the observed strong reductions of absolute permeability, the effective CO_2 permeability increased during the experiment in all cases. This relatively mild impact of precipitation on the sample permeability can be attributed to the observed local precipitation pattern; salt precipitates in the brine phase and hence in the vicinity of CO_2-conducting channels, leaving these channels essentially open.

The results of the study are of direct relevance for the risk assessment of injection operations, and are of practical use for injectivity modeling. For the prediction of macroscopic salt transport and the resulting porosity reductions, injection rates and effective evaporation rates need to be taken into account. The dimension of the affected zone has been estimated to be in the order of several centimeters to meters, which is valuable input for an adequate gridding around gas injectors and producers in reservoir modeling.

Acknowledgments

The authors thank Steffen Berg and Jeroen Snippe for fruitful discussions and for reviewing the manuscript. Fons Marcelis is acknowledged for sample characterization and preparation and Pacelli Zitha for continuous support and discussions.

Bibliography

André, L., Peysson, Y., Azaroual, M., 2014. Well injectivity during CO2 storage operations in deep saline aquifers–Part 2: Numerical simulations of drying, salt deposit mechanisms and role of capillary forces. International Journal of Greenhouse Gas Control 22, 301-312.

Bacci, G., Korre, A., Durucan, S., 2011. Experimental investigation into salt precipitation during CO2 injection in saline aquifers. Energy Procedia 4, 4450-4456.

Bachu, S., Gunter, W.D., 2004. Overview of acid gas injection operations in western Canada, Proceedings of the 7th international conference on greenhouse gas control technologies, pp. 5-9.

Berg, S., Oedai, S., Ott, H., 2013. Displacement and mass transfer between saturated and unsaturated CO2–brine systems in sandstone. International Journal of Greenhouse Gas Control 12, 478-492.

Brooks, R., Corey, T., 1964. Hydraulic Properties of Porous Media.

Ehrenberg, S., Nadeau, P., 2005. Sandstone vs. carbonate petroleum reservoirs: A global perspective on porosity-depth and porosity-permeability relationships. AAPG bulletin 89, 435-445.

Giorgis, T., Carpita, M., Battistelli, A., 2007. 2D modeling of salt precipitation during the injection of dry CO2 in a depleted gas reservoir. Energy Conversion and Management 48, 1816-1826.

Hubbell, J.H., 1969. Photon cross sections, attenuation coefficients, and energy absorption coefficients from 10 keV to 100 GeV. DTIC Document.

Kleinitz, W., Koehler, M., Dietzsch, G., 2001. The precipitation of salt in gas producing wells, SPE European formation damage conference. Society of Petroleum Engineers.

Lagneau, V., Pipart, A., Catalette, H., 2005. Reactive Transportmodelling and Long Term Behaviour of CO2 Sequestration in Saline Aquifers. Oil & gas science and technology 60, 231-247.

Lide, D., 2003. CRC Handbook of Chemistry and Physics C R C Press LLC. Boca R aton FL.

Metz, B., Davidson, O., De Coninck, H., Loos, M., Meyer, L., 2005. IPCC, 2005: IPCC special report on carbon dioxide capture and storage. Prepared by Working

Group III of the Intergovernmental Panel on Climate Change. Cambridge, United Kingdom and New York, NY, USA, 442 pp.

Muller, N., Qi, R., Mackie, E., Pruess, K., Blunt, M.J., 2009. CO2 injection impairment due to halite precipitation. Energy procedia 1, 3507-3514.

Ott, H., de Kloe, K., Marcelis, F., Makurat, A., 2011. Injection of supercritical CO2 in brine saturated sandstone: Pattern formation during salt precipitation. Energy Procedia 4, 4425-4432.

Ott, H., de Kloe, K., Taberner, C., Marcelis, F., Wang, Y., Makurat, A., 2010. Rock/Fluid Interaction by Injection of Supercritical CO2/H2S: Investigation of Dry-zone Formation Near the Injection Well, International Symposium of the Society of Core Analysts, Halifax, Nova Scotia, Canada.

Ott, H., de Kloe, K., van Bakel, M., Vos, F., van Pelt, A., Legerstee, P., Bauer, A., Eide, K., van der Linden, A., Berg, S., 2012. Core-flood experiment for transport of reactive fluids in rocks. Review of Scientific Instruments 83, 084501.

Pape, H., Clauser, C., Iffland, J., 1999. Permeability prediction based on fractal pore-space geometry. Geophysics 64, 1447-1460.

Peysson, Y., Andre, L., Azaroual, M., 2014. Well injectivity during CO2 storage operations in deep saline aquifers—Part 1: Experimental investigation of drying effects, salt precipitation and capillary forces. international journal of Greenhouse Gas Control 22, 291-300.

Pruess, K., Garcia, J., 2002. Multiphase flow dynamics during CO2 disposal into saline aquifers. Environmental Geology 42, 282-295.

Pruess, K., Spycher, N., 2007. ECO2N–A fluid property module for the TOUGH2 code for studies of CO2 storage in saline aquifers. Energy Conversion and Management 48, 1761-1767.

Roels, S.M., Ott, H., Zitha, P.L., 2014. μ-CT analysis and numerical simulation of drying effects of CO2 injection into brine-saturated porous media. International Journal of Greenhouse Gas Control 27, 146-154.

Schutjens, P., Hanssen, T., Hettema, M., Merour, J., De Bree, P., Coremans, J., Helliesen, G., 2004. Compaction-induced porosity/permeability reduction in sandstone reservoirs: Data and model for elasticity-dominated deformation. SPE Reservoir Evaluation & Engineering 7, 202-216.

Shao, H., Ray, J.R., Jun, Y.-S., 2010. Dissolution and Precipitation of Clay Minerals under Geologic CO2 Sequestration Conditions: CO2−Brine−Phlogopite Interactions. Environmental Science & Technology 44, 5999-6005.

Span, R., Wagner, W., 1996. A new equation of state for carbon dioxide covering the fluid region from the triple-point temperature to 1100 K at pressures up to 800 MPa. Journal of physical and chemical reference data 25, 1509-1596.

Spycher, N., Pruess, K., 2005. CO2-H2O mixtures in the geological sequestration of CO2. II. Partitioning in chloride brines at 12–100° C and up to 600 bar. Geochimica et Cosmochimica Acta 69, 3309-3320.

Vinegar, H.J., Wellington, S.L., 1987. Tomographic imaging of three-phase flow experiments. Review of Scientific Instruments 58, 96-107.

Wellington, S., Vinegar, H., 1987. X-ray computerized tomography. Journal of Petroleum Technology 39, 885-898.

Wyble, D., 1958. Effect of Applied Pressure on the Conductivity Porosity and Permeability of Sandstones. Journal of Petroleum Technology 10, 57-59.

Xu, T., Apps, J.A., Pruess, K., 2004a. Numerical simulation of CO2 disposal by mineral trapping in deep aquifers. Applied geochemistry 19, 917-936.

Xu, T., Ontoy, Y., Molling, P., Spycher, N., Parini, M., Pruess, K., 2004b. Reactive transport modeling of injection well scaling and acidizing at Tiwi field, Philippines. Geothermics 33, 477-491.

Zuluaga, E., Monsalve, J., 2003. Water vaporization in gas reservoirs, SPE Eastern Regional Meeting. Society of Petroleum Engineers.

Zuluaga, E., Muñoz, N., Obando, G., 2001. An Experimental study to evaluate water vaporisation and formation damage caused by dry gas flow through porous media, International Symposium on Oilfield Scale. Society of Petroleum Engineers.

5

Effect of capillary-driven backflow on salt precipitation due to CO_2 injection into brine-saturated porous media

Abstract

CO_2 flow into linear and radial brine-saturated porous media was investigated both by numerical analysis and CT scan aided core-flood experiments. We found that the potential of formation clogging due to salt precipitation depends strongly on the velocity field in the porous medium. Numerical simulation showed that in linear flows, salt accumulation near the inlet occurred only for low injection rates where water evaporation induced steep brine saturation gradients inside the porous medium. Capillary-driven backflow of brine toward the injection point resulted in complete impairment in injectivity. For injection velocities, it was found that capillary-driven backflow is suppressed and injectivity is not negatively affected by the presence of solid salt. For radial flows, however, impairment of injectivity occurred regardless of whether the injection velocity was low or high. Capillary-driven backflow of brine resulted in accumulation of salt near the injection well for both cases. In radial flows, instead, capillary-driven backflow of brine is possible for high injection velocities since the flow velocity decreases with increasing distance from the well.

[Based on: Roels, S.M., Nicolaides, C., Zitha, P.L.J., 2015. Effect of capillary-driven backflow on salt precipitation due to CO_2 injection into brine-saturated porous media. Accepted with revisions in Water Resources Research.]

5.1. Introduction

Rise of energy demand due to population growth and improving living standards in the coming decades could result in substantial increase of anthropogenic CO_2 emissions unless mitigation measures are taken. Global climate change, characterized by extreme weather conditions, rising sea levels and desertification, could be the adverse consequences of increasing CO_2 concentration in the atmosphere (*IEA-ETP*, 2010). The storage of CO_2 captured at power plants, refineries and other major industrial facilities into geological formations appears to be a feasible option for mitigating CO_2 emission into the atmosphere (Metz et al., 2007; Yang et al., 2010). Deep saline aquifers, in particular, are suitable storage sites due their large capacities. They can be used either as a temporary trap of CO_2 intend for later utilization or as a permanent CO_2 disposal.

A major challenge related to CO_2 storage in saline aquifers is the risk of formation clogging due to salt precipitation, which can strongly reduce the storage capacity of the aquifer. Evaporation of water from the formation brine into the injected CO_2 occurs due to the mutual solubility of CO_2 and water (Spycher and Pruess, 2005, 2010). Salt concentration in brine increases as a result, leading eventually to salt precipitation. This causes the porosity of the medium to decrease which may also induce a permeability reduction of the formation rock (Pape et al., 1999; Verma and Pruess, 1988a). Reductions in matrix permeability up to 60% due to salt precipitation induced by CO_2 injection were reported by several authors (Bacci et al., 2011; Muller et al., 2009; Wang et al., 2009; Zuluaga et al., 2002). Although permeability decreased significantly, severe clogging and hence impairment of injectivity was not observed in all cases. Capillary-driven backflow of brine to the injection point seems to be the main factor contributing to clogging of a porous medium during CO_2 injection (André et al., 2014; Lorenz and Müller, 2003; Ott et al., 2012; Peysson et al., 2014; Pruess and Müller, 2009a). However, there is no consensus yet about the exact circumstances for which capillary-driven backflow can lead to complete clogging of the porous medium.

Recently, it was reported that at high injection velocities where hydrodynamic displacement is dominant over water evaporation the influence of capillary-driven backflow on salt precipitation was negligible (Roels et al., 2014). In that study, the effect of salt precipitation on injectivity was investigated using one-dimensional flow through core samples. The distribution of salt precipitation was practically uniform and its effect on injectivity was insignificant. A critical flow rate could be defined above which capillary-driven backflow may not play a role (Ott et al., 2011), as water removal from the core in the gaseous stream is faster than the transport of brine toward the inlet by capillary-driven backflow. At low injection velocities such that water evaporation is dominant compared to hydrodynamic fluid

displacement, brine saturation decreases faster near the injection point establishing a steep saturation gradient. The corresponding capillary pressure gradient results in the suction of brine toward the dryer zone. However, one-dimensional flow regimes do not take into account the significant decrease in flow velocities which occurs in field applications when radial injection takes place.
The aim of this study is to examine the influence of the velocity field within the porous medium on the potential of formation clogging due to salt precipitation. For this purpose, radial CO_2 injection experiments were performed and compared with numerical simulations for high and low injection velocities. First, an overview of the numerical concept is given. After that, the experimental method used to perform radial core flow experiments is described. Then, the results are discussed using the work from Roels et al. (2014) as a baseline for comparison with current radial injection conditions. We show that injection of CO_2 into a radial domain results in different salt precipitation patterns than found under one-dimensional flow conditions.

5.2. Model description

Numerical simulations were carried out in both a 1D and a 2D-axisymmetric domain. The 1D simulations follow the concept used in Roels et al. (2014) which are presented in Chapter 3. Figure 5.1 shows the simulation domain for the 2D-axisymmetrical case. The geometry of the domain represents the shape of the porous medium used to conduct the experiments (see section 5.3.2). The injection well is located in the middle of the domain and penetrates the whole depth of 1.5 cm. The outlet is represented by an opening at the lower part of the domain at a radius of 2.0 cm.

5.2.1. Model formulation

The model encompasses the mass balance equations for water, CO_2, dissolved and precipitated salt and the relevant Darcy's equations (see Eqs. (1) and (2) in Chapter 2). A non-equilibrium mass transfer formulation between brine and CO_2 was adopted. The mass transfer of component H_2O from the brine phase w to the gaseous phase g is described according to Eq. (6) by a constant mass-transfer coefficient and limited by the difference between the solubility limit of water vapor in CO_2 and the actual mass fraction of water vapor in CO_2 (Pinder and Celia, 2006). For 1D simulations instantaneous salt precipitation is assumed when the solubility limit of dissolved salt is reached and in the radial simulations instant salt precipitation is approached by the use of a very high precipitation rate. The effect of salt precipitation, i.e. decrease in porosity, on permeability was described by Eq. (8-10), following the models of Verma and Pruess (1988a).

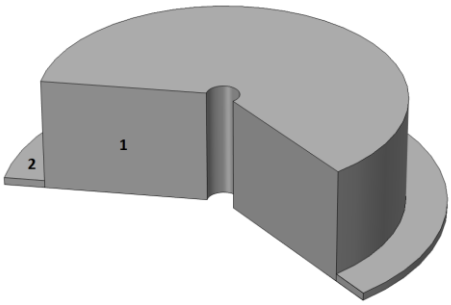

Figure 5.1. Modeling domain with height of 1.5 cm and radius of 2 cm. Domain 1 represents the porous medium and domain 2 represents the outlet.

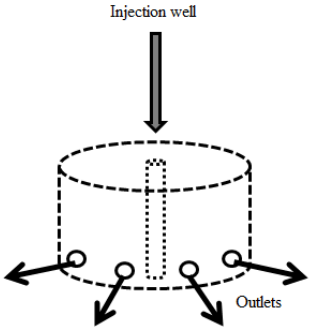

Figure 5.2. Schematic of core set-up used to study CO_2 flow into a radial domain. Injection is done through a well in the center and eight symmetrically located outlets ensure radial flow.

Constitutive relations include relative permeability functions as described by Eq.(4) by an extended Corey model (Brooks and Corey, 1964; Corey, 1954). The capillary pressure-saturation was modelled using the Eq.(5) following the Van Genuchten formulation (Van Genuchten, 1980) and was validated using data measured by mercury injection. For convenience, a few assumptions are made in this model. Due to the small length or radius of the core, and hence the small pressure drop, densities of both CO_2 and brine are assumed to be constant. Viscosities of brine and CO_2 are also kept constant which is a valid assumption under isothermal conditions. CO_2 dissolution can be neglected under ambient pressure and temperature conditions and the porous medium is assumed to be incompressible.

5.2.2. Numerical solution

The physical modeling domain consists of two sections in contact with each other (Figure 5.1). Section 1 is the main domain and represents the core and section 2 represents the outlet. This approach was found most suitable in order to avoid boundary effects on the main domain. The 1D-simulations were coded in MATLAB® using an IMPEM solution scheme as explained earlier in Chapter 3 (Roels et al., 2014). The radial flow simulations were done using the PDE mode for a 2D-axisymmetric domain in COMSOL Multiphysics®.

The domains are initially fully saturated with brine being close to the saturation limit with respect to solutes. At $t = 0$, CO_2 injection starts with a constant flow rate from the inlet of the domain, which are the first node in the 1D linear domain and the

injection well in the 2D radial domain. The outlet is represented by a Dirichlet boundary with the capillary pressure set to zero. More precisely, the last grid block of the modeling domain is situated outside the outlet of the porous medium and has constant properties for all time-steps.

5.3. Experiments

5.3.1. Experimental set-up

The experimental set-up used in this study is shown in Figure 5.3. CO_2 with 99.7% purity was supplied by a pressurized vessel fitted with a pressure regulator and using a Bronkhorst EL-FLOW® mass flow controller. Brine was injected using a P-500 Pharmacia Biotech pump. Two pressure transducers were used of which two for CO_2 flow and one for brine flow (range 0-40 bar). During CO_2 injection, two pressure transducers (range 0-500 mbar and 0-40 bar) were used to accurately measure the pressure drop during brine displacement as well as during the dry-out phase. Inlet temperature was measured using a 2-wire thermocouple with an accuracy of 0.1°C. A data acquisition system from National Instruments™ was used to monitor all the measuring devices. Produced water vapor in the CO_2 phase was measured by connecting the outlet to a cooling bath of 2.5°C, in which the water vapor condensed. The remaining produced volume of CO_2 was measured by gas meter (RITTER MilliGascounter).

5.3.2. Porous media and brine

The porous medium was a cylindrical Bentheimer sandstone core of 4±0.1 cm diameter and 1.5±0.1 cm height (Figure 5.2). The core was completely sealed with epoxy glue to avoid by-passing of the injected liquids. A hole of 4.0±0.1 mm diameter was drilled into the middle of the core to function as an injection well. Eight outlets symmetrically distributed around the core were drilled in order to establish quasi-radial flow conditions. Permeability and porosity were measured with a gas permeameter and pycnometer and were found to be 1.3±0.1 Darcy and 21.0±0.1 %, respectively. The core was placed into a polyether ether ketone (PEEK) core holder which was specially designed and built to cope with the requirements for radial flow. The core holder was placed inside a third generation Siemens SOMATOM CT-scanner for 3D imaging of the rock matrix and the fluid distribution in it.

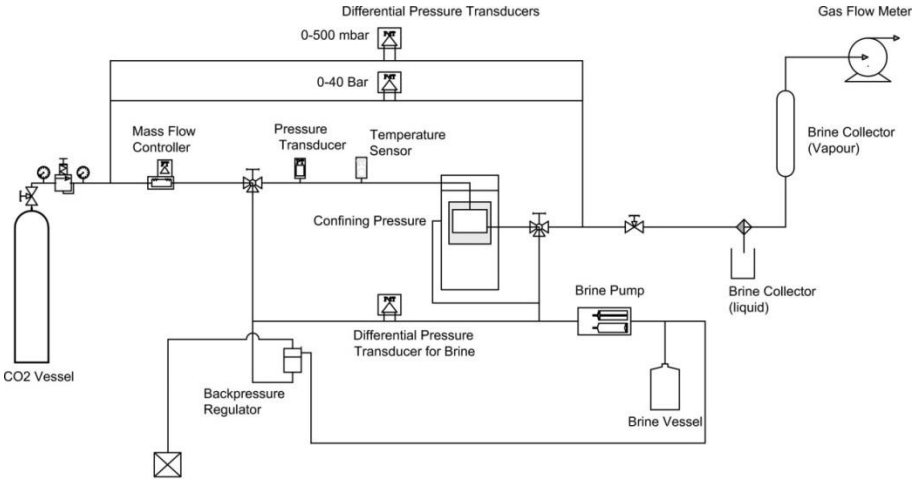

Figure 5.3. Experimental set-up for radial core flooding.

Brine consisting of nearly saturated potassium iodide (KI) solution (58.3 wt%) was used to conduct the experiments. KI has high X-ray attenuation coefficient due to its high density and mass number and enhances the contrast between the CO_2 and brine. In this way optimal CT-scanning results were obtained.

5.3.3. Experimental procedure

Table 5.1 gives an overview of the steps taken during the experiment. Air was removed from the core by flushing it with CO_2 for several hours at ambient temperature and pressure. Next, the core was saturated with brine from bottom to top at 2.5 mL/min for 3 hours. Then, the back pressure was increased to 25 bar and brine injection continued at 1 mL/min for another 2 hours to ensure that any remaining CO_2 was dissolved. CT scans were taken to check that complete brine saturation was established. After that, the pressure was slowly decreased to atmospheric pressure while continuing brine injection with 2.5 mL/min for another 2 hours. CO_2 was injected with 15 NmL/min started upon completing core saturation with brine. Pressure, temperature and pressure drop were all monitored continuously and captured every 10 seconds by a data acquisition system. The injection of CO_2 would be terminated when only minor changes in pressure drop would be observed for a long period of time or when the maximum safety pressure of 20 bar would be reached. To ensure reproducibility the experiment was carried out in duplicate.

5.3.4. CT scanning

The saturation distribution in the porous medium was monitored by taking CT scans. Four slices were taken near the center of the core, each consisting of 512x512 pixels

with the pixel size of 0.3×0.3 mm. The noise for CT images typically ranges from 3 to 20 Hounsfield Units (HU), corresponding to an accuracy of ±2% (Simjoo et al., 2012). CT-scans produce images consisting of voxels with a Hounsfield Unit (HU) according to the average saturation inside the voxel, with a higher HU corresponding to a higher density. The HU for CO_2 at the experimental pressure and temperature is close to the value of air, which is -1000. KI-solution has a value of approximately 3000, which is close to the maximum value of the HU scale (3071). Since solid salt has an even higher density than brine, its phase cannot be distinguished from brine. Therefore, in the CT images, brine and solid salt were treated as a single phase. The files were imported into and processed in MATLAB® to calculate brine saturations at different time steps (Akin and Kovscek, 2003; Simjoo et al., 2012). When imported into MATLAB® for processing, the values are stored as HU+1024 in order to do calculations.

To visualize the distribution of solid salt inside the core, µ-CT scans were taken at the end of the experiment. The core was removed from the core holder and scanned in the µ-CT scanner, with resolution of 22×22×22 µm. The µ-CT images were reconstructed with the Phoenix reconstruction software which is based on the Feldkamp algorithm (Feldkamp et al., 1984), after which the resolution of the images was 43×43×43 µm.

Table 5.1. Experimental procedure used to perform core flooding experiments.

Step	*Description*	*Flow rate*	*Back Pressure*	*Duration*
1	CO_2 flushing	-	1 bar	3 h
2	CT scan (dry)	-	-	-
3	Brine filling	2.5 mL/min	1 bar	3 h
4	Brine filling	1 mL/min	25 bar	2 h
5	Brine filling	2.5 mL/min	1 bar	2 h
6	CT scan (brine)	-	-	-
7	CO_2 injection	15 NmL/min	1 bar	15.5 h
8	CT scans	-	-	-

5.4. Results and discussion

In the following sections the numerical and experimental results are presented. First, a detailed extension of 1D CO_2 injection reported earlier (Roels et al., 2014) is

discussed as a baseline for comparison. Then the numerical and experimental work on radial injection are presented. We compare the effect of injection velocity on salt precipitation distribution and formation clogging in both domains by numerical simulation. The experimental results include saturation distributions at various time steps obtained from CT scanning and pressure drop data measured during the experiments.

The numerical simulations are carried out for two different injection velocities: a high velocity corresponding roughly to injection of 1 Mt/year CO_2 in an aquifer of 100 m thickness and a low velocity of an order of magnitude lower. The high velocity equals the CO_2 injection rate applied in the experiments and the low velocity was chosen such that the effect of capillary-driven backflow could be highlighted. The simulation parameters used are listed in Tables 2.1 and 3.1, and repeated here for convenience in Table 5.2.

Simulation and experimental results are compared qualitatively rather than quantitatively. The mathematical description of dry-out and the effect of salt precipitation on constitutive relations as well as the values of many parameters involved (e.g. porosity-permeability relation, mass transfer rate) are not studied independently and contain assumptions. It would therefore not be useful to give meaning to simulation results in terms of absolute numbers.

Table 5.2. Simulation parameters.

Parameter	*Value*	*Unit*
Injection velocity - high	0.001	ms^{-1}
Injection velocity - low	0.0002	ms^{-1}
S_{wc}	0.1	-
S_{gr}	0.0	-
k_{rw}^{0} *- Brooks and Corey*	1.0	-
k_{rg}^{0} *- Brooks and Corey*	0.5	-
n_w *- Brooks and Corey*	3.5	-
n_g *- Brooks and Corey*	1.5	-
P_d *- Van Genuchten*	3.3×10^{4}	Pa
m - Van Genuchten	0.85	-
μ_{brine}	8.91×10^{-4}	Pa.s
μ_{co2}	1.5×10^{-5}	Pa.s
φ_r *- Verma and Pruess*	0.5	-

Γ - Verma and Pruess	0.95	-
Mass transfer rate coefficient	0.04	s^{-1}

5.4.1. One-dimensional CO_2 injection

The following sections present solid salt distribution and pressure drop during one-dimensional CO_2 injection. In addition, the mass fraction of water vapor in the CO_2 phase is presented to give an insight in evaporation efficiency inside the domain.

5.4.1.1. Numerical results

Figures 5.4 show the precipitated salt saturation profiles along the core length at various time steps and the pressure drop *vs.* time as simulated by the 1D-model for high and low injection velocities. At high injection velocity the salt saturation decreases linearly as the distance from the inlet increases (Figure 5.4a). The slope of the graphs increases gradually from 0 to 2.3/m with time indicating that salt accumulation along the core is not completely uniform. However, pressure drop decreases (Figure 5.4b) during the entire simulation and the presence of precipitated salt does not influence the injectivity.

For a lower injection rate, the salt concentration profiles are much steeper indicating that salt accumulates near the inlet of the domain (Figure 5.4c). The precipitated salt saturation increases until it reaches 0.5, when the permeability reduces to zero, as described by the porosity-permeability relationship (see Eqs. (8-10)). Figure 5.4d shows the corresponding pressure drop simulation. After approximately 4200 PV of CO_2 injected the pressure drop starts to increase until the inlet is completely clogged and the simulation is aborted.

Figure 5.5 shows the mass fraction of water vapor in CO_2 along the 1D-domain for both high and low injection velocity. Because of the constant evaporation rate coefficient assumed in this study, these profiles are constant from the moment breakthrough occurs until complete dry-out starts to proceed from the inlet. The results show that in case of low injection velocity the solubility limit of 0.028 (-) water vapor in CO_2 is reached at a distance of approximately 2 cm from the inlet. This means that after this point water uptake by the CO_2 stream does not occur and therefore a large quantity of water evaporates in a short distance, leading to a steep saturation gradient. For the higher injection velocity the solubility limit is not reached inside the domain. The flat profile shows that evaporation takes place uniformly throughout the entire domain and a brine saturation gradient is not established.

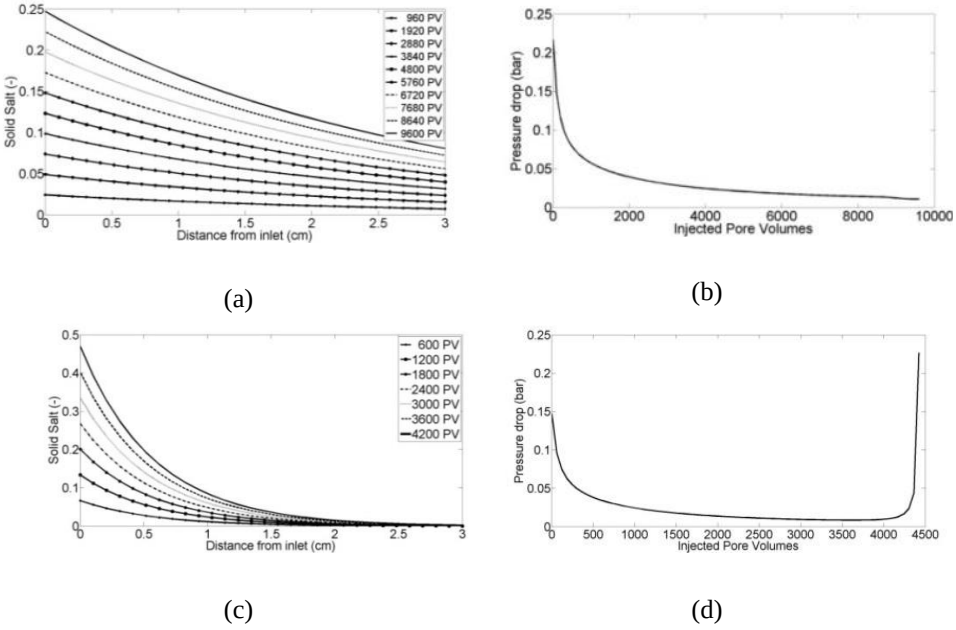

Figure 5.4. Solid salt saturation and corresponding pressure drop profiles at various time steps for (a and b) high injection velocity and (c and d) low injection velocity. Salt accumulation and complete formation clogging only occur at lower injection velocity.

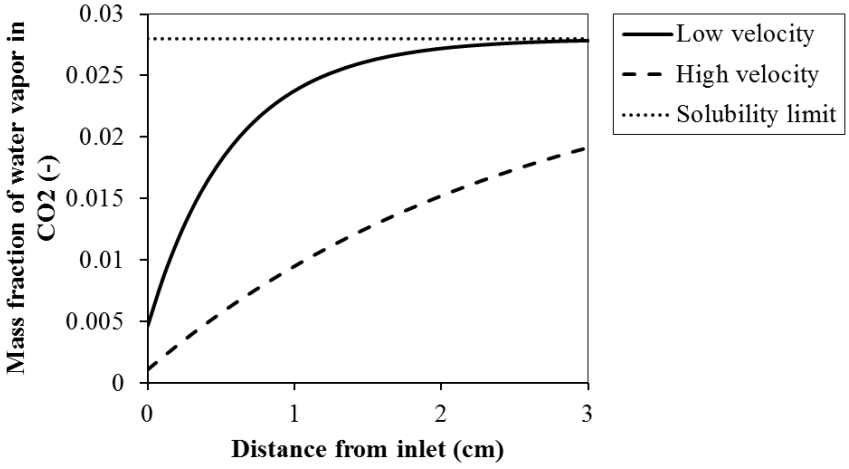

Figure 5.5. Mass fraction of water vapor in CO_2 along the domain. In case of low injection velocity the solubility limit (0.028) is reached whereas for high injection velocity the limit is not reached inside the domain.

5.4.1.2. Experimental results

Salt precipitation results from previous work (Roels et al., 2014) containing a one-dimensional flow through experiment are shown in Figure 5.6. It was found that salt precipitated rather uniformly inside the core and no clogging of the porous medium was observed. The solid salt profile shows a slight increase at a distance of 1.0 cm from the inlet which was most likely due to heterogeneities in porosity. The results indicated that the high ratio of injection rate versus evaporation rate (i.e. kinetic evaporation) prevented CO_2 from becoming completely saturated with brine and evaporation could take place throughout the entire core. Therefore no gradient in brine saturation was established, and hence no capillary-driven backflow occurred.

The pressure drop was found to be decreasing during the experiment (Figure 5.7), even though salt precipitated inside the porous medium. This can be explained by the fact that the increase in CO_2 relative permeability caused by the increase in CO_2 saturation can counteract the decrease in permeability of the porous medium in agreement with others (Ott et al. (2012). As long as salt precipitates in the pore space previously occupied by brine (capillary-driven backflow is not significant) pressure drop will decrease during dry-out and injectivity impairment will not occur.

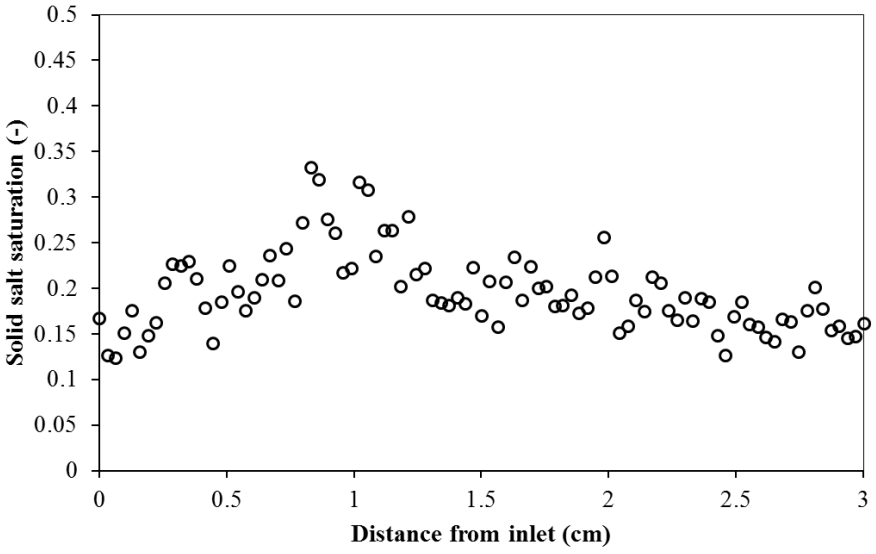

Figure 5.6. Solid salt at the end of one-dimensional flow experiment (Roels et al., 2014). Precipitated salt was found to be equally distributed inside the core.

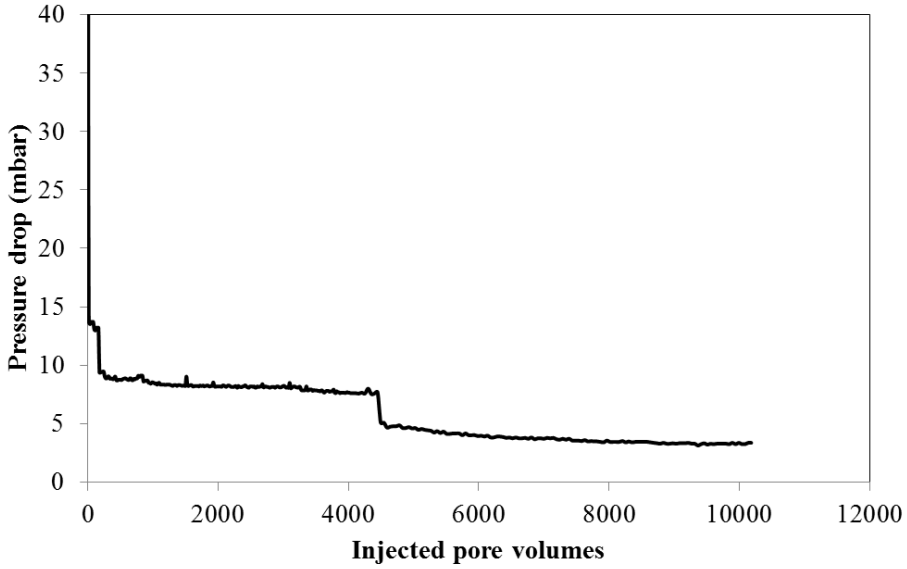

Figure 5.7. Pressure drop during one-dimensional flow experiment (Roels et al., 2014). The decrease in permeability caused by salt precipitation is counteracted by the increase in CO_2 relative permeability and no injectivity impairment was found.

5.4.2. Radial injection of CO_2

The results from CO_2 injection into a radial domain are discussed in the following subsections. The numerical results show the potential of formation clogging by the analysis of solid salt distribution and pressure drop for the two injection velocities mentioned before. The experimental results show brine saturation profiles derived from CT scans and high resolution localization of salt precipitation. At last, the pressure drop measurement during the experiment is presented.

5.4.2.1. Numerical results

Figure 5.8 shows the precipitated salt saturation and the pressure drop simulated by the radial model for high (Figure 5.8a and 5.8b) and low (Figure 5.8c and 5.8d) injection velocities. The solid salt profiles show the distribution at the end of the simulation which is either when the domain is completely dry, or when permeability has reached zero. Complete clogging of the domain (i.e. permeability tends to zero) is reached when the solid salt saturation approaches the maximum value of 0.5 (see Eq.(8-10)). The results show that complete clogging is reached for both high and low injection velocities after respectively 3800 and 820 PV of CO_2 injected. The pressure drop profiles show a gradual increase after approximately 2500 and 600 PV, followed by a dramatic increase when total blocking is reached. The gradient of

increase in pressure drop due to salt precipitation depends on the parameters chosen in the permeability-porosity relationship and should therefore be interpreted as a trend rather than an absolute slope.

In contrast to the 1D simulations clogging of the domain occurs in case of both high and low injection velocity. This indicates that capillary-driven backflow of brine is stronger in the radial domain than in the one-dimensional domain. As backflow is driven by the gradient in brine saturation caused by evaporation, we know that this gradient is larger in the radial domain.

A closer look at the mass fraction of water vapor in CO_2 (Figure 5.9) shows that CO_2 becomes saturated with water vapor for both high and low injection velocities. The efficiency with which the CO_2 takes up water vapor depends on its flow rate (in case of constant evaporation rate coefficient), with a more efficient uptake for lower injection rates. In contrast to the 1D case, the solubility limit is reached for both high and low injection velocities. In a one-dimensional injection domain the CO_2 velocity is constant whereas in radial velocity field the velocity decreases with increasing distance from the well. Thus, even for high injection rates evaporation becomes efficient compared to flow rate at a certain distance from the injection well. A gradient in brine saturation can be established which makes that capillary-driven backflow can be stronger in a radial injection domain.

5.4.2.2. Experimental results

Figure 5.10 shows CT scan slices obtained at a fixed location inside the core. On top, slices are shown for which brine saturation is calculated. The middle of each slice shows the injection well and has a brine saturation of zero immediately after CO_2 injection started. The images below show the corresponding histograms for the raw CT scan data starting with the histogram for the dry image. Recall that the attenuation values are shifted by 1024 compare to the actual Hounsfield Units (HU).

The first image shows the core after CO_2 flushing (Dry) with a corresponding peak in the histogram of about 2300 HU value. After complete brine filling (second image: Brine) the HU values increase to > 4100 which cannot be captured by the HU scale. A small artefact can be observed under the well caused by the rectangular shape of the image. Images 3 and 4 are taken at 0.01 h and 0.017 h and show the displacement of brine by CO_2, which is not efficient due to gravity segregation and the mobility contrast of the two fluids. A large amount of brine remains in the core after CO_2 breakthrough. The histograms show a substantial decrease in HU values, from over 4100 to an average of about 3500 compared to the brine-saturated image. The main mechanism causing dry-out of the porous medium thereafter is water evaporation. After 15.5 h of injection the porous medium shows significantly lower brine saturation, as can be inferred from the corresponding histogram. However, the area around the well shows a strong increase in attenuation coefficient which indicates the presence of precipitated salt.

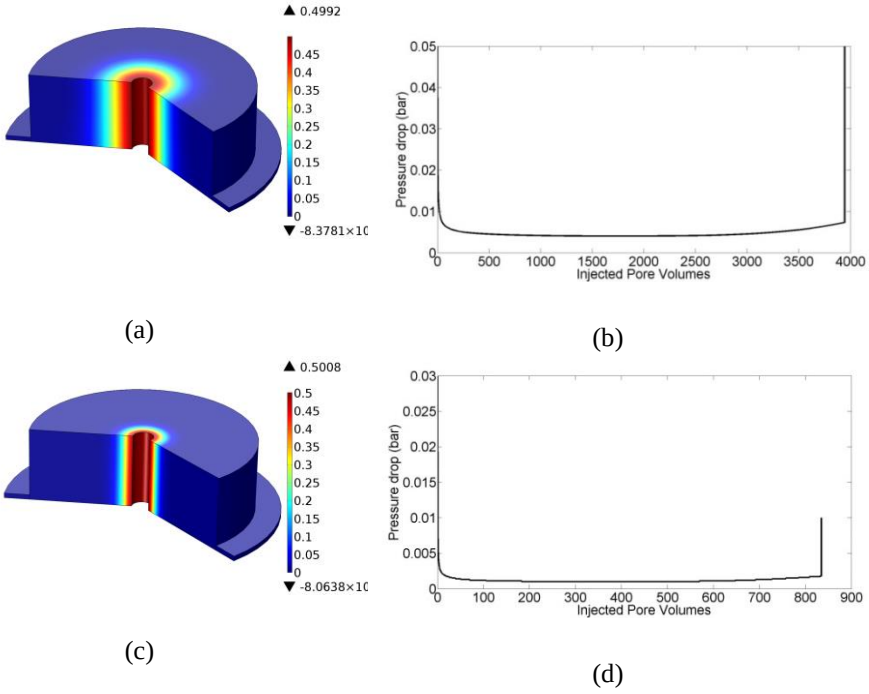

Figure 5.8. Solid salt at the end of the simulation for high (a and b) and low (c and d) injection velocity. Solid salt accumulates around the injection well. Corresponding pressure drop over time for high (b) and low (d) injection velocity with clogging resulting in an increase in pressure drop.

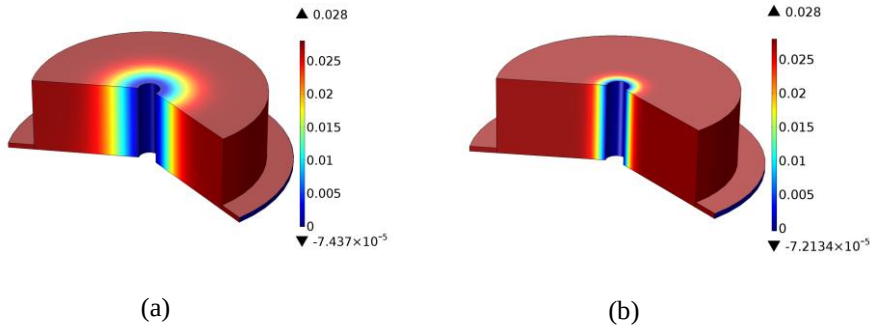

Figure 5.9. Mass fraction of water vapor in CO_2 for (a) high injection velocity and (b) low injection velocity. Solubility limit of 0.028 is reached inside the domain in both scenarios.

Figures 5.11 and 5.12 show µ-CT slices obtained immediately after the end of the CO_2 injection at various depths and widths. The gray scale ranges according to attenuation coefficient, with a lighter color for higher densities: hence solid salt is represented by white and CO_2 by black. It can be clearly observed that salt precipitated in the vicinity of the injection well, which supports the above argument that solid salt is present at 15.5 h in Figure 5.10.

The pressure drop over the core was measured continuously during CO_2 injection (Figure 5.13). The zoomed area represents the pressure drop for the first 12 minutes in which brine was displaced by CO_2. After breakthrough the pressure drop stabilized at approximately 55 mbar for 9 hours. After 9 hrs the pressure drop starts to increase gradually until it reaches 20 bar after approximately 15 hrs of injection. The increase in pressure drop indicates complete formation clogging due to precipitation of solid salt. The experiment was terminated when the pressure reached 20 bar to comply with laboratory safety regulations.

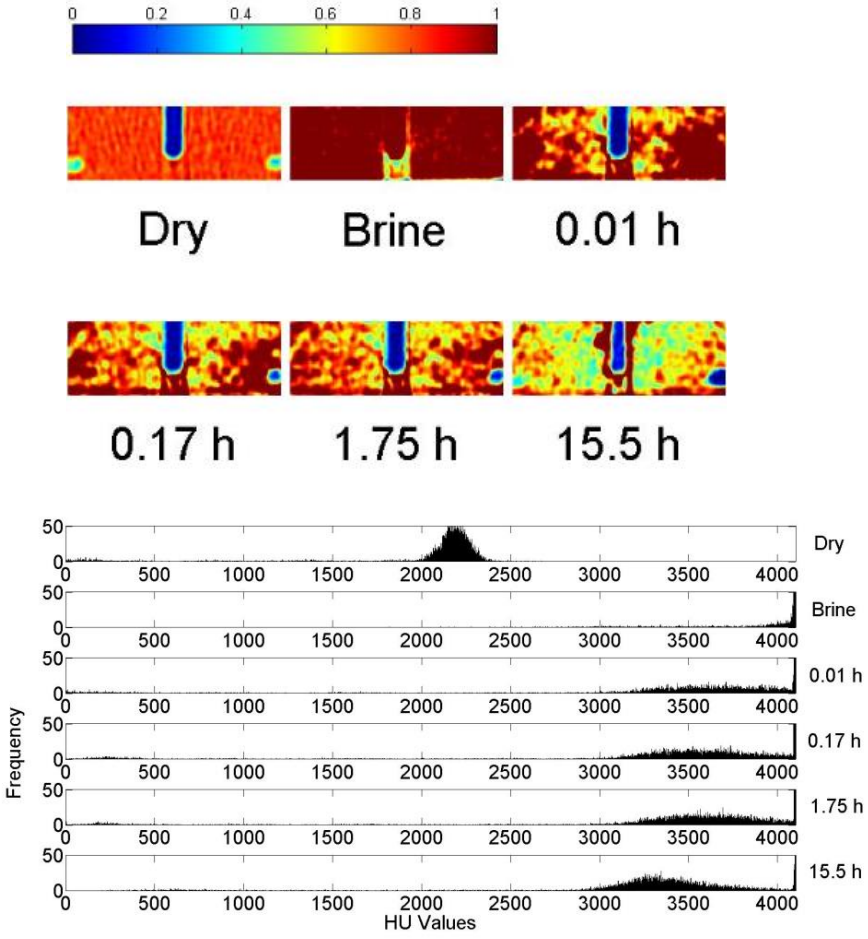

Figure 5.10. Top: Brine saturation inside the porous medium at various times. The saturation decreases with time and clogging of the well can be observed after 15.5 h of CO_2 injection. Bottom: Histograms belonging to the corresponding raw data. The decrease in HU shows that the core is drying-out.

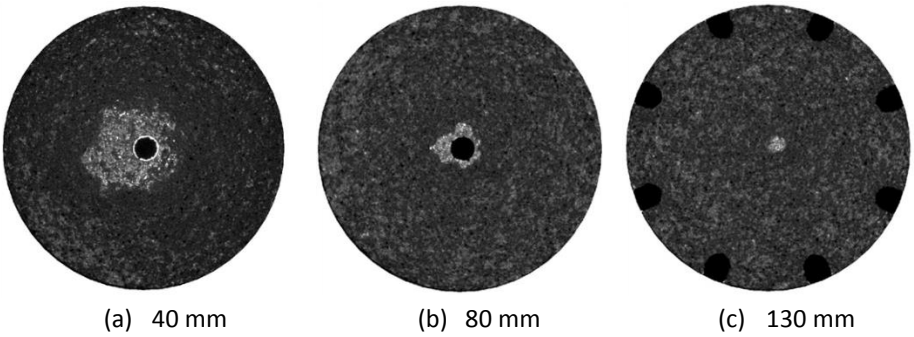

Figure 5.11. Micro-CT images taken at various depths from the top of the core. White corresponds to higher densities (salt) and black corresponds to lower densities (CO_2). The porous medium is shown in gray.

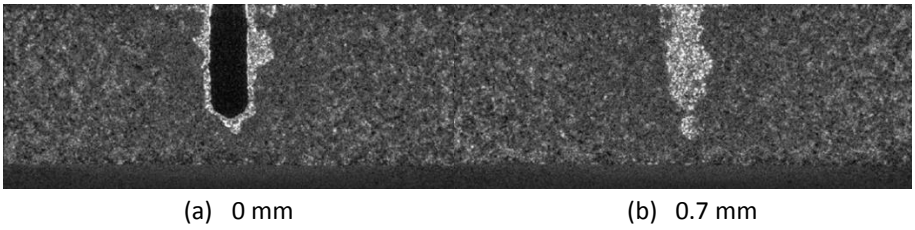

Figure 5.12. Micro-CT images taken at various distances with (a) at the center of the core and (b) at 0.7 mm from the center. White corresponds to higher densities (salt) and black corresponds to lower densities (CO_2). The porous medium is shown in gray.

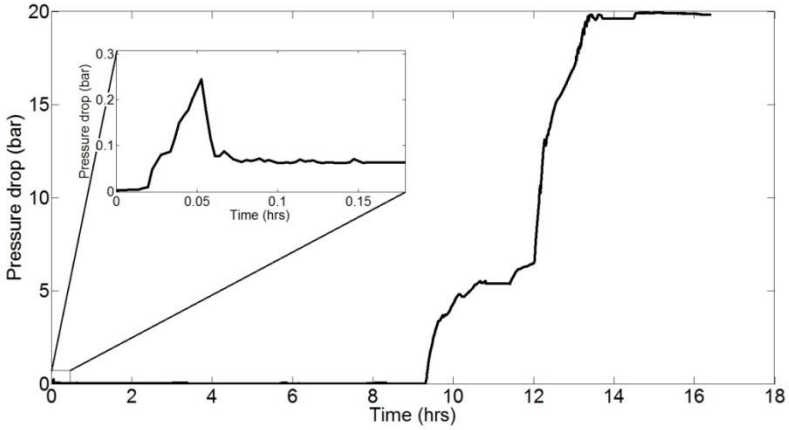

Figure 5.13. Pressure drop over the core during CO_2 injection. After approximately 9 hours the pressure drop starts to increase due to the precipitation of salt. The enlarged section shows the pressure drop during displacement of the brine by CO_2.

5.5. Conclusions

The influence of flow velocity field on formation clogging due to salt precipitation induced by CO_2 injection was investigated by both numerical simulations and experiments. Numerical and experimental work in radial injection domains was performed and compared with previous work on CO_2 injection in a one-dimensional domain (Roels et al., 2014). The effect of salt precipitation on injectivity was studied for both high and low injection velocities.

We found complete impairment of injectivity caused by the precipitation of salt for both high and low injection rates in the radial domain. Due to capillary-driven backflow salt accumulated in the vicinity of the well until complete clogging occurred. This is in contrast to the findings for a one-dimensional injection domain, where salt accumulation near the injection point was only found in case of low injection velocity. For the high injection velocity capillary-driven backflow and salt accumulation were not observed. Instead, salt precipitated where the remaining brine previously filled the pores. In this case, the decrease in the absolute permeability due to salt precipitation is counteracted by the increase in CO_2 relative permeability and therefore impairment of injectivity does not occur.

The spatial difference in salt precipitation between the radial and one-dimensional domain is caused by a difference in velocity field. The efficiency of evaporation

determines the rate of uptake of water vapor into the CO_2 stream and hence whether a gradient in brine saturation will occur in the domain. At high injection velocity the evaporation rate is low compared to the flow rate so that CO_2 does not become saturated with water vapor and evaporation occurs throughout the whole domain. No gradient in brine saturation is established and therefore no capillary-driven backflow and salt accumulation occur. However, in the radial domain the flow velocity decreases with increasing distance from the injection well, enabling a more efficient evaporation and the establishment of a brine saturation gradient. This causes a continuous transport of dissolved salt toward the drying zone and subsequent precipitation. As evaporation continues solid salt accumulates near the inlet until complete clogging occurs, i.e. injectivity approaches zero. Therefore, in the radial domain capillary-driven backflow is allowed even for high injection velocities and the risk of formation clogging is higher than in the one-dimensional domain.
Future study should focus on the determination of the distance from the well at which accumulation of salt will occur at a certain injection velocity. This will allow accurate prediction of the impact of salt accumulation on injectivity and of estimations of required volumes needed in case fresh water injection measures should be applied.

Acknowledgments

This research was done as part of CATO 2, the Dutch National Program for CCS. The authors are grateful for the Dutch Ministry of Economic Affairs and the sponsoring companies for funding. We would like to thank Marc Friebel, Dirk Delforterie, Wim Verwaal and Ellen Meijvogel-de Koning, technical staff of our laboratory, for their help with conducting the experiments.

Bibliography

Akin, S., Kovscek, A., 2003. Computed tomography in petroleum engineering research. Geological Society, London, Special Publications 215, 23-38.

André, L., Peysson, Y., Azaroual, M., 2014. Well injectivity during CO2 storage operations in deep saline aquifers–Part 2: Numerical simulations of drying, salt deposit mechanisms and role of capillary forces. International Journal of Greenhouse Gas Control 22, 301-312.

Bacci, G., Korre, A., Durucan, S., 2011. Experimental investigation into salt precipitation during CO2 injection in saline aquifers. Energy Procedia 4, 4450-4456.

Brooks, R., Corey, T., 1964. Hydraulic Properties of Porous Media.

Corey, A.T., 1954. The interrelation between gas and oil relative permeabilities. Producers monthly 19, 38-41.

Feldkamp, L., Davis, L., Kress, J., 1984. Practical cone-beam algorithm. JOSA A 1, 612-619.

International Energy Agency-Energy Technology Perspectives (IEA-ETP). Scenarios and Strategies to 2050. Paris, France, 2010.

Lorenz, S., Müller, W., 2003. Modelling of halite formation in natural gas storage aquifers, Proceedings, TOUGH Symposium 2003.

Metz, B., Davidson, O., Bosch, P., Dave, R., Meyer, L., 2007. IPCC, 2007: Climate Change 2007: Mitigation. Contribution of Working Group III to the Fourth Assessment Report of the Intergovernmental Panel on Climate Change. Cambridge University Press, Cambridge, United Kingdom and New York, NY, USA.

Muller, N., Qi, R., Mackie, E., Pruess, K., Blunt, M.J., 2009. CO2 injection impairment due to halite precipitation. Energy procedia 1, 3507-3514.

Ott, H., de Kloe, K., Marcelis, F., Makurat, A., 2011. Injection of supercritical CO2 in brine saturated sandstone: Pattern formation during salt precipitation. Energy Procedia 4, 4425-4432.

Ott, H., de Kloe, K., van Bakel, M., Vos, F., van Pelt, A., Legerstee, P., Bauer, A., Eide, K., van der Linden, A., Berg, S., 2012. Core-flood experiment for transport of reactive fluids in rocks. Review of Scientific Instruments 83, 084501.

Pape, H., Clauser, C., Iffland, J., 1999. Permeability prediction based on fractal pore-space geometry. Geophysics 64, 1447-1460.

Peysson, Y., Andre, L., Azaroual, M., 2014. Well injectivity during CO2 storage operations in deep saline aquifers—Part 1: Experimental investigation of drying effects, salt precipitation and capillary forces. international journal of Greenhouse Gas Control 22, 291-300.

Pinder, G.F., Celia, M.A., 2006. Subsurface hydrology. John Wiley & Sons.

Pruess, K., Müller, N., 2009. Formation dry-out from CO2 injection into saline aquifers: 1. Effects of solids precipitation and their mitigation. Water Resources Research 45, W03402.

Roels, S.M., Ott, H., Zitha, P.L., 2014. μ-CT analysis and numerical simulation of drying effects of CO2 injection into brine-saturated porous media. International Journal of Greenhouse Gas Control 27, 146-154.

Simjoo, M., Nguyen, Q.P., Zitha, P.L.J., 2012. Rheological Transition during Foam Flow in Porous Media. Industrial & Engineering Chemistry Research 51, 10225-10231.

Spycher, N., Pruess, K., 2005. CO2-H2O mixtures in the geological sequestration of CO2. II. Partitioning in chloride brines at 12–100° C and up to 600 bar. Geochimica et Cosmochimica Acta 69, 3309-3320.

Spycher, N., Pruess, K., 2010. A phase-partitioning model for CO2–brine mixtures at elevated temperatures and pressures: application to CO2-enhanced geothermal systems. Transport in porous media 82, 173-196.

Van Genuchten, M.T., 1980. A closed-form equation for predicting the hydraulic conductivity of unsaturated soils. Soil science society of America journal 44, 892-898.

Verma, A., Pruess, K., 1988. Thermohydrological Conditions and Silica Redistribution Near High-Level Nuclear Wastes Emplaced in Saturated Geological Formations. J. Geophys. Res. 93, 1159-1173.

Wang, Y., Mackie, E., Rohan, J., Luce, T., Knabe, R., Appel, M., 2009. Experimental study on halite precipitation during CO 2 sequestration, International Symposium of the Society of Core Analysts held in Noordwijk, The Netherlands, pp. 27-30.

Yang, F., Bai, B., Tang, D., Shari, D.-N., David, W., 2010. Characteristics of CO2 sequestration in saline aquifers. Petroleum Science 7, 83-92.

Zuluaga, E., Castrillon, J., Monsalve, J., Rendon, A., 2002. Experiments on Water Vaporisation in Porous Media, Canadian International Petroleum Conference. Petroleum Society of Canada.

6

Capillary-driven transport of dissolved salt to the drying zone during CO_2 injection in homogeneous and layered porous media

Abstract

A major challenge of CO_2 injection into saline aquifers is the risk of formation clogging due to salt precipitation. Capillary-driven flow of brine can provide a continuous transport of dissolved salt toward the dry zone around the injection well where it ultimately precipitates due to water evaporation. In this study, core flooding experiments were performed in homogeneous coarse textured cores and in layered cores consisting of a coarse textured layer overlying a fine textured layer. CO_2 was injected through a well in the upper part of the cores and the bottom parts functioned as brine sources. Impairment in injectivity was found due to accumulation of precipitated salt caused by capillary-driven flow from the brine sources to the upper dryer region. Compared to flow domains without a brine source, we found that capillary-driven upward flow at first prevents complete clogging because the porous medium remains wet, but eventually leads to a more severe clogging of the entire domain. The results show that after sufficient dry-out, a coarse textured injection layer can draw brine from an underlying a fine textured layer by capillary forces. A connected fine textured layer can therefore contribute to salt precipitation and clogging of the injection layer.

[Based on: Roels, S.M., El Chatib, N., Nicolaides, C., Zitha, P.L.J., 2015. Capillary-driven transport of dissolved salt to the drying zone during CO_2 injection in homogeneous and layered porous media. Accepted for publication in Transport in Porous Media].

6.1. Introduction

Formation clogging during CO_2 injection caused by precipitation of salt can decrease storage potential substantially. Reduced storage capacity can occur by (1) a decrease in available pore space caused by the presence of solid salt (e.g. Bacci et al., 2011; Hurter et al., 2007; Pruess and Müller, 2009a) and (2) complete clogging of the porous medium in the vicinity of the injection well by solid salt accumulation (e.g. Giorgis et al., 2007; Muller et al., 2009; Peysson et al., 2014). Whether salt precipitation will affect the injectivity depends on its distribution inside the porous medium. In case viscous forces dominate over capillary forces, salt precipitates locally and the decrease in soil permeability due to salt precipitation can be counteracted by the increase in relative permeability caused by the increase in CO_2 saturation (Ott et al., 2011; Roels et al., 2014). When capillary forces are dominant over viscous forces, complete clogging can occur by accumulation of salt via continuous transport of brine by capillary forces toward to the dry zone around the injection well (Alkan et al., 2010; Peysson, 2012; Roels et al., 2015).

Capillary-driven flow of brine occurs due to a gradient in brine saturation, which can be established by evaporation. Evaporation of water from the formation brine into the injected CO_2 is a complex phenomenon: it occurs due to the mutual solubility of CO_2 and water (Spycher and Pruess, 2005, 2010). The rate of evaporation depends on factors including interfacial area between brine and CO_2 (Niessner and Hassanizadeh, 2009), persistence of liquid pathways to supply brine to the drying front (Lehmann et al., 2008; Nachshon et al., 2011; Shokri et al., 2010), CO_2 flow velocity (Zuluaga et al., 2001) and thermodynamic properties which determine the vapor pressure. The efficiency of evaporation determines the steepness of the gradient in brine saturation inside the porous medium and therefore the significance of capillary-driven flow.

Recently, we have shown that at high CO_2 injection velocities the assumption of local equilibrium for evaporation leads to an overestimation of salt accumulation near the inlet (Roels et al., 2014). Controlled μ-CT scan experiments showed that solid salt was uniformly distributed inside the porous medium after complete dry-out and impairment in injectivity was not found. The findings were supported by numerical simulation including a kinetic phase partitioning between brine and CO_2. This suggested that injection velocity plays a major role in the potential of clogging. At high injection velocities, CO_2 does not become saturated with water vapor and evaporation takes place throughout the whole domain. Brine saturation decreases gradually in the entire domain and capillary-driven backflow does not occur. Similar results were found by André et al. (2014) and Peysson et al. (2014) where capillary-driven backflow was limited above a threshold gas injection rate and salt

accumulation near the inlet was only found for low injection velocities. The threshold value of the injection rate was found to depend on the salinity of the brine.
Potential CO_2 injection sites consist of a high permeable, coarse-textured injection layer confined by low permeable, fine-textured layers (aquitards) (Hosa et al., 2011). Brine inside the low permeable, fine-textured layer is retained at the interface between the fine and coarse layers (within the fine-textured layer) by capillary forces. When the entry pressure for gas of the fine-textured layer is reached (i.e. until the entry pressure for brine for the coarse layer is reached) gas and water redistribute between the layers until equilibrium pressure is established (Schroth et al., 1998b). This suggests that when the entry pressure is overcome, brine from the fine-textured layer is transported to the drying zone where it contributes to formation clogging. A capillary pressure jump between fine and coarse layers followed by a relaxation through water redistribution was also reported by Shokri et al. (2010). In addition, flow from micro-pores to macro-pores was observed in a dual-porosity system (Ott et al., 2013). The micro-porous volume functions as a brine reservoir and gradually transports dissolved salt to the macro-porous channels as dry-out proceeds.
The primary goal of the present study was to investigate permeability impairment due to salt accumulation induced by capillary-driven flow of brine, arising from connected brine sources. CO_2 injection experiments were performed to investigate brine redistribution dynamics during dry-out of a porous medium. Capillary-driven flows and the resulting permeability impairment were examined for isolated porous media and media in contact with a source of brine. The effect of capillary suction from a fine-textured layer to a coarse- textured layer was studied using a layered porous medium. The following section discusses experimental details on the core floods. After that, the experimental results are presented and evaluated using fundamental principles on dry-out during two-phase flow. Concluding remarks on the potential of formation clogging and the influence of capillary-driven flow on solid salt distribution are presented in the last section.

6.2. Core flooding experiments

6.2.1. Experimental set-up

The experimental set-up used in this study is shown in Figure 6.1. CO_2 with 99.7% purity was supplied from a pressurized vessel using a Bronkhorst EL-FLOW® mass flow controller. Brine solution was injected by a P-500 Pharmacia Biotech pump. During CO_2 injection, two pressure transducers (range 0-500 mbar and 0-40 bar) were used to accurately measure the pressure drop during brine displacement as well as during the dry-out phase. A third pressure transducer (range 0-40 bar) was used

during brine filling. Inlet temperature was measured using a 2-wire thermocouple with an accuracy of 0.1°C. A data acquisition system from National Instruments™ was used to monitor the measuring devices. Produced water vapor in the CO_2 phase was measured by connecting the outlet to a cooling bath of 2.5°C, in which the water vapor condensed. The remaining produced volume of CO_2 was measured by a gas meter (RITTER MilliGascounter).

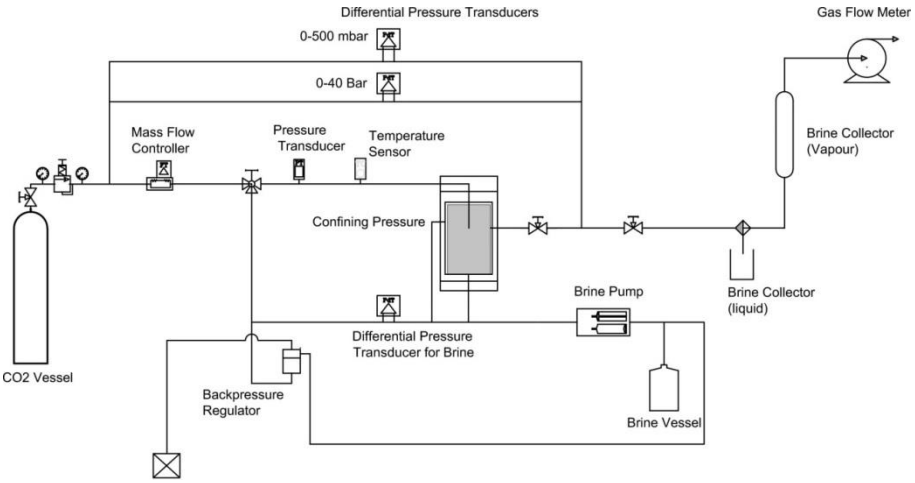

Figure 6.1. Experimental set-up for radial core flooding.

6.2.2. Porous media and brine

The first set of experiments were performed with a cylindrical macroscopically homogeneous Bentheimer sandstone core of 4±0.1 cm diameter and 9±0.1 cm height (Figure 6.2b). The second set of experiments was performed on a layered system, formed by an upper layer consisting of Bentheimer sandstone and bottom layer consisting of Berea sandstone. The sandstone samples had both diameter 4.0±0.1 cm diameter and heights 1.5±0.1 and 7.5±0.1 cm, respectively (Figure 6.2c). Figure 6.2a shows the Bentheimer core of 4±0.1 cm diameter and 1.5±0.1 cm height used in Chapter 5, of which the results are used for comparison. The cores were completely sealed with epoxy glue to avoid by-passing of the injected liquids. An injection well of 4 mm diameter and 1.5 cm depth was drilled from the top in the middle of the core. Eight outlets symmetrically distributed around the core were drilled in the epoxy layer in order to establish quasi-radial flow conditions. The properties of the cores are listed in Table 6.1. The capillary pressure parameters for Bentheimer were obtained by fitting the Van Genuchten equation (Van Genuchten, 1980) to the

capillary pressure data measured by mercury injection (Roels et al., 2014). For Berea we used capillary pressure parameters obtained from Berg et al. (2013) for a Berea sandstone with similar permeability. The cores were placed into a polyether ether ketone (PEEK) core holder which was specially designed and built to cope with the requirements for radial flow. The core holder was placed inside a third generation Siemens SOMATOM CT-scanner for 3D imaging of the rock matrix and the fluid distribution in it. Brine consisting of nearly saturated potassium iodide (KI) solution (58.3 wt%) was used to conduct the experiments. KI has high X-ray attenuation coefficient due to its high density and mass number and enhances the contrast between the CO_2 and brine. In this way optimal CT-scanning results were obtained.

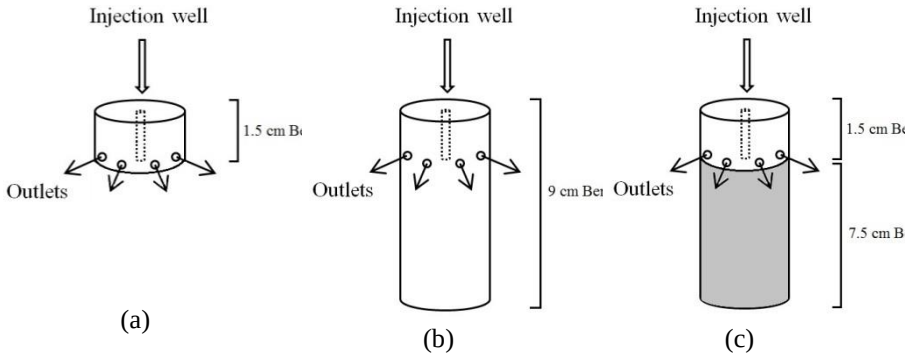

Figure 6.2. Schematics of cores used for the flooding experiments with (a) short Bentheimer core (Roels et al., 2015), (b) long Bentheimer core, and (c) layered core of Bentheimer and Berea. The bottom part of (b) and (c) function as brine sources for capillary-driven flow.

Table 6.1. Sandstone properties and parameters.

Property	*Bentheimer*	*Berea*	*Unit*
Porosity	0.21±0.01	0.21±0.01	-
Permeability	$1.3\pm0.1 \times 10^{-12}$	$2.4\pm0.1 \times 10^{-13}$	m^2
P_d *– Van Genuchten*	3.3×10^4	6.0×10^4	Pa
m – Van Genuchten	0.85	0.9	-

6.2.3. Experimental procedure

Table 6.2 gives an overview of the steps taken during the experiments which followed the procedure used in Chapter 5. Air was removed from the core by flushing it with CO_2 for several hours at ambient temperature and pressure. Next, the

core was saturated with brine from bottom to top at 2.5 mL/min for 3 hours. Then, the back pressure was increased to 25 bar and brine injection continued at 1 mL/min for another 2 hours to ensure that any remaining CO_2 was dissolved. CT scans were taken to check that complete brine saturation was established. After that, the pressure was slowly decreased to atmospheric pressure while continuing brine injection with 2.5 mL/min for another 2 hours. After completion of the core saturation with brine, CO_2 injection was initiated with 15 NmL/min, corresponding to injection of 1 Mt/year in an aquifer of 100 m thickness under 45°C and 100 bar. Pressure and pressure drop were monitored continuously and captured every 10 seconds by a data acquisition system. The entire experiment was performed at ambient temperature which was monitored using a 2-wire thermocouple with an accuracy of 0.1°C. Injection of CO_2 would be terminated when only minor changes in pressure drop would be observed for a long period of time (±0.5 bar), when the maximum safety pressure of 20 bar would be reached or when the maximum duration of the experiment of 6 days would be reached. To ensure reproducibility the experiments were carried out in duplicate.

6.2.4. CT scanning

The saturation distribution inside the porous medium was monitored by taking CT scans every few hours. Four slices were taken near the center of the core, each consisting of 512×512 pixels with the pixel size of 0.3×0.3 mm. The noise for CT images typically ranges from 3 to 20 Hounsfield Units (HU), corresponding to an accuracy of ±2% (Simjoo et al., 2012). CT-scans produce images consisting of voxels with a Hounsfield Unit (HU) according to the average saturation inside the voxel, with a higher HU corresponding to a higher density. The attenuation coefficient of pure CO_2 at the experimental pressure and temperature is close that of air, which is -1000. KI-solution has a value of approximately 3000, which is close to the maximum value of the HU scale, i.e. 3071 HU. Since solid salt has an even higher density than brine, its phase cannot be distinguished from brine. Therefore, in the CT images, brine and solid salt were treated as a single phase. The files were imported into and processed in MATLAB® to calculate brine saturations at different time steps (Akin and Kovscek, 2003; Simjoo et al., 2012). When imported into MATLAB® for processing, the values are stored as HU+1024 in order to do calculations.

To visualize the distribution of solid salt in the core, µ-CT scans were taken at the end of the experiment. The core was removed from the core holder and scanned in the µ-CT scanner, with resolution of 22×22×22 µm. The micro-CT images were reconstructed with the Phoenix reconstruction software which is based on the Feldkamp algorithm (Feldkamp et al., 1984), after which the resolution of the images was 43×43×43 µm. The µ-CT images were reconstructed with the Phoenix reconstruction software which is based on the Feldkamp algorithm (Feldkamp et al.,

1984), after which the resolution of the images was decreased to 43×43×43 µm, in order to obtain a workable file size.

Table 6.2. Experimental procedure used to perform core flooding experiments.

Step	*Description*	*Flow rate*	*Back Pressure*	*Duration*
1	CO_2 flushing	-	1 bar	3 h
2	CT scan (dry)	-	-	-
3	Brine filling	2.5 mL/min	1 bar	3 h
4	Brine filling	1 mL/min	25 bar	2 h
5	Brine filling	2.5 mL/min	1 bar	2 h
6	CT scan (brine)	-	-	-
7	CO_2 injection	15 NmL/min	1 bar	144 h
8	CT scans	-	-	-

6.3. Results and discussion

In the following sections the experimental results are presented and discussed. In depth analysis of driving forces of salt accumulation is described for dry-out of porous media with and without a brine source. At first, the results of CO_2 injection into a radial domain from Roels et al. (2015) are presented as a baseline for dry-out without connected brine source. After that, we discuss the experimental results from present study, followed by a comparison of the effect of salt precipitation on injectivity.

6.3.1. Porous media dry-out and capillary-driven backflow: short core

Figure 6.3 shows the CT scans for CO_2 injection into a radial domain without brine source, as shown in Figure 5.10 (see Chapter 5). The first two scans, taken at 0.6 min and 1 min after injection started, show the displacement of brine by CO_2. Due to unfavorable mobility ratio, after CO_2 breakthrough a high remaining brine saturation is present in the core. After breakthrough of CO_2 the main drying mechanism is evaporation of water into the gaseous phase. After 15.5 h complete clogging of the injection well was observed (dark red color). This can be explained by combined continuous evaporation and capillary-driven backflow of brine towards the vicinity of the injection well.

The potential of formation clogging due to capillary-driven backflow depends strongly on the saturation gradient inside the porous medium. We analyze the situation at which capillary-driven backflow becomes dominant over viscous-driven flow with a 1D example (Figure 6.4). In the absence of gravity and compressibility, the velocity of the water phase can be described by the fractional flow formulation:

$$u_w = u_t f_w = u_t \frac{\lambda_w}{\lambda_w + \lambda_g}\left(1 + \frac{\lambda_g}{u_t}\frac{dP_c}{dS_w}\frac{\partial S_w}{\partial x}\right) \qquad (19)$$

where u_w is the Darcy velocity for water, f_w is the water fractional flow, u is the total velocity, $\lambda_g = Kk_{rg}/\mu_g$ is the gas mobility and $\lambda_w = Kk_{rw}/\mu_w$ is the water mobility, P_c is the capillary pressure and S_w is the aqueous phase (water/brine) saturation. The equation consists of a viscous flow term and a capillary flow term, where the derivative dP_c/dS_w is negative and the direction of brine flow is determined by the dominancy of either viscous or capillary-driven flow.

In Figure 6.4 the viscous flow velocity is represented by the dashed line and the capillary flow velocity is shown in solid black lines, for $\partial S_w/\partial x$ equal to: 0, 2, 4, 6, 8 m^{-1}. The highest value for $\partial S_w/\partial x$ is represented by the first solid line from the left. Less steep slopes of $\partial S_w/\partial x$ result in a lower capillary-driven flow velocity. The viscous flow velocity is constant for all cases. The red lines represent u_w, being the sum of the viscous flow velocity and the capillary flow velocity. The first red line from the top corresponds to the highest value for $\partial S_w/\partial x$. For experimental conditions, the capillary-driven term has the highest (negative) velocity for a water saturation of approximately 0.85. The unfavorable mobility ratio for brine displacement by CO_2 under experimental conditions stimulates the term for capillary-driven backflow at high water saturations. For comparison, we show the potential for backflow of brine under reservoir conditions, 45°C/100 bar. The ratio between gas and water mobility is lower and therefore the capillary-driven term becomes dominant at a lower water saturation. The viscous flow term is also affected by a lower mobility ratio so that the viscous velocity is higher for the same water saturation. The red lines show that at a certain water saturation, capillary-driven flow exceeds viscous flow, and backflow of brine toward the injection point occurs. For example, for $\partial S_w/\partial x$ = 8 m^{-1}, capillary-driven backflow dominates over viscous-driven flow below a water saturation of approximately 0.75 and 0.55 for experimental and reservoir conditions, respectively.

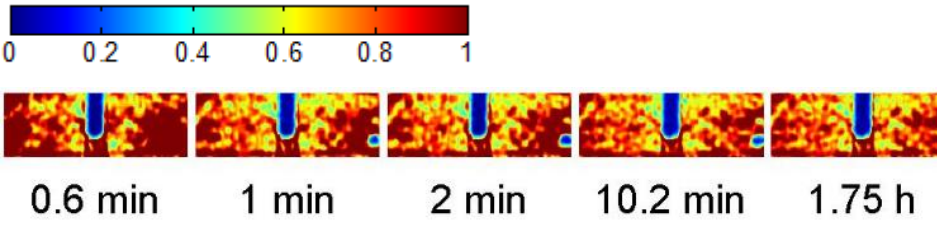

Figure 6.3. Brine saturation at different times obtained from CT scan imaging (Figure 5.10). The brine saturation represents both the presence of brine and solid salt. After 15.5 h of injection complete clogging of the injection well can be observed (dark red).

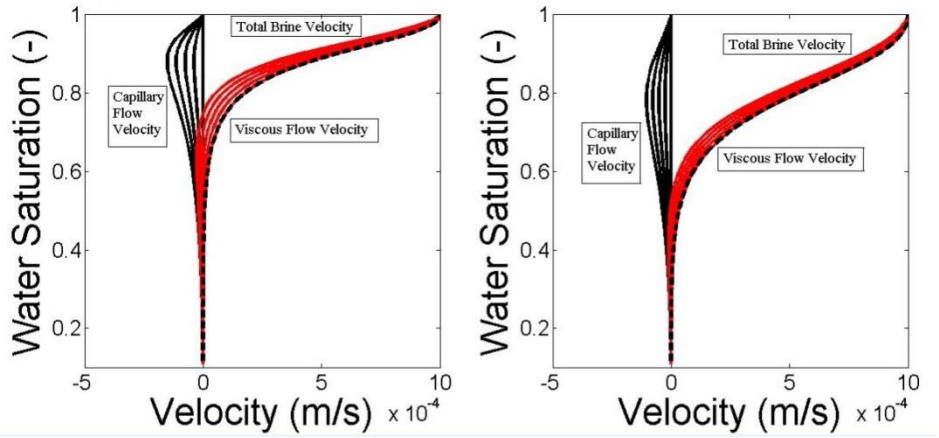

Figure 6.4. Comparison of viscous flow velocity and capillary flow velocity at (left) laboratory and (right) reservoir conditions. The total brine velocity, u_w, is represented by the red lines and consists of the sum of the viscous and capillary flow velocities. Capillary flow velocity is plotted vs. saturation for $\partial(S_w, x)$ varying from 1 (closest to the y-axis) to 8 (furthest from the y-axis) m^{-1}. Below a certain water saturation the value of the capillary flow velocity exceeds the viscous flow velocity and u_w becomes negative.

6.3.2. In-situ brine saturation redistribution during dry-out: long cores

Brine saturation distributions were calculated from the CT scans at various times during CO_2 injection into the Bentheimer sandstone core and the layered core consisting of Bentheimer (top) and Berea (bottom) as shown in Figure 6.5. The first scans from the left hand side which were taken at 1 min and 10 min after CO_2 injection started, show the remaining brine saturation after CO_2 breakthrough. The scans show that in both systems CO_2 initially does not propagate into the lower part of the cores. Especially in the layered system it is clearly visible that Berea layer does not get penetrated by CO_2 at all. This can be explained by the fact that Berea

has a higher entry capillary pressure than Bentheimer as can be seen from the P_c *vs.* S_w curves plotted in Figure 6.9. We shall return to this point in the Section 6.3.4 below. As injection continues, after approximately 98 hours, dry-out of the lower parts of the cores become visible and is more pronounced in the homogeneous Bentheimer system. At 142 hours, dry-out of the lower part of the Berea sandstone has become significant.

Solid salt could not be quantified directly from the CT scans, but the results indicate that salt precipitation takes place throughout the whole upper part in case of the Bentheimer core. Salt precipitation is observed only near the top in the layered system (dark red). For the latter system, the lower part of the Bentheimer layer seems to dry-out completely with brine saturations lower than 0.2 (dark blue). The physical mechanism responsible for the severe dry-out on the upper part is addressed in the next section. Complete clogging in the vicinity of the injection well as observed in previous work with a fully penetrating well in a short core did not take place (Figure 6.3).

To compare the saturation distribution inside the porous media we have averaged the values over the width of each slice and plotted against core height in Figure 6.6. The black line represents the brine saturation in the homogeneous core and the gray line represents the saturation in the layered core. After displacement and in the early stages of dry-out (the first four figures from the left) a comparable brine saturation was found in the upper part which both consist of Bentheimer. This shows that the composition of the core (homogeneous or layered) did not affect the displacement process. A difference in brine saturation between the two experiments can be observed at a height of 7-7.5 cm, with lower brine saturations in the homogeneous core and a fully saturated Berea layer in the layered core. Due to noise, a saturation that slightly exceeds 1 was found for the lower part of the cores.

The fifth scan shows how dry-out starts to affect the distribution of the brine saturation. For the homogeneous core we can observe a decrease in brine saturation below 6 cm height as the dry-out front propagates into the lower part. At this time, the bottom part of the layered system remains fully saturated with brine. The last scan in Figure 6.6 shows how the brine saturation in the Berea layer eventually decreases as well (gray line). The upper part has eventually reached sufficiently low brine saturation values so that capillary suction from the bottom part can start taking place.

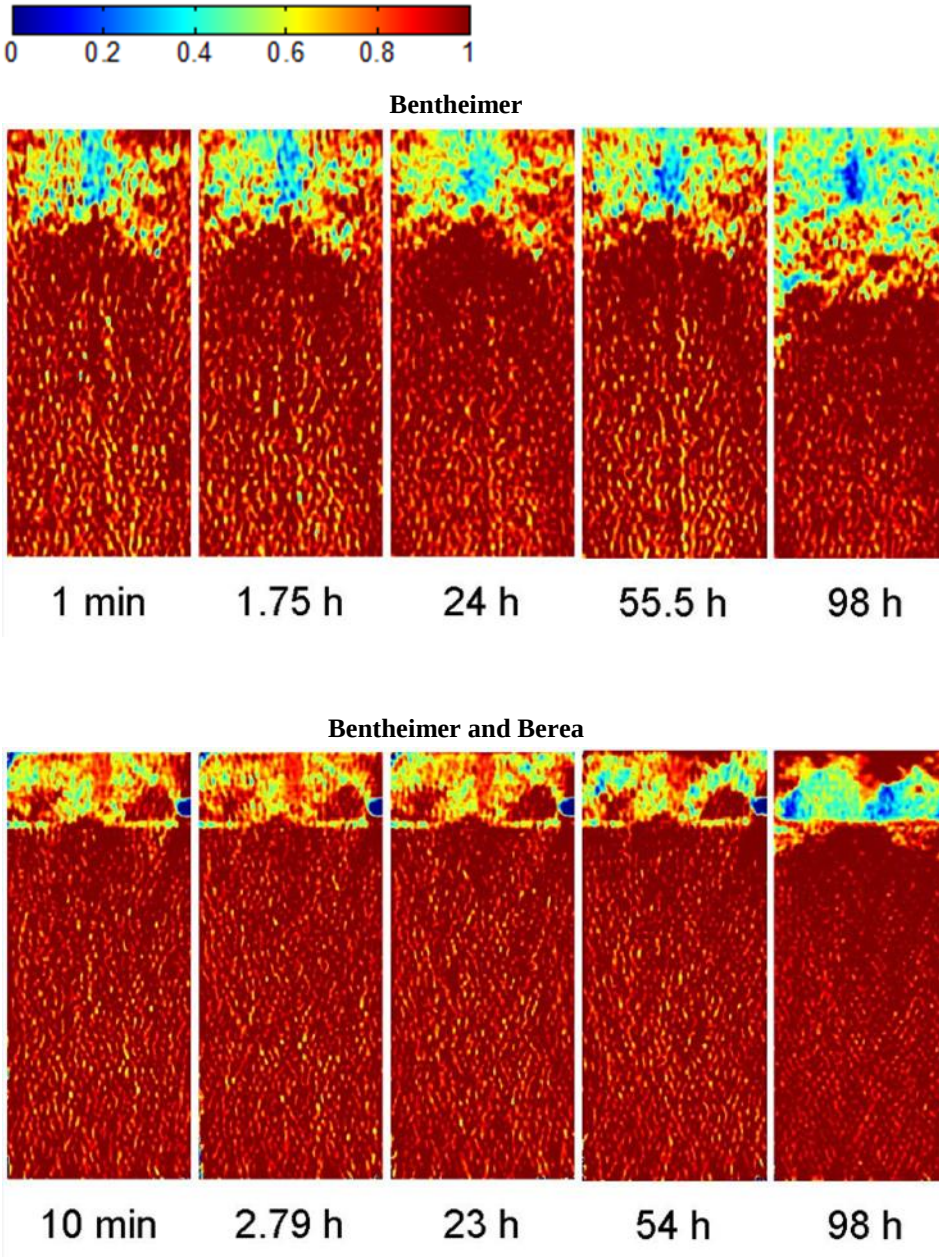

Figure 6.5. CT scan images at various times for (a) homogeneous Bentheimer core and (b) layered Bentheimer and Berea core.

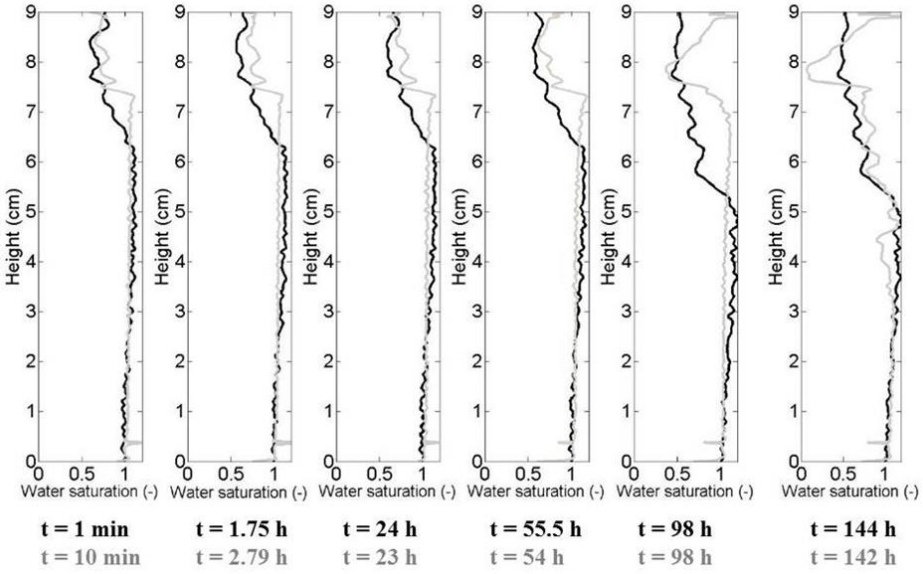

Figure 6.6. Brine saturation calculated from the CT scans and averaged over the width. The black line corresponds to the homogeneous core and the gray line to the layered core.

6.3.3. Visualization of solid salt by µ-CT scans

After the core-floods were terminated µ-CT scans were taken from the short core and the layered core in order to visualize solid salt inside the porous media. Figure 6.7 shows slices taken at a depth of 0.8 cm from the top of the cores. After reconstruction, the color map ranges on a grayscale from black to white with increasing density. Solid salt has a high density (3.1 g/cm^3) and is represented by white, CO_2 has a low density (0.0018 g/cm^3) and is shown in black and the porous medium has an intermediate density (2.6 g/cm^3) and is shown in gray. It was found by Van Hemert et al. (2013) that salt crystals tend to cover multiple connecting pore spaces and can therefore be clearly detected by the µ-CT scanner.

The images confirm that solid salt accumulated around the injection well inside the short Bentheimer core (Figure 6.7a). The light gray color in the outer part of the core shows pore spaces filled with brine. This means that the injection well was completely clogged before complete dry-out was reached. A different salt pattern was observed in the layered system (Figure 6.7b). Salt precipitated throughout the Bentheimer layer and reduced the available pore space dramatically.

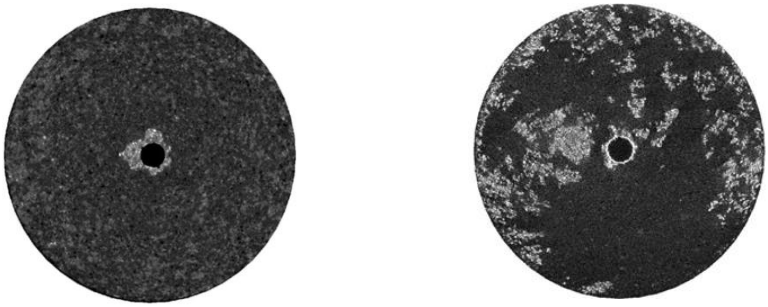

(a) (b)

Figure 6.7. Post experiment µ-CT scans taken at 0.8 cm from the top from (a) short Bentheimer core (Roels et al., 2015 and (b) layered core. White color represents higher density (solid salt) and black color represents lower density (CO_2). Solid salt was found (a) accumulated around the injection well and (b) distributed along the domain.

6.3.4. Capillary-driven flow directions in homogeneous and layered systems

Figure 6.8 shows a conceptual illustration of the brine flow regimes in the different cores resulting in different salt precipitation patterns. In the short core (Figure 6.8a), brine flow is directed toward the dry zone around the well and accumulation of salt leads to a relatively fast clogging of the porous medium in the vicinity of the injection well. For the homogenous core, the capillary curves for the upper layer (CO_2 displacement takes place) and for the lower layer (the source of brine for the upper layer) are similar (Figure 6.8b). For this reason capillary-driven flow of brine from the source will continuously redistribute the brine saturation so that the zone around the well remains wet. The slope of the $P_c(S_w)$-curve starts to increase as brine saturation decreases (Figure 6.9, dashed line) and capillary-driven forces become stronger. As a consequence, capillary-suction of brine towards the upper dry zone occurs. Therefore, the source of brine delays salt precipitation and retards its accumulation near the injection well.

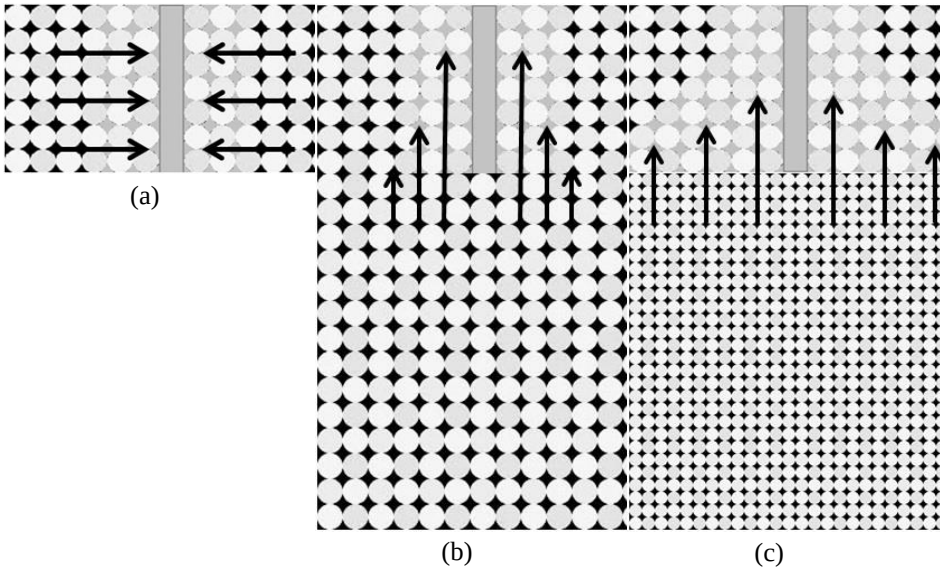

Figure 6.8. Conceptual illustration of capillary suction of brine toward the dry zone for (a) without brine source, (b) with homogeneous system and (c) layered system.

For the layered core, the capillary pressures for the upper layer (Bentheimer) are lower than those of the lower layer (Berea) at equal saturations as shown in Figure 6.9 with the parameters from Table 6.1. The brine saturation in the upper part decreases due to evaporation and as a result capillary pressure becomes higher. At a certain saturation, the capillary pressure equals the entry pressure of the lower region (arrow). As dry-out continues, the system will redistribute its fluids in such way that the difference in capillary pressure at the contact area is minimized. However, if the upper layer reaches complete dry-out at a capillary pressure that is lower than the pressure that needs to be overcome to redistribute the brine between the low and high permeable layer, the influence of additional salt precipitation will be minimal.

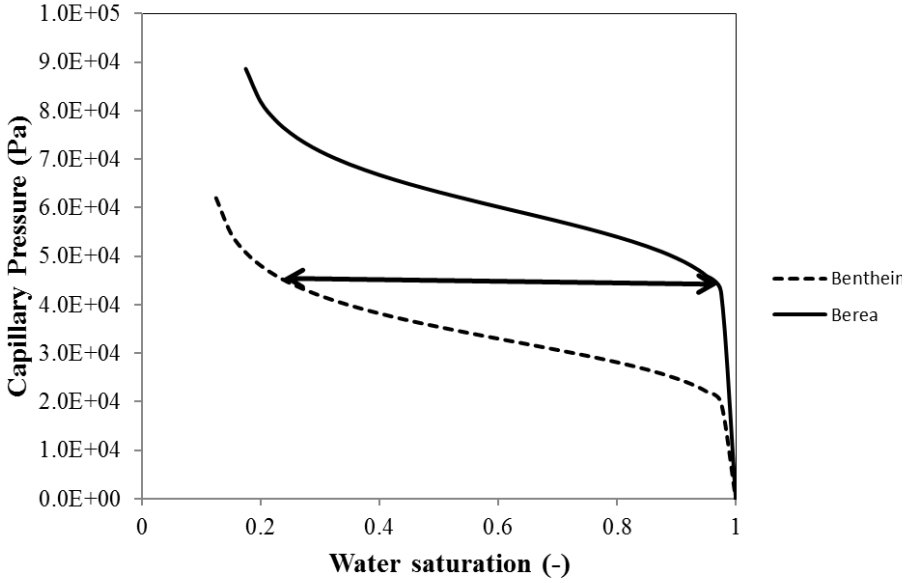

Figure 6.9. Capillary pressure-water saturation curves for Bentheimer (dashed line) and Berea (solid line). After sufficient dry-out fluid will be redistributed so that capillary pressure equilibrium is maintained between Bentheimer and Berea.

6.3.5. Effect of salt precipitation on pressure drop

The pressure drop between injection well and outlets measured during the experiments is shown in Figure 6.10. The dashed line shows the pressure drop from the experiment with the short radial core as shown in Figure 5.13, Chapter 5. In that experiment, the maximum safety pressure is reached within approximately 15 hours. The pressure drop during CO_2 injection into the long Bentheimer core is represented by the black line and the line with symbols shows the pressure drop in the layered core. All systems show an increase in pressure drop due to a decrease in matrix permeability caused by the precipitation of salt. The pressure drop increases gradually for systems in which a brine source was included at the bottom whereas in the absence of a brine source clogging occurred much faster.

The results indicate that the brine source delays salt precipitation by keeping the porous medium wet for a longer period of time. It was found in the CT scans that salt accumulated around the well in absence of a brine source, whereas more salt precipitation throughout the domain was found in presence of a brine source. This indicates that capillary driven flow towards the well, i.e. a brine saturation gradient created by evaporation, is stronger in the short core. The presence of a brine source prevents the establishment of a saturation gradient between injection well and outlet,

but rather establishes a gradient between upper and lower part of the cores. This is consistent with the conceptual model given in Figure 6.8.

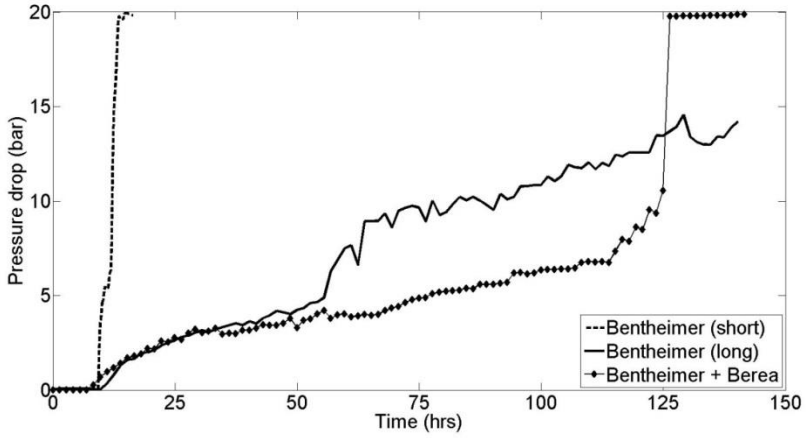

Figure 6.10. Pressure drop vs. time for three experiments. The dashed line represents the short Bentheimer core (Figure 5.13), the black line represents the long Bentheimer core and the line with symbols represents the layered core of Bentheimer and Berea. Salt precipitation lead to an increase in injection pressure in all cases.

6.3.6. Implications for field scale injection

An important factor that influences the amount of pore volume that will be blocked by the precipitation of solid salt is the amount of dissolved salt available in the brine after displacement. In case of KI-solution, which has a high solubility limit, the concentration of dissolved salt is high and therefore a significant impact on permeability impairment can be expected. A brine solution with smaller concentration of dissolved salt, as well as solutions with types of salt with lower solubility limit (e.g. NaCl-solutions and formation brine) will show similar precipitation patterns but with smaller volume of occupied pore space, and therefore a smaller impact in pressure drop.

On the other hand, the amount of brine available for capillary-driven flow in the experiments is limited whereas under field conditions the source of brine is 'unlimited'. The brine source in the injection layer as well as in the less permeable confining layer(s) could provide flow of brine toward the injection well until complete clogging has been reached. In contrast, in Figure 4, we showed that the potential for backflow of brine under reservoir conditions, 45°C/100 bar, is lower than under current experimental conditions. Under reservoir conditions, the ratio between gas and water mobility is lower and therefore the capillary-driven term is

less pronounced. However, field scale scenarios have been studied numerically (e.g. Giorgis et al., 2007; Muller et al., 2009; Peysson et al., 2014) and have shown that under resevoir conditions, capillary-driven backflow can be strong enough to cause severe injection impairment due to formation clogging in the vicinity of the well.

6.4. Conclusions

CO_2 core-flood experiments were performed to investigate the effect of a brine source on permeability impairment in radial geometry. Three cases were considered: (a) a short Bentheimer core perforated through its axis (from previous study), (b) a long cylindrical homogenous (Bentheimer) core perforated over the same height as the short core (c) an long layered core formed by superimposing a short perforated Bentheimer section and Berea section so that total length is equal to that in (b). CT scans were taken to quantify the saturation distributions inside the porous medium at various times during dry-out. The effect of salt precipitation on injectivity was measured by monitoring the pressure drop over the core while injecting CO_2.

Experimental evidence indicates that formation clogging due to salt precipitation during CO_2 injection may cause significant impact on injection pressures. It was found that capillary rise from a brine source toward the drying zone retards complete impairment injectivity by keeping the porous medium wet. However, continuous transport of brine to the injection zone eventually decreases the permeability of the porous medium dramatically and injection pressure rises.

For the layered case, it was found that capillary suction into the coarse layer starts when the layer is sufficiently dry. Tendency towards equilibrium in capillary pressure between the two layers leads to a continuous redistribution of brine inside the layered system. Transport of brine from the fine-textured layer can contribute to accumulation of salt and severe clogging of the injection layer. Current study shows that formation clogging due to salt precipitation during CO_2 injection can be underestimated when connected layers are not taken into account.

Acknowledgments

This research was done as part of CATO 2, the Dutch National Program for CCS. The authors are grateful for the Dutch Ministry of Economic Affairs and the sponsoring companies for funding. We would like to thank Marc Friebel, Dirk Delforterie and Ellen Meijvogel-de Koning, technical staff of our laboratory, for their help with conducting the experiments.

Bibliography

Akin, S., Kovscek, A., 2003. Computed tomography in petroleum engineering research. Geological Society, London, Special Publications 215, 23-38.

Alkan, H., Cinar, Y., Ülker, E., 2010. Impact of capillary pressure, salinity and in situ conditions on CO2 injection into saline aquifers. Transport in porous media 84, 799-819.

André, L., Peysson, Y., Azaroual, M., 2014. Well injectivity during CO2 storage operations in deep saline aquifers–Part 2: Numerical simulations of drying, salt deposit mechanisms and role of capillary forces. International Journal of Greenhouse Gas Control 22, 301-312.

Bacci, G., Korre, A., Durucan, S., 2011. Experimental investigation into salt precipitation during CO2 injection in saline aquifers. Energy Procedia 4, 4450-4456.

Feldkamp, L., Davis, L., Kress, J., 1984. Practical cone-beam algorithm. JOSA A 1, 612-619.

Giorgis, T., Carpita, M., Battistelli, A., 2007. 2D modeling of salt precipitation during the injection of dry CO2 in a depleted gas reservoir. Energy Conversion and Management 48, 1816-1826.

Hosa, A., Esentia, M., Stewart, J., Haszeldine, S., 2011. Injection of CO2 into saline formations: Benchmarking worldwide projects. Chemical Engineering Research and Design 89, 1855-1864.

Hurter, S., Berge, J.G., Labregere, D., 2007. Simulations for CO2 injection projects with compositional simulator. Offshore Europe.

Lehmann, P., Assouline, S., Or, D., 2008. Characteristic lengths affecting evaporative drying of porous media. Physical Review E 77, 056309.

Muller, N., Qi, R., Mackie, E., Pruess, K., Blunt, M.J., 2009. CO2 injection impairment due to halite precipitation. Energy procedia 1, 3507-3514.

Nachshon, U., Weisbrod, N., Dragila, M.I., Grader, A., 2011. Combined evaporation and salt precipitation in homogeneous and heterogeneous porous media. Water Resources Research 47.

Niessner, J., Hassanizadeh, S.M., 2009. Modeling Kinetic Interphase Mass Transfer for Two-Phase Flow in Porous Media Including Fluid–Fluid Interfacial Area. Transport in porous media 80, 329-344.

Ott, H., de Kloe, K., Marcelis, F., Makurat, A., 2011. Injection of supercritical CO2 in brine saturated sandstone: Pattern formation during salt precipitation. Energy Procedia 4, 4425-4432.

Ott, H., Snippe, J., de Kloe, K., Husain, H., Abri, A., 2013. Salt Precipitation Due to Sc-gas Injection: Single Versus Multi-porosity Rocks. Energy Procedia 37, 3319-3330.

Peysson, Y., 2012. Permeability alteration induced by drying of brines in porous media. The European Physical Journal Applied Physics 60, 24206.

Peysson, Y., Andre, L., Azaroual, M., 2014. Well injectivity during CO2 storage operations in deep saline aquifers—Part 1: Experimental investigation of drying effects, salt precipitation and capillary forces. international journal of Greenhouse Gas Control 22, 291-300.

Pruess, K., Müller, N., 2009. Formation dry-out from CO2 injection into saline aquifers: 1. Effects of solids precipitation and their mitigation. Water Resources Research 45, W03402.

Roels, S.M., Ott, H., Zitha, P.L., 2014. μ-CT analysis and numerical simulation of drying effects of CO2 injection into brine-saturated porous media. International Journal of Greenhouse Gas Control 27, 146-154.

Roels, S.M., Nicolaides, C., Zitha, P.L.J., 2015. Effect of capillary-driven backflow on salt precipitation due to CO_2 injection into brine-saturated porous media. Accepted with revisions in Water Resources Research.

Schroth, M.H., Istok, J.D., Selker, J.S., 1998. Three-phase immiscible fluid movement in the vicinity of textural interfaces. Journal of Contaminant Hydrology 32, 1-23.

Shokri, N., Lehmann, P., Or, D., 2010. Evaporation from layered porous media. Journal of Geophysical Research: Solid Earth (1978–2012) 115.

Simjoo, M., Nguyen, Q.P., Zitha, P.L.J., 2012. Rheological Transition during Foam Flow in Porous Media. Industrial & Engineering Chemistry Research 51, 10225-10231.

Spycher, N., Pruess, K., 2005. CO2-H2O mixtures in the geological sequestration of CO2. II. Partitioning in chloride brines at 12–100° C and up to 600 bar. Geochimica et Cosmochimica Acta 69, 3309-3320.

Spycher, N., Pruess, K., 2010. A phase-partitioning model for CO2–brine mixtures at elevated temperatures and pressures: application to CO2-enhanced geothermal systems. Transport in porous media 82, 173-196.

Van Hemert, P., Rudolph, E.S.J., Zitha, P.L., 2013. Micro Computer Tomography Study of Potassium Iodide Precipitation in Bentheimer Sandstone Caused by Flow-through CO2 Drying. Energy Procedia 37, 3331-3346.

Zuluaga, E., Muñoz, N., Obando, G., 2001. An Experimental study to evaluate water vaporisation and formation damage caused by dry gas flow through porous media, International Symposium on Oilfield Scale. Society of Petroleum Engineers.

7

General discussion

This work provides a better understanding of the main processes involved in underground CO_2 storage into saline aquifers. The key processes which may take place during CO_2 injection into a brine-saturated porous medium include displacement of brine by CO_2, capillary forces, evaporation of water into CO_2, dissolution of CO_2 into brine and salt precipitation. Their combined effects can under certain circumstances lead to severe injectivity decline. Indeed, evaporation of formation water into the injected CO_2 (formation dry-out) induces an increase in dissolved salt concentration, eventually leading to salt precipitation. The ensuing impairment of permeability has serious consequences for CO_2 storage operations as it reduces injection capacity, i.e. how much CO_2 can be injected per unit time, and results in a lower storage capacity, i.e. the amount of CO_2 which can ultimately be stored. In this study, we have used a combination of modeling, numerical simulations and laboratory experiments in order to obtain an insight into the above effects. The following paragraphs present a review of the main results from a broader perspective.

We have studied the effect of salt precipitation and subsequent injectivity impairment by injection of CO_2 injection into brine-saturated sandstone core samples. During CO_2 injection three (counteracting) processes affect the pressure drop:

(1) Precipitation of salt in the pore space decreases the rock permeability and therefore increases the pressure drop. The relation between salt precipitation and permeability has been studied directly by Bacci et al. (2011) and Peysson (2012) after complete dry-out of the core samples. The results are useful for parameterization of the $K - \varphi$ relationship. In this work we used the "tubes in series" model by Verma and Pruess (1988b), which allows permeability reduction to zero for a certain fraction of pore space blocked.

(2) Capillary-driven backflow of brine toward the dry zone near the injection point causes salt to accumulate and increases the pressure drop. This was found previously in several numerical studies (e.g. Giorgis et al., 2007; Muller et al., 2009; Pruess and Müller, 2009b) and is confirmed experimentally in this work and other recent studies (Ott et al., 2011; Peysson et al., 2014).

(3) An increase in CO_2 relative permeability due to an increase in CO_2 saturation decreases the pressure drop (Ott et al., 2011).

For the first set of experiments (Chapter 3 and 4), we used homogeneous cores of certain diameter and length, with injection forced into a quasi-1D flow direction along the length of the core. We found that in 1D injection samples the increase in

CO_2 relative permeability was able to compensate for the decrease in rock permeability caused by salt precipitation and accumulation. During CO_2 injection, the pressure drop (and by extension injection pressure) gradually decreased over time. Numerical simulations showed that a weak capillary-driven backflow did not bring sufficient salt to the vicinity of the injection point in order to impair injectivity. This work showed that when viscous forces dominate over capillary forces (i.e. in case of a high injection rate), capillary-driven backflow is weak and salt precipitates uniformly over the length of the porous medium resulting in an increase in injectivity. The results follow the concept of a threshold injection rate above which capillary-driven backflow may not play a role, as proposed by Ott et al. (2011) and André et al. (2014). Capillary backflow is driven by a gradient in brine saturation inside the porous medium. This gradient is established by evaporation of water into the CO_2 and is steeper for higher evaporation rates at a given flow rate. We found that evaporation (phase partitioning between CO_2 and brine) should be described by a kinetic model for typical injection rates. In the numerical simulations, evaporation was described in two ways: (1) local equilibrium assumption (LEA) and (2) kinetic phase partitioning. It was found that LEA leads to an overestimated prediction of clogging at the inlet due to an overestimated capillary-driven backflow. By using a kinetic model for the CO_2 and brine phase partitioning the predicted profiles were more compatible with the measured ones. Another possible explanation for the absence of injectivity decline in the case of 1D flooding, is that a critical number of pores did not become blocked by solid salt (Lehmann et al., 2008; Nachshon et al., 2011). The theory on essential pores for flow would benefit from three-dimensional reconstructions of CT-scan data and the visualization of pore-bodies and throats. The exact location of solid salt (pore bodies or throats) could be related to rock permeability and an accurate porosity-permeability relation for salt precipitation during CO_2 injection could be developed.

Because of the crucial effect of flow velocity on salt accumulation and injectivity, we performed a second series of experiments of CO_2 injection into brine-saturated *radial* domains (Chapter 5). 1D flow regimes do not take into account the significant decrease in flow velocities which occurs when radial injection takes place. To the best of our knowledge, this experimental work is completely new. The results show that in the radial injection domain salt accumulates near the injection well and injectivity decreases dramatically. Due to capillary-driven backflow salt accumulated in the vicinity of the well until complete clogging occurred. Numerical modelling showed that the spatial difference in salt precipitation between the radial and 1D domain is caused by a difference in velocity field. The efficiency of evaporation determines the rate of uptake of water vapor into the CO_2 stream and hence whether a gradient in brine saturation will occur in the domain. At high

injection velocity the evaporation rate is low compared to the flow rate so that CO_2 does not become saturated with water vapor and evaporation occurs throughout the whole domain. No gradient in brine saturation is established and therefore no capillary-driven backflow and salt accumulation occur. However, in the radial domain the flow velocity decreases with increasing distance from the injection well, enabling a more efficient evaporation and the establishment of a brine saturation gradient. This causes a continuous transport of dissolved salt toward the drying zone and subsequent precipitation. As evaporation continues solid salt accumulates near the inlet until complete clogging occurs, i.e. injectivity approaches zero. The work shows that one should be cautious when drawing conclusions in velocity-dependent systems. This recommendation applies also to other subsurface flow phenomena studied in laboratory research, such as polymer or foam flow where non-Newtonian behavior can be expected.

The third series of injection domains addressed in current work comprised radial injection experiments with a connected brine source (Chapter 6). The brine source was located in a porous medium with equal or higher water retention properties. It was reported earlier by Schroth et al. (1998a) and Shokri et al. (2010) that water redistribution between fine and coarse layers occurs after a capillary pressure jump has been overcome. We performed the flooding experiments in order to investigate whether this phenomena contributes to injectivity decline in case dissolved salt is taken into account. The results show that capillary suction from the brine source into the injection layer starts when the layer is sufficiently dry. Tendency towards equilibrium in capillary pressure between the two layers leads to a continuous redistribution of brine inside the layered system leading to severe clogging of the injection layer. This study shows that formation clogging due to salt precipitation during CO_2 injection can be underestimated when connected layers are not taken into account.

In this work, simulation and experimental results were compared qualitatively rather than quantitatively. The mathematical description of dry-out and the effect of salt precipitation on constitutive relations as well as the values of many parameters involved (e.g. porosity-permeability relation, mass transfer rate) are not studied independently and contain assumptions. For instance, using a simplified evaporation description (constant evaporation coefficient) an accurate pressure drop prediction could not be obtained. However, using a more detailed description of evaporation (e.g. including interfacial area) would require additional information on parameter values, which are difficult to obtain. The results indicate that the complexity of the evaporation process cannot be captured by the constant evaporation rate as applied in our model. A more accurate formulation of the dependence of evaporation on, e.g.

interfacial area and injection velocity, should be developed in future studies. Feedback loops and dependencies on evaporation were not taken into account when deriving the evaporation rate and using it in our numerical simulations. Also, constitutive relations such as the dependence of relative permeability and capillary pressure on water saturation do not take the effect of salt precipitation into account. An increase in adjustable parameters would probably allow us to make a better fit with the experimental results but it would not increase the reliability of our model. For more accurate simulation results, a more detailed parameter study is required.

Bibliography

André, L., Peysson, Y., Azaroual, M., 2014. Well injectivity during CO2 storage operations in deep saline aquifers–Part 2: Numerical simulations of drying, salt deposit mechanisms and role of capillary forces. International Journal of Greenhouse Gas Control 22, 301-312.

Bacci, G., Korre, A., Durucan, S., 2011. Experimental investigation into salt precipitation during CO2 injection in saline aquifers. Energy Procedia 4, 4450-4456.

Giorgis, T., Carpita, M., Battistelli, A., 2007. 2D modeling of salt precipitation during the injection of dry CO2 in a depleted gas reservoir. Energy Conversion and Management 48, 1816-1826.

Lehmann, P., Assouline, S., Or, D., 2008. Characteristic lengths affecting evaporative drying of porous media. Physical Review E 77, 056309.

Muller, N., Qi, R., Mackie, E., Pruess, K., Blunt, M.J., 2009. CO2 injection impairment due to halite precipitation. Energy procedia 1, 3507-3514.

Nachshon, U., Weisbrod, N., Dragila, M.I., Grader, A., 2011. Combined evaporation and salt precipitation in homogeneous and heterogeneous porous media. Water Resources Research 47.

Ott, H., de Kloe, K., Marcelis, F., Makurat, A., 2011. Injection of supercritical CO2 in brine saturated sandstone: Pattern formation during salt precipitation. Energy Procedia 4, 4425-4432.

Peysson, Y., 2012. Permeability alteration induced by drying of brines in porous media. The European Physical Journal Applied Physics 60, 24206.

Peysson, Y., Andre, L., Azaroual, M., 2014. Well injectivity during CO2 storage operations in deep saline aquifers—Part 1: Experimental investigation of drying effects, salt precipitation and capillary forces. international journal of Greenhouse Gas Control 22, 291-300.

Pruess, K., Müller, N., 2009. Formation dry-out from CO2 injection into saline aquifers: 1. Effects of solids precipitation and their mitigation. Water Resources Research 45.

Schroth, M.H., Istok, J.D., Selker, J.S., 1998. Three-phase immiscible fluid movement in the vicinity of textural interfaces. Journal of contaminant hydrology 32, 1-23.

Shokri, N., Lehmann, P., Or, D., 2010. Evaporation from layered porous media. Journal of Geophysical Research: Solid Earth (1978–2012) 115.

Verma, A., Pruess, K., 1988. Thermohydrological conditions and silica redistribution near high-level nuclear wastes emplaced in saturated geological formations. Journal of Geophysical Research: Solid Earth (1978–2012) 93, 1159-1173.

Summary

Accumulation of CO_2 in the atmosphere is an important factor in the contribution to global warming. As most of the atmospheric CO_2 increase is attributed to anthropogenic activities, society as a whole must act to mitigate this development. One of the most widely discussed options for reducing CO_2 emissions is referred to as *carbon dioxide capture and storage* (CCS). This technique concerns the capture and purification of CO_2 emissions from fossil-fuel power plants, subsequent compression and transport, and ultimately the storage of CO_2 in deep geological formations. Three main types of sites for subsurface CO_2 storage have been discussed widely: saline aquifers, depleted oil and gas reservoirs, and coal beds. It has become the favored option to store CO_2 in saline aquifers, due to their potential of high storage capacities. However, a major challenge related to CO_2 storage in saline aquifers is the risk of formation clogging due to salt precipitation which will strongly reduce the storage capacity of the aquifer. This research aims at understanding the conditions that lead to impairment in injectivity due to salt precipitation. A general introduction into the topic and the motivation for this research are described in **Chapter 1**.

Formation clogging during CO_2 injection caused by precipitation of salt can decrease storage potential substantially. Reduced storage capacity can occur by (1) a decrease in available pore space caused by the presence of solid salt and (2) complete clogging of the porous medium in the vicinity of the injection well by solid salt accumulation. Water and CO_2, either in gaseous or supercritical state, are mutually soluble. As CO_2 is injected into a saline aquifer it will therefore eventually vaporize water of the resident brine phase. This will lead to super-saturation of the brine and consequently precipitation of salt in the porous medium, also known as *sub-florescence*, which reduces formation porosity and possibly permeability. When brine saturation decreases due to evaporation, capillary forces increase and act as a driving force for brine to flow from higher saturations toward dryer zones. As long as the liquid is connected to the bulk phase, advective transport of dissolved salt is possible and may lead to salt accumulation near the well, which may result in a dramatic decrease in injectivity. A mathematical overview of the equations used to describe the processes involved in CO_2 sequestration is presented in **Chapter 2**.

In **Chapter 3**, CO_2 injection in brine-saturated Bentheimer sandstone was studied experimentally to visualize and quantify salt precipitation in porous rock caused by evaporation of water into injected gaseous phase CO_2. Gas and solid-salt saturation profiles were captured by μ-CT (micro computed tomography) and the pressure drop over the core was monitored continuously. The experimental results were compared with numerical simulations using the TOUGH2 reservoir simulator with the

equation of state module ECO2N, and a numerical code that we have developed with an alternative approach on evaporation. Using the equilibrium phase partitioning model in TOUGH2, simulation results predict injectivity decline due to an accumulation of precipitated salt near the core inlet. This is in contradiction to our experimental observations, in which neither salt accumulation nor injectivity impairment was noticed. It appears that at near well injection velocities, local equilibrium phase partitioning used in the simulator overestimates evaporation of water into the CO_2 gaseous phase. On the other hand, satisfying results were obtained from our model which uses a kinetic formulation for the evaporation. No injectivity impairment was found which is compatible with the experimental results.

In **Chapter 4** we investigated the consequences of supercritical CO_2 injection in sandstones. By injecting dry supercritical CO_2 into brine-saturated sandstone, we investigate the drying process and the associated precipitation of salts in a capillary-pressure-dominated flow regime. Precipitation patterns were recorded during the drying process by means of μ-CT scanning. The experimental results and numerical simulations show that under a critical flow rate salt precipitates with an inhomogeneous spatial distribution because of brine and solutes being transported in counter-current flow upstream where salt eventually precipitates. A substantial impairment of the absolute permeability has been found, but despite high local salt accumulation, the effective CO_2 permeability increased during all experiments. This phenomenon is a result of the observed microscopic precipitation pattern and eventually the resulting K-ϕ-relationship. The findings in this paper are related to unimodal sandstone.

CO_2 injection into linear and radial brine-saturated porous media was investigated both by numerical analysis and CT scan aided core-flood experiments and presented in **Chapter 5**. We found that the potential of formation clogging due to salt precipitation depends strongly on the velocity field inside the porous medium. In linear flows, complete impairment of injectivity occurred only for low injection rates where water evaporation induced steep brine saturation gradients in the porous medium. For radial flows, however, impairment of injectivity occurred regardless of whether the injection velocity was low or high. Capillary-driven backflow of brine resulted in accumulation of salt near the injection well. In linear flows, capillary-driven backflow is supressed at high injection velocities. In radial flows, instead, capillary-driven backflow of brine is always possible since the flow velocity decreases with increasing distance from the well.

Chapter 6 investigates the contribution of continuous transport of dissolved salt toward the dry zone around the injection well by capillary-driven flow of brine from a brine source. In this study, core flooding experiments were performed in homogeneous coarse textured cores and in layered cores consisting of a coarse textured layer overlying a fine textured layer. CO_2 was injected through a well in the

upper part of the cores and the bottom parts functioned as brine sources. Impairment in injectivity was found due to accumulation of precipitated salt caused by capillary-driven flow from the brine sources to the upper dryer region. Compared to flow domains without a brine source, we found that capillary-driven upward flow at first prevents complete clogging because the porous medium remains wet, but eventually leads to a more severe clogging of the entire domain. The results show that after sufficient dry-out, a coarse textured injection layer can draw brine from an underlying a fine textured layer by capillary forces. A connected fine textured layer can therefore contribute to salt precipitation and formation clogging of the injection layer.

The performed experimental and numerical work show that formation clogging can be a substantial risk during underground storage of CO_2. **Chapter 7** discusses the main findings of this research. The location of salt precipitation inside the porous medium depends strongly on the velocity field inside the domain and has a major effect on whether injectivity problems will occur. Capillary-driven backflow becomes dominant over viscous-driven flow in case of steep brine saturation gradients inside the domain and salt accumulation near the injection point can be expected. Formation clogging was found to be more likely to occur when low CO_2 injection rates are applied. In addition, transport of brine from fine-textured layers which should act as confining layers, can contribute to accumulation of salt and severe clogging of the coarse textured injection layer.

Samenvatting

Ophoping van CO_2 in de atmosfeer vormt een belangrijke factor in de bijdrage aan de opwarming van de aarde. Aangezien het grootste deel van de toename in atmosferische CO_2 wordt toegeschreven aan antropogene activiteiten, moet de samenleving als geheel handelen om deze ontwikkeling te beperken. Een van de meest besproken opties voor het verminderen van de CO_2-uitstoot wordt aangeduid als kooldioxide-afvang en -opslag (CCS). Deze techniek heeft betrekking op de afvang en zuivering van CO_2-uitstoot van fossiele brandstoffen uit krachtcentrales, daaropvolgende compressie en transport, en uiteindelijk de opslag van CO_2 in diepe geologische formaties. Drie belangrijke types van locaties voor ondergrondse CO_2-opslag zijn besproken op grote schaal: zoute aquifers, uitgeputte olie- en gasreservoirs en kolenlagen. Momenteel gaat de voorkeur voor opslag van CO_2 uit naar zoute aquifers, vanwege de potentieel hoge opslagcapaciteit. Echter, een belangrijke uitdaging met betrekking tot CO_2 opslag in zoute aquifers is het risico van verstopping van de formatie door zoutneerslag dat de opslagcapaciteit van de aquifer sterk zal verminderen. Dit onderzoek richt zich op het begrijpen van de omstandigheden die leiden tot afname in injectiviteit door zoutneerslag. Een algemene inleiding in het onderwerp en de motivatie voor dit onderzoek zijn beschreven in **Hoofdstuk 1**.

Verstopping van de formatie tijdens de injectie van CO_2, veroorzaakt door het neerslaan van zout, kan opslag potentieel aanzienlijk verlagen. Verminderde opslagcapaciteit kan plaatsvinden door (1) een vermindering van beschikbare poriënruimte veroorzaakt door de aanwezigheid van zout en (2) een volledige verstopping van het poreuze medium in de nabijheid van de injectieput door zout accumulatie. Water en CO_2, hetzij in gasvormige of superkritische toestand, zijn onderling oplosbaar. Als CO_2 wordt geïnjecteerd in een aquifer zal het water van de aanwezige waterfase verdampen. Dit zal leiden tot oververzadiging van het zoutwater en derhalve precipitatie van het zout in het poreuze medium, genaamd sub-fluorescentie, wat de porositeit en permeabiliteit mogelijk vermindert. Wanneer de zoutwater verzadiging afneemt als gevolg van verdamping, verhogen de capillaire krachten en fungeren als een drijvende kracht om het zoutwater te laten stromen van een hogere verzadiging richting droger zones. Zolang de vloeistof is verbonden met de bulk fase is advectief transport van opgeloste zouten mogelijk wat kan leiden tot zoutophoping nabij de put, wat kan resulteren in een dramatische afname van de injectiviteit. Een wiskundig overzicht van de vergelijkingen om de CO_2 opslag processen te beschrijven is opgenomen in **Hoofdstuk 2**.

In **Hoofdstuk 3** werd de injectie van CO_2 in Bentheimer zandsteen verzadigd met zoutwater bestudeerd met betrekking tot het visualiseren en kwantificeren van

zoutneerslag in poreus gesteente als gevolg van verdamping van water in de geïnjecteerde gasvormige fase CO_2. Gas en zout verzadiging profielen werden geregistreerd door μ-CT (micro computertomografie) en de drukval over de kern werd continu gemonitord. De experimentele resultaten werden vergeleken met numerieke simulaties met behulp van de TOUGH2 reservoir simulator met de toestandsvergelijking module ECO2N, en een numerieke code die we hebben ontwikkeld met een alternatieve beschrijving voor verdamping. Het lokaal evenwicht faseverdeling model in TOUGH2 voorspelde daling in injectiviteit te wijten aan een opeenstapeling van neergeslagen zout in de buurt van het injectiepunt. Dit is in tegenspraak met onze experimentele waarnemingen, waarin noch zoutophoping noch afname in injectiviteit werden opgemerkt. Het blijkt dat bij injectie snelheden die dichtbij de put voorkomen, de aanname van lokaal evenwicht in de faseverdeling verdamping van water in de CO_2 gasfase overschat. Aan de andere kant werden bevredigende resultaten verkregen met het model waarbij een kinetische formulering voor de verdamping werd toegepast. Geen afname in injectiviteit werd gevonden, wat verenigbaar is met de experimentele resultaten.

In **Hoofdstuk 4** onderzochten we de gevolgen van superkritische CO_2-injectie in zandsteen. Door het injecteren van droog superkritisch CO_2 in een zandsteen verzadigd met zoutwater, onderzoeken we het droogproces en de bijbehorende neerslag van zouten in een capillaire druk gedomineerde stroming. Neerslag patronen werden opgenomen tijdens het droogproces middels μ-CT scan. De experimentele resultaten en numerieke simulaties laten zien dat onder een kritiek debiet zout neerslaat met een inhomogene ruimtelijke verdeling omdat het water en de daarin opgeloste zouten stroomopwaarts worden vervoerd waar zout uiteindelijk neerslaat. Alhoewel een aanzienlijke afname van de absolute permeabiliteit is gevonden, is ondanks de hoge lokale zoutophoping de effectieve CO_2 permeabiliteit verhoogd tijdens alle experimenten. Dit verschijnsel is een gevolg van het waargenomen microscopische precipitatiepatroon en tenslotte de resulterende K (φ) relatie. De bevindingen in dit document zijn gerelateerd aan unimodale zandsteen.

CO_2 injectie in lineaire en radiale poreuze media verzadigd met zoutwater werd zowel met numerieke analyse als met kernstroming experimenten in de CT scanner onderzocht en gepresenteerd in **Hoofdstuk 5**. De resultaten lieten zien dat het potentieel van verstopping van de formatie door zoutprecipitatie sterk afhankelijk is van het snelheidsveld in het poreuze medium. In de lineaire injectie experimenten was er alleen volledige afwaardering van injectiviteit voor lage injectie snelheden doordat water verdamping een steile verzadiging gradiënt in zoutwater veroorzaakte in het poreuze medium. In de radiale injectie experimenten trad verminderde injectiviteit echter op ongeacht of de injectie snelheid laag of hoog was. Capillair-gedreven terugstroming van zouwater resulteerde in ophoping van zout in de buurt van het injectiepunt. In de lineaire poreuze media wordt capillair-gedreven

terugstroom onderdrukt bij hoge injectie snelheden. In radiale stromen, is capillair-gedreven terugstroming van zoutwater altijd mogelijk omdat de stroomsnelheid afneemt met toenemende afstand tot de bron.

Hoofdstuk 6 onderzoekt de bijdrage van het continue transport van opgelost zout naar de droge zone rond het injectiepunt door capillair-gedreven stroom van zoutwater vanuit een pekel bron. In deze studie werden kernstroming experimenten uitgevoerd in homogene grove kernen en in gelaagde kernen bestaande uit een laag met grove textuur die ligt op een laag van een fijne textuur. CO_2 werd geïnjecteerd door een put in het bovenste deel van de kernen en de bodemdelen functioneerden als pekel bronnen. Afname in injectiviteit werd gevonden wat werd veroorzaakt door ophoping van neergeslagen zout door capillair-gedreven stroming uit de pekel bronnen naar de bovenste drogere regio. Vergeleken met domeinen zonder pekel bron, vonden we dat capillair aangedreven opwaartse stroming eerst volledige verstopping voorkomt omdat het poreuze medium nat blijft, maar uiteindelijk leidt tot een ernstige verstopping van het gehele domein. De resultaten tonen aan dat na voldoende droogte, een grove structuur injectie laag pekel kan putten uit een onderliggende fijne textuur laag door capillaire krachten. Een aangesloten fijne textuur laag kan daarom bijdragen aan zout neerslag en verstopping van de injectie laag.

Het uitgevoerde experimentele en numerieke werk laat zien dat verstopping van het poreuze medium een aanzienlijk risico kan zijn voor de ondergrondse opslag van CO_2. **Hoofdstuk 7** bespreekt de belangrijkste bevindingen van dit onderzoek. De locatie van zoutprecipitatie binnen het poreuze medium blijkt sterk afhankelijk te zijn van het snelheidsveld in het domein en heeft een groot effect op de mate van problemen in injectiviteit. Capillair-gedreven terugstroming wordt dominant over viskeuze aangedreven stroming bij steile zoutwater verzadiging gradiënten binnen het domein in welke geval zoutophoping nabij het injectiepunt kan worden verwacht. De resultaten laten zien dat het risico op verstopping van het poreuze medium hoger is wanneer lage CO_2-injectie snelheden worden toegepast. Bovendien kan het transport van zoutwater uit fijne textuur lagen die dienen als beperkende lagen bijdragen tot accumulatie van zout en ernstige verstopping van de injectie laag.

Addendum

Affiliations of co-authors

Delft University of Technology
Civil Engineering & Geosciences
Department of Geoscience & Engineering
Pacelli L.J. Zitha
Ntiana El Chatib
Costas Nicolaides

Shell Global Solutions International BV
Rock & Fluid Science
Holger Ott
K. de Kloe

List of publications

Roels, S.M., Ott, H., Zitha, P.L.J., 2014. µ-CT analysis and numerical simulation of CO_2 injection into brine-saturated sandstone. Int. Journal of Greenhouse Gas Control 27, 146-154.

H. Ott, **S. M. Roels**, K. de Kloe. Salt precipitation due to supercritical gas injection: capillary-driven flow in unimodal sandstone. Accepted for publication in International Journal of Greenhouse Gas Control.

Roels, S.M., Nicolaides, C., Zitha, P.L.J., 2015. Effect of capillary-driven backflow on salt precipitation due to CO_2 injection into brine-saturated porous media. Accepted with revisions in Water Resources Research.

Roels, S.M., El Chatib, N., Nicolaides, C., Zitha, P.L.J., 2015. Capillary-driven transport of dissolved salt to the drying zone during CO_2 injection in homogeneous and layered porous media. Accepted for publication in Transport in Porous Media.

Acknowledgments

Firstly, I would like to express my sincere gratitude to my advisor Prof. Pacelli Zitha for the continuous support of my Ph.D study and related research, for his patience, motivation, and knowledge. Your guidance helped me in all the time of research and writing of this thesis. Thank you for understanding me on a personal level.

Secondly, I would like to thank Dr. Holger Ott for the interesting discussions and fruitful collaboration. I would also like to thank the rest of my thesis committee: Prof. Chris Spiers, Prof. Hans Geerlings, Prof. Jan Dirk Jansen, Prof. Bill Rossen and Dr. Karl-Heinz Wolf, for taking the time to review my research. Also, I thank Dr. Karl-Heinz Wolf for his guidance and enthusiasm in the laboratory.

My sincere thanks also goes to Marc Friebel who built my experimental setup and was as stressed as myself to obtain good results. Without his precious support it would not have been possible to conduct this research. Your singing in the laboratory lightened up the whole atmosphere. I would also like to thank the rest of the laboratory staff, in particular Wim Verwaal and Ellen Meijvogel-de Koning, for their help with the CT scanning.

I thank my fellow labmates and PhD students for the stimulating discussions and for all the fun we have had in the last four years. Also I thank my all my other friends, cousins and housemates for listening to my stories and helping me remember that there is life outside PhD. In particular, I am grateful to Dr. Leon Kapetas for keeping me calm in moments of panic.

Last but not the least, I would like to thank my family: my parents and my sister for supporting me spiritually throughout writing this thesis and my life in general.